ABSTRACT

Title of Document: LONGITUDINAL CONTROL OF INTENSE CHARGED PARTICLE BEAMS

Brian Louis Beaudoin, PhD, 2011

Directed By: Professor Patrick Gerald O'Shea
Professor Rami Alfred Kishek
Department of Electrical & Computer Engineering

As the accelerator frontier shifts from high energy to high intensity, accelerator facilities are demanding beams with higher quality. Applications such as Free Electron Lasers and Inertial Fusion Energy production require the minimization of both transverse emittance and longitudinal energy spread throughout the accelerator. Fluctuations in beam energy or density at the low-energy side of the accelerator, where space-charge forces dominate, may lead to larger modulations downstream and the eventual degradation of the overall beam quality. Thus it is important to understand the phenomenon that causes these modulations in space-charge dominated beams and be able to control them. This dissertation presents an experimental study on the longitudinal control of a space-charge dominated beam in the University of Maryland Electron Ring (UMER). UMER is a scaled model of a high-intensity beam system, which uses low-energy high-current electron beams to study the physics of space-charge.

Using this facility, I have successfully applied longitudinal focusing to the beam edges, significantly lengthening the propagation distance of the beam to 1000 turns (>11.52 km). This is a factor of 10 greater than the original design conceived for the accelerator. At this injected current, the space-charge intensity is several times larger than the standard limit for storage rings, an encouraging result that raises the possibility of operating these machines with far more space-charge than previously assumed possible.

I have also explored the transverse/longitudinal correlations that result when a beam is left to expand longitudinally under its own space-charge forces. In this situation, the beam ends develop a large correlated energy spread. Through indirect measurements, I have inferred the correlated energy profile along the bunch length.

When the bunch is contained using longitudinal focusing, I have shown that errors in the applied focusing fields induce space-charge waves at the bunch edges that propagate into the middle region of the beam. In some cases, these waves sustain multiple reflections before damping away.

I conclude that space-charge in an intense beam without longitudinal focusing can cause the bunch to develop a large correlated energy spread, increasing the risk that the beam is lost to the pipe walls as it requires a larger aperture. When longitudinal focusing is applied however, we are able to transport the beam over a much longer path length and reduce the correlated energy spread.

LONGITUDINAL CONTROL OF INTENSE CHARGED PARTICLE BEAMS

By

Brian Louis Beaudoin.

Dissertation submitted to the Faculty of the Graduate School of the
University of Maryland, College Park, in partial fulfillment
of the requirements for the degree of
Doctor of Philosophy
2011

Advisory Committee:
Professor Patrick G. O'Shea, Chair
Professor Rami Alfred Kishek
Professor Victor L. Granatstein
Professor Edo Waks
Professor Richard Ellis, Deans Representative

Dedication

To my friends and family.

Acknowledgements

First I am thankful for the guidance provided by my advisors throughout the successful completion of this dissertation and for providing their encouragement as well as advice, Professor Patrick G. O'Shea and Professor Rami A. Kishek. I also thank Professor Martin Reiser for his support and valuable intuition and my PhD examination committee members, Professor Victor L. Granatstein, Professor Richard Ellis and Professor Edo Waks.

I am grateful for all of the UMER staff as this work would not have been possible without the assistance and positive encouragements of Dr. Santiago Bernal, Dr. Timothy Koeth, Dr. David Sutter, Dr. Irving Haber, Dr. Massimo Cornacchia, and Dr. Karen Fiuza. I am also grateful to the past and current students of UMER, Dr. Charles Tobin, Dr. Christos Papadopoulos, Dr. Chao Wu, Dr. Kai Tian, Dr. Diktys Stratakis, Eric Voorhies, Hao Zhang, Yichao Mo, and Jeffrey Birenbaum for their guidance with this work. I also thank Alex Friedman, John Barnard, Dave Grote, Andy Faltens, Will Waldron and George Caporaso for the helpful discussions.

Finally, I thank the support of the United States Department of Energy Offices, of High Energy Physics and High Energy Density Physics, and by the United States Department of Defense, Office of Naval Research and Joint Technology Office

Table of Contents

List of Tables

List of Figures

Chapter 1: Introduction

1.1 Motivation

In the 20th century, the focus for particle accelerators was on colliding particles for high energy physics [1-4]. Now, the frontier is shifting from high energy to high intensity, as new applications demand the acceleration of a large number of particles that are contained in all six dimensions of phase-space [5-8]. As an example, the Linac Coherent Light Source (LCLS) at Stanford produces short-pulse bright X-rays to characterize materials and processes at the atomic and molecular levels at femto second timescales [6]. The underlying technology of these bright X-ray sources is Free Electron Lasers (FELs) that utilize coherent undulator radiation to produce coherent light from medium energy electron beams [9]. The number of photons generated from these sources is dependent on both the electron beam intensity as well as the transverse emittance [9]. The beam current at the LCLS prior to entering the undulator is on the order of 1-3 kA, delivering 250 pC of charge in 80-240 fs [10]. The transverse rms normalized emittance prior to entering the undulator is 0.5-1.6 μm, with a longitudinal energy spread that is 0.04-0.07% of the peak energy [10]. Another application that requires high current space-charge dominated beams is the proposed accelerator-driven Inertial Fusion Energy production [11]. The required power deposited on target in order to compress it and initiate a fusion reaction must be at a rate of 4×10^{14} watts, with a beam current of 40 kA [11]. This is a total of 400 μC of charge in a pulse duration of 10 ns [11]. The transverse rms normalized

emittance in this case must be approximately 0.1 μm, with a longitudinal energy spread that is 0.3% of the deposited energy [11].

Achieving these stringent specifications requires that the beam quality throughout the accelerator be maintained such that no degradation in emittance or longitudinal energy spread results. This is especially important during the low-energy stages of the accelerator where space-charge forces dominate and the beam responds more as a fluid than as a collection of single particles; exhibiting phenomena such as space-charge waves and solitons [12-14]. Small density modulations at the source can be amplified or converted to energy modulations as the beam propagates through dispersive elements, such as chicanes and doglegs, resulting in Coherent Synchrotron Radiation (CSR) [15]. This undesirable CSR in turn leads to an increase in the emittance within the bend axis, modifying the phase space, which can eventually result in beam scraping along the accelerator pipe walls [15]. Hence it is important to preserve the beam quality at the low-energy stages of the accelerator, where we can control and alleviate it; otherwise, these modulations will become frozen into the distribution at the higher-energy stages of the accelerator from the diminishing space-charge forces [16].

1.2 Background & History

Controlling space-charge forces requires an understanding of both the mechanisms behind it as well as ways of mitigating it. Space-charge waves are a result of forces within the longitudinal beam distribution from perturbations of both beam density and

energy. We can use externally applied electric fields to induce these waves as well as lessen them [14]. Using induction cells, we can apply these tailored non-linear longitudinal fields to any region of the bunch.

1.2.1 Space-Charge Waves

The history of these longitudinal modulations or space-charge waves goes back to Simon Ramo and W.C. Hahn with their investigations of space-charge and field waves in vacuum tubes in 1939 [17, 18]. In the 1950s, Birdsall and Whinnery obtained theoretical calculations of gain and phase velocity from electrons passing near lossy walls [19].

The classical method for modeling space-charge waves in a beam uses a one-dimensional cold fluid model [12]. This model treats the particles in the beam as a one-dimensional fluid and assumes the longitudinal temperature to be approximately zero, truncating the fluid equation hierarchy. If a small perturbation is added to the beam, one obtains a linear description of the line-charge density and velocity wave functions [12].

The ability to generate controlled perturbations to induce space-charge waves was pioneered at the University of Maryland Charged Particle Beam Laboratory, through experimental investigations by Dr. J.G. Wang and Dr. D.X. Wang [20, 21]. They observed the evolution of space-charge waves when applying a voltage modulation to the grid of a gridded thermionic gun. They had also explored the gun conditions required to induce single wave motion as opposed to both a fast and slow wave [20]. This perturbation work was further investigated by Dr. Yun Zou, studying the non-

linear regime of wave propagation (wave steepening) using a retarding grid energy analyzer to resolve the particle energies [22].

Dr. Yupeng Cui than developed a higher resolution retarding grid energy analyzer in order to resolve the longitudinal energy profiles of the bunch as well as the energy spread [23]. Dr. Kai Tian followed by using this analyzer to measure energy profiles of perturbed bunches in order to confirm one dimensional cold fluid calculations and WARP simulations of space-charge waves in a long solenoid channel [24].

With the advent of the University of Maryland Electron Ring (UMER), other more sophisticated methods were developed to generate controlled perturbations. The first student to use a focused ultraviolet laser onto the UMER dispenser cathode was Yijie Huo [25]. In this method, current is extracted from the dispenser cathode through photoemission. Dr. John Harris extended this work to more then half the ring during the rings construction phase and Dr. Jayakar C.T. Thangaraj continued this work through the rings closure with the multi-turn transport of laser induced density perturbations atop a long bunch [26, 27]. Dr. Thangaraj also used another laser to show space-charge wave crossings as well as laser intensity dependent induced instabilities, such as virtual cathode oscillations when over driving the cathode [27]. Though, one of the outstanding issues that Dr. Thangaraj left was the question of space-charge wave reflections in bunched beams. He did not have the ability at the time to explore this, but simulations by Dr. Alex Friedman for inertial fusion drivers, showed that it was possible to observe multiple wave reflections in a perfectly bunched beam [28].

I was the first to apply electric fields on UMER to perturb the beam energy as opposed to the density [29]. The purpose for this device was to focus the bunch longitudinally, but through timing adjustments the axial electric fields could be applied within the central region of the beam, allowing me to induce space-charge waves within the bunch. These results were then successfully compared with one-dimensional cold-fluid calculations. One of the outstanding questions, however, was the possibility of inducing space-charge waves while focusing the bunch longitudinally. Simulations by Dr. Debra Callahan showed that when these intermittent fields are applied carefully, they will generate small perturbations on the distribution [30].

The type of longitudinal focusing installed on UMER is the induction cell. By using the principle of the induced voltage across an inductive element, we can apply these longitudinal electric fields within the central core or the edges of the bunch. This allows us to easily tailor the applied voltage waveform to non-linear beam distributions by using a combination of pulsed circuits and passive elements [31]. These wide-bandwidth induction cells also allow us to get around space-limitations in compact accelerators since the operation of the cell is independent of the input voltage wavelength.

1.2.2 The Induction Principle Applied to Accelerators

The first use of the induction principle as applied to accelerators dates back to 1940 with Donald Kerst's work on the x-ray detection of accelerated electrons in a device that eventually became known as the betatron [32]. In 1964, Nicholas Christofilos

built an induction linear accelerator at Lawrence Livermore National Laboratory (LLNL) as part of the Astron Experiment [33, 34]. Other electron machines that have used induction cells since then are the Dual Axis Radiographic Hydrodynamic Testing (DARHT) facility at Los Alamos National Laboratory (LANL) and the Flash X-Ray (FXR) facility at LLNL [35-37]. Induction cells were also used on the Single Beam Transport Experiment (SBTE), Multi-Beam Experiment (MBE-4), Neutralized Drift Compression eXperiment (NDCX) and the future (NDCXII), all multi-cell linear ion accelerators at Lawrence Berkeley Laboratory (LBL) that are typically less than 100 meters in length [38-41].

To explore the physics of a beam over a long path length, a ring topology is advantageous over a linear machine, as the linear machine has a finite length whereas the circular machine is ideally infinite in length. Circular machines however, require precise synchronization between the beam and applied fields, so as to avoid timing errors that lead to focusing errors. The bends in a ring also impact the transverse dynamics through the lattice dispersion, resulting in correlated centroid motion in the beam ends.

The LLNL recirculator was the first circular ion induction accelerator ever built [42]. Though the machine was never completed, it propagated a 2 mA 80 keV K^+ beam over a quarter of the ring, a distance of more than 6.6 m. The KEK proton induction synchrotron was also built using induction focusing and acceleration as opposed to normal RF cavities [43]. The use of induction focusing enabled them to get around the limitation of the available longitudinal phase space for acceleration from 0.5 GeV to 12 GeV, through tailored voltage profiles [43, 44].

The first use of induction focusing at the University of Maryland Charged Particle Beam Laboratory was with the 5-meter solenoidal linear accelerator [12]. Dr. D.X. Wang showed beam manipulation using induction focusing over a short distance [21]. The next use of induction focusing by the group has been through the installation of the induction cell on the University of Maryland Electron Ring. This high-intensity circular machine was conceived and constructed for the study of long path length space-charge dominated beam physics on a small scale [12, 16, 45].

Using this accelerator, we are able to apply controlled perturbations to study these modulation effects in beams while the beam remains at a low-energy. We also have the ability to study techniques to control and potentially reverse any of these modulation effects before they become irreversible [14]. This dissertation presents an experimental study on the requirements needed to control the non-linear longitudinal space-charge forces at the University of Maryland Electron Ring. The need for this control is necessitated by the fact that the beam longitudinally expands and fills the ring, wrapping multiple times around the circumference of the machine. Without these focusing fields, the beam also incurs a correlated centroid motion along the bunch, which increases the potential for scraping and resonant charge loss mechanisms. This dissertation investigates these topics, as well as longitudinal focusing and synchronization errors. Though we center on the parameter range for UMER, the underlying phenomena's are generally applicable.

1.3 Organization of Dissertation

This dissertation begins in chapter 2 by reviewing the one-dimensional cold fluid theory for space-charge waves and rectangular bunch erosion. In chapter 3, we present some of the UMER diagnostics relevant to this dissertation as well as the details of the induction cell, including the basic limitations of the ferrite material and cell frequency response. In chapter 4, we discuss the experimental studies on the transverse-longitudinal correlation of an unconfined bunch. This includes the resulting centroid motion along the bunch and its correlation to beam energy and tune. In chapter 5, we discuss the experimental results on the longitudinal containment of the bunch. Analyzing the trade-offs between focusing period and gradient at long path-lengths as well as the sensitivity to frequency errors. In chapter 6, we discuss the longitudinal mismatched induced space-charge waves at the bunch edges and the occurrence of multiple wave reflections. Finally in chapter 7, we draw conclusions and list suggested ideas for other experiments and PIC simulations that could assist in continuing the exploration on confining space-charge dominated beams using induction focusing.

Chapter 2: Space-Charge Waves and Head/Tail Effects of a Rectangular Bunch

In this chapter we review the theory of longitudinal wave propagation in a space charge dominated beam as well as rectangular bunch erosion. The purpose of this chapter is to analyze the theoretical predictions of wave polarities when an initial perturbation is either a pure density modulation or a pure velocity modulation. This chapter also analyzes the rectangular eroding beam frame solutions of line-charge density and velocity as well as the longitudinal-transverse correlation in application to circular machines. We finish with a derivation of the total energy within the bunch-ends.

2.1 Linear Wave Motion in Coasting Beams

This section reviews the one-dimensional cold fluid model along with the definition of sound speed and the wave dispersion relation for an infinitely long cylindrical beam inside a conductive pipe. The evolution of wave magnitudes and polarities are also analyzed with various analytical Gaussian wave illustrations as a result of different initial perturbations.

2.1.1 One-Dimensional Theory of Linearized Wave Motion

The longitudinal dynamics of beams with space-charge can be accurately captured through the use of a cold fluid model, if the beam has a very low longitudinal thermal velocity spread, i.e. one that is significantly less than the space-charge wave speed [12]. Here, we briefly review the 1-D theory for wave propagation.

The cold fluid model represents the beam as a 1-D fluid and assumes a zero temperature so as to truncate the fluid equation hierarchy. Transversely, the beam is assumed to be a cylinder of charge with the radius equal to a, inside a pipe of radius b with line-charge density λ, beam velocity v and product of the two $\lambda\mathrm{v}$, equal to the beam current I.

For small perturbations we can linearize the momentum and continuity equations by writing the line-charge density, velocity and beam current as the sum of a constant plus a perturbed quantity [12].

$$\begin{aligned} \lambda(z,t) &= \lambda_0 + \lambda_1 e^{i(\omega t - kz)} \\ \mathrm{v}(z,t) &= \mathrm{v}_0 + \mathrm{v}_1 e^{i(\omega t - kz)} \\ I(z,t) &= I_0 + I_1 e^{i(\omega t - kz)} \end{aligned} \qquad \text{(Eqn. 2. 1)}$$

The quantities with the subscript *0*, represents the constant part of the beam and the subscript *1* represents the perturbation which varies both in time as well as space. After linearizing the continuity and momentum equations and then performing the necessary Fourier transforms, we obtain the dispersion relation as well as the phase velocity (sound speed) of a wave moving within the beam frame,

$$(\omega - \mathrm{v}_0 k)^2 = \frac{q}{\gamma_0^3 m}\frac{g}{4\pi\varepsilon_0\gamma_0^2}\lambda_0 k^2 = C_s^2 k^2 \qquad \text{(Eqn. 2. 2)}$$

$$C_s = \sqrt{\frac{q}{\gamma_0^5 m}\frac{g}{4\pi\varepsilon_0}\lambda_0} \qquad \text{(Eqn. 2. 3)}$$

where q is the electron charge, m the electron mass, γ_0 the Lorentz factor, ε_0 the relative permittivity and the variable g is the geometry factor. This factor accounts for the beam pipe shielding of the longitudinal electric fields of the bunch [12].

$$g = \alpha + 2\ln\left(\frac{b}{a}\right) \qquad \text{(Eqn. 2. 4)}$$

If the injected bunch is transversely emittance dominated, then α in Eqn. 2.4 is equal to $1/2$. Whereas if the bunch is transversely space-charge dominated, then α is equal to 0. This constant represents the axial electric field E_z variation as either a perturbation in the line-charge density (with a constant beam size) or a perturbation in the beam size (with a constant volume charge density) [12]. The intensity parameter χ is a dimensionless parameter with a value between 0 and 1 that defines if the beam is emittance dominated or space-charge dominated. It is defined as $\chi = \frac{K}{k_o^2 a^2}$, where K is the perveance and $k_o^2 a^2$ the external focusing force. If the intensity parameter is less than $1/2$, the beam is emittance dominated, and if it is greater than $1/2$, the beam is space-charge dominated [12].

The wave dispersion relation (Eqn. 2.2), of the space-charge wave, defines that the wavelength (or frequency) of the wave is independent of the sound speed. Within linear theory, space-charge waves of various wavelengths will propagate either faster v_f than the beam velocity or slower v_s than the beam velocity, propagating as a non-dispersive wave through the bunch.

$$\begin{aligned} \mathrm{v_f} &= \mathrm{v_0} + C_s \\ \mathrm{v_s} &= \mathrm{v_0} - C_s \end{aligned} \qquad \text{(Eqn. 2. 5)}$$

Non-dispersive wave motion, are waves that maintain their initial shape as the wave perturbation propagates [46]. The following two sections detail wave parameters in an infinitely long cylindrical beam.

2.1.2 Velocity versus Density Perturbations

Space-charge waves can be launched from either an initial density perturbation or an initial velocity perturbation, or any combination thereof. The difference between an initial pure density perturbation and an initial pure velocity perturbation are the respective fast and slow wave polarities in velocity, line-charge density and current space. Let us assume a general perturbation launched at $t = 0^+$, and use $\delta = \dfrac{\mathrm{v_1}\left(0, t = 0^+\right)}{\mathrm{v_0}}$ to denote the magnitude of the velocity perturbation at $t = 0^+, z = 0$ and $\eta = \dfrac{I_1\left(0, t = 0^+\right)}{I_0}$ to denote the magnitude of the current perturbation at $t = 0^+, z = 0$. The analytical solutions for the perturbed line-charge density, velocity and current are shown, (see Eqns. 2.6, 2.7, 2.8) where the shape of the perturbation is characterized by a smooth-varying function of magnitude equal to unity $p\left(t - \dfrac{z}{\mathrm{v_0} \mp C_s}\right)$. The top sign within the smooth-varying function is used for the slow wave and the bottom sign is used for the fast wave [20, 29].

$$\lambda_1(z,t) = \mp\frac{\lambda_0}{2}\left[\delta\frac{\mathrm{v}_0}{C_s} \mp (\eta-\delta)\right] p\left(t - \frac{z}{\mathrm{v}_0 \mp C_s}\right) \quad \text{(Eqn. 2. 6)}$$

$$\mathrm{v}_1(z,t) = \frac{\mathrm{v}_0}{2}\left[\delta \mp (\eta-\delta)\frac{C_s}{\mathrm{v}_0}\right] p\left(t - \frac{z}{\mathrm{v}_0 \mp C_s}\right) \quad \text{(Eqn. 2. 7)}$$

$$I_1(z,t) = \mp\frac{I_0}{2}\left[\delta\frac{\mathrm{v}_0}{C_s} \mp \eta + (\eta-\delta)\frac{C_s}{\mathrm{v}_0}\right] p\left(t - \frac{z}{\mathrm{v}_0 \mp C_s}\right) \quad \text{(Eqn. 2. 8)}$$

Figure 2.1a-b, displays the magnitude functions of line-charge density, velocity and current for both cases described above, as either a function of η or δ. It is calculated from the equations above with either η or δ set to zero.

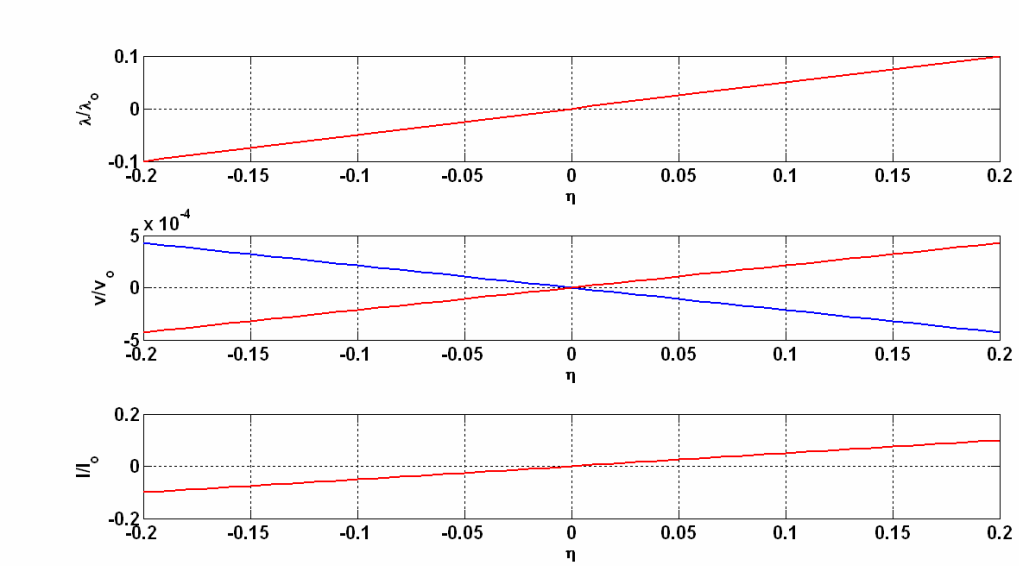

(a)

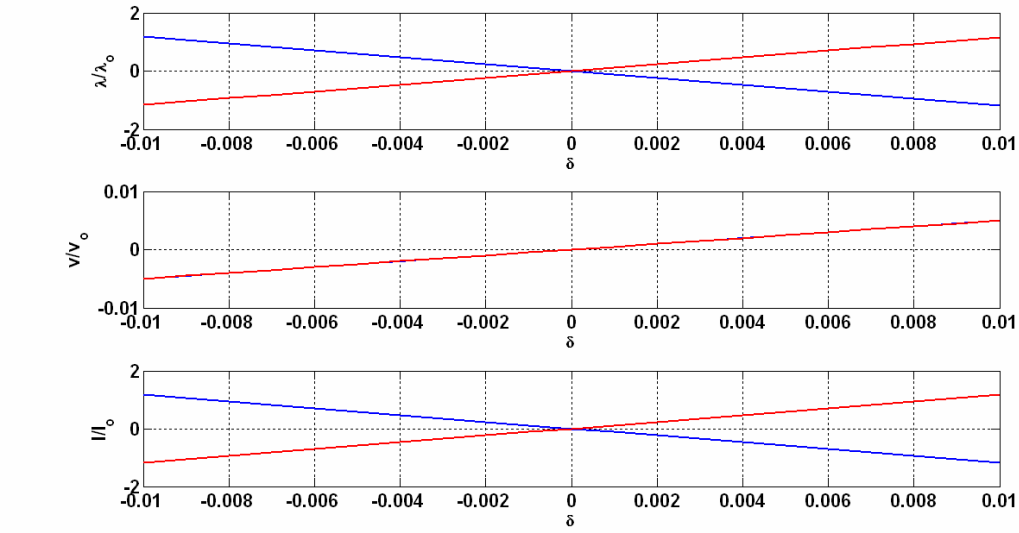

(b)

Fig. 2. 1. Magnitude function of the perturbed line-charge density, velocity and current waves for an initial (a) density ($\delta = 0$), or (b) velocity ($\eta = 0$) perturbation. Fast wave information is displayed in red, where as the slow wave information is displayed in blue.

If a positive-amplitude density perturbation is placed on the beam with $\eta = 0.1$, i.e., an increase in line-charge density, then the density and current will have the same polarity for both waves but opposing polarities for the velocity waves. This is shown

in Fig. 2.1a with the red and blue velocity wave amplitude lines. The fast wave line has a positive slope while the slow wave line has a negative slope.

If a positive-amplitude velocity perturbation is placed with $\delta = 0.002$, then the velocity waves will have identical polarities but the line-charge density and current will have opposing wave polarities, as shown in Fig. 2.1b. The fast and slow velocity wave amplitude lines are overlaid on top of each other, resulting in identical polarities. The next section (Sec. 2.1.3), illustrates wave motion as a result of the various induced perturbations using a Gaussian wave profile.

2.1.3 One-Dimensional Wave Propagation of an Analytical Solution

Gaussian wave analytical calculations for density induced and velocity induced perturbations are shown below (see Figs. 2.2a-b and Fig. 2.3a-b, respectively). These calculations assume linear propagation and zero dispersion.

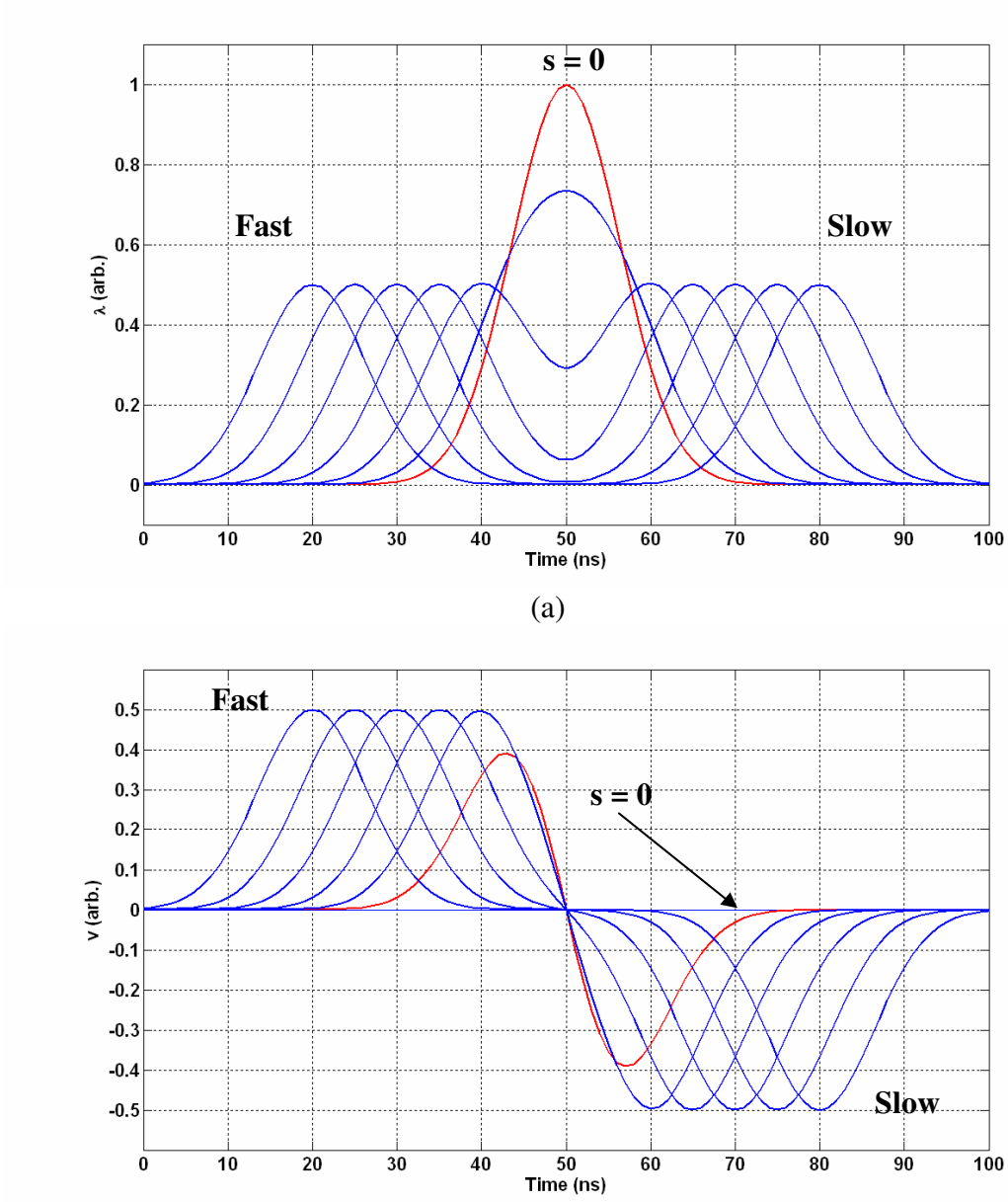

Fig. 2. 2. (a) Line-charge density and (b) velocity waves (within the beam frame) from an induced positive density perturbation (the red curves at $s = 0$), with each profile calculated at equal distances starting from the point where the perturbation originates. Vertical axes are in arbitrary units.

The profiles are separated by equal distances, starting from the point of initiation at $s = 0$ (the red curves). For this case, the positive perturbation in density splits into two waves moving in opposite directions with identical polarities where as the

velocity waves are opposing in polarity. The density waves also drop by a factor of two from the initial perturbation amplitude. If a pure velocity perturbation is placed on the beam, then the waves will propagate as shown in Fig. 2.3a-b.

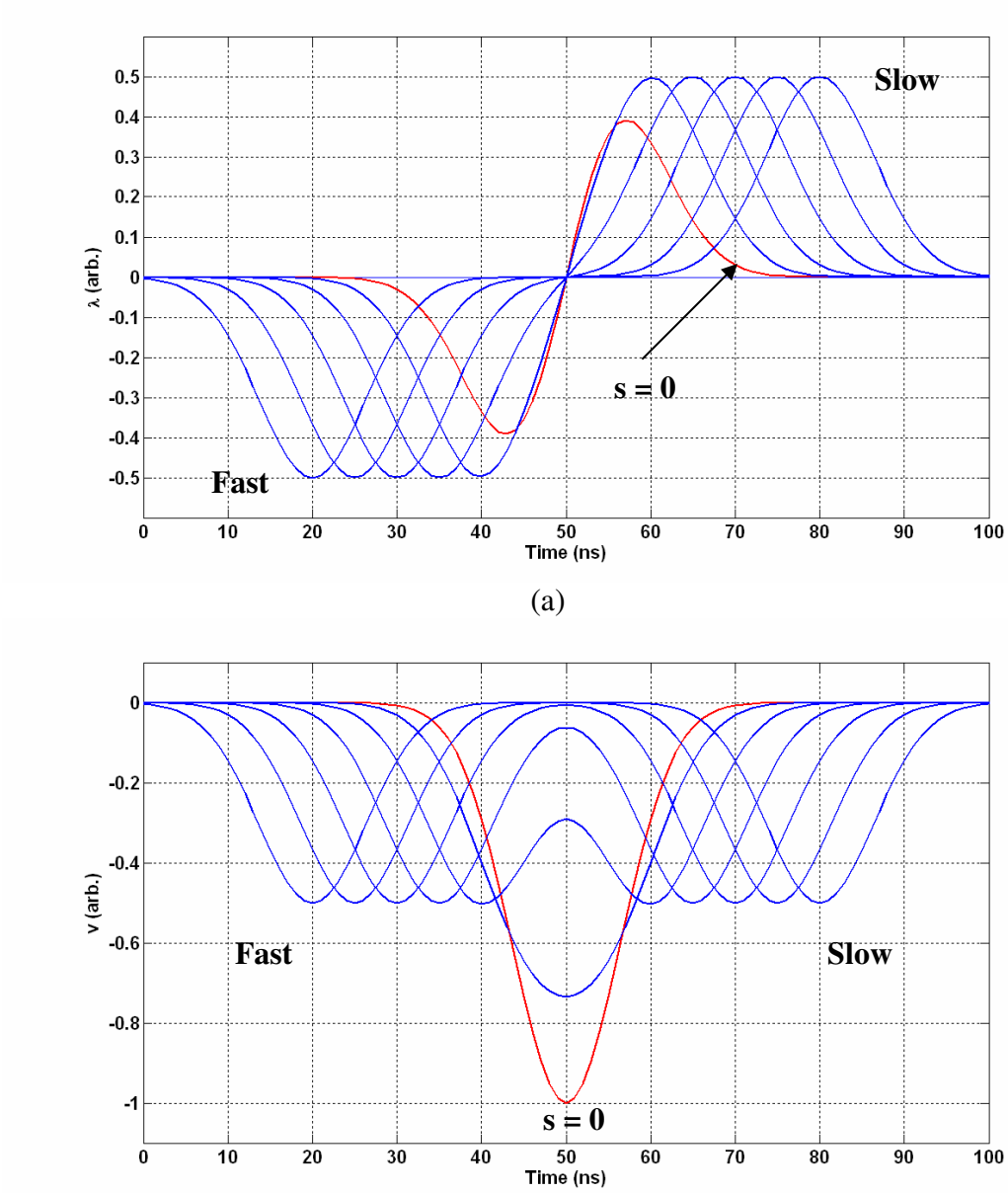

Fig. 2. 3. (a) Line-charge density and (b) velocity waves (within the beam frame) from an induced negative velocity perturbation (the red curves at $s = 0$), with each profile calculated at equal distances starting from the point of the where the perturbation originates. Vertical axes are in arbitrary units.

The positive perturbation in velocity also splits into two waves moving in opposite directions, whereas the density waves are opposite in polarity and the velocity waves are identical in polarity, dropping by a factor of two from the initial perturbation amplitude. This concludes the discussion on waves and the following section (Sec. 2.2), illustrates the basics of rectangular bunch-end erosion in a long beam.

2.2 Rectangular Bunch Erosion

The one-dimensional theoretical model of bunch-end erosion is presented in this section along with calculations of beam current evolution as a function of the propagated distance, including Particle-In-Cell (PIC) simulations. This section also explores the nuances of the one-dimensional model when applied to linear and circular transport lines.

2.2.1 One-Dimensional Theory of End-Erosion

The longitudinal dynamics of a space-charge dominated rectangular bunch with uniform line-charge density and velocity is highly non-linear. The longitudinal electric field, within a uniform bunch, is approximately equal to the derivative of the line-charge density along the bunch. This holds true as long as the bunch remains non relativistic with slow variations in the line-charge density [47].

The axial electric field is approximately equal to zero within the mid region of the uniform bunch, but gradients in the line-charge density near the bunch-ends lead to

longitudinal electric self-fields that push particles in the bunch away from the ends [48-50]. This causes the bunch to lengthen longitudinally.

In the moving beam frame, particles at the head of the beam will be accelerated forward from the main bunch while particles at the tail will be accelerated backwards from the main bunch. By solving the one-dimensional fluid equations through the method of characteristics, we obtain line-charge density and velocity analytical wave solutions in the beam frame and time domain [48-50]. This allows us to track beam profiles as a function of the bunch propagation distance s. The solutions for the front of the bunch are shown below as a function of t, time within the beam frame starting from the center of the bunch at $t = 0$,

$$\frac{\lambda}{\lambda_o} = \begin{cases} 1, \; t > \left(\frac{1}{2} - \frac{s}{2s_{rarefaction}}\right)\tau_o \\ \left(\frac{2}{3} + \frac{s_{rarefaction}}{3s}\left(1 - \frac{2t}{\tau_o}\right)\right)^2, \; \left(\frac{1}{2} - \frac{s}{2s_{rarefaction}}\right)\tau_o < t < \left(\frac{1}{2} + \frac{s}{s_{rarefaction}}\right)\tau_o \end{cases} \quad \text{(Eqn. 2. 9)}$$

$$\frac{v}{C_s} = \begin{cases} 0, \; t > \left(\frac{1}{2} - \frac{s}{2s_{rarefaction}}\right)\tau_o \\ \frac{2}{3}\left(1 - \frac{s_{rarefaction}}{s}\left(1 - \frac{2t}{\tau_o}\right)\right), \; \left(\frac{1}{2} - \frac{s}{2s_{rarefaction}}\right)\tau_o < t < \left(\frac{1}{2} + \frac{s}{s_{rarefaction}}\right)\tau_o \end{cases} \quad \text{(Eqn. 2. 10)}$$

where τ_o is the injected beam length in units of time and $s_{rarefaction}$ is the beam propagation distance required for the rarefaction waves to interact [48-50]. An explanation of the rarefaction distance will be presented within this section. The line-charge density and velocity solutions are symmetric for either side of the bunch, i.e. the solutions are time-reversible within the beam frame.

As the beam erodes, each end (expansion wave) will expand at a rate of $2C_s$ with the (rarefaction wave) moving at a rate of C_s inward as shown in Fig. 2.4 [47-51].

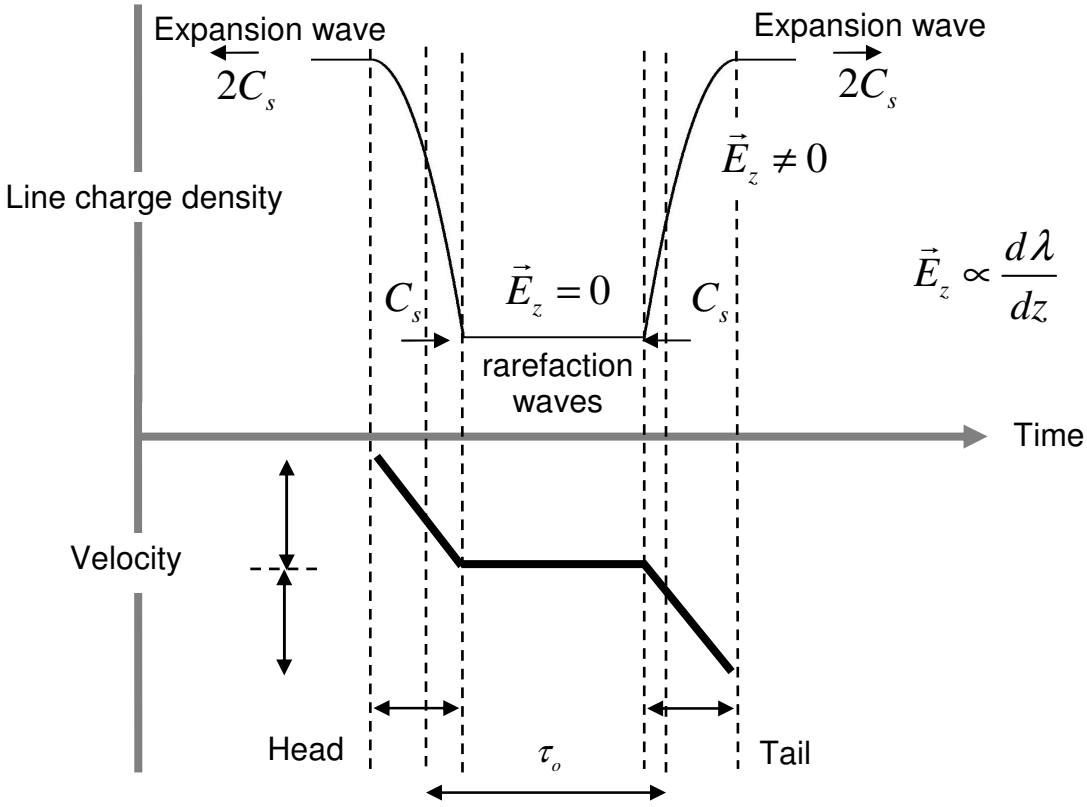

Fig. 2. 4. Beam line-charge density and velocity profiles as a function of time for an initially rectangular beam distribution.

There are two regions of wave propagation along the bunch when this model is applied to a linear transport line and three regions when this model is applied to a ring topology. The extra region is a result of the closed boundary condition of a ring topology that would not necessarily be considered in a linear system. The first is the simple-wave region; in this case, both the rarefaction waves and expansion waves, from either side, have not come into contact. The analytical solutions (Eqn. 2.9 and 2.10) are well defined within this region [50]. The second region is defined as the non simple-wave region. In this region, either the rarefaction waves or the expansion

waves may come into contact initially. Which ever set of waves is first, depends on the bunch length relative to the ring lap time. In a linear transport line, only the rarefaction waves will meet.

If we assume a ring lap time of $2\tau_o$ and assume that the injected beam length τ_o is longer than $\frac{1}{3}$ the total lap time or $\frac{2\tau_o}{3}$, the expansion waves at the bunch edges will interact before the rarefaction waves interact in the center of the beam-bunch. If the injected beam length is shorter then $\frac{2\tau_o}{3}$, the rarefaction waves will interact first.

If we assume that the beam length is longer than $\frac{1}{3}$ the total lap time, the distance the bunch propagates around the ring before the expansion waves interact and interpenetrate each other is calculated using Eqn. 2.11.

$$s_{expansion} = \frac{v_o^2 \tau_o}{4C_s} \qquad \text{(Eqn. 2. 11)}$$

The third region is just an extension of the second region, in that, which ever set of waves interacts first, the other set will then interact. Continuing with the same assumption that the beam length is longer than $\frac{1}{3}$ the total lap time; the distance the bunch can propagate around the ring before the rarefaction waves interact, is calculated using Eqn. 2.12.

$$s_{rarefaction} = \frac{v_o^2 \tau_o}{2C_s} \qquad \text{(Eqn. 2. 12)}$$

No analytical solutions of velocity and line-charge density exist after any of the wave interactions, but some formulas do approximate the result [50, 52]. Section 2.2.2, illustrates the bunch-end erosion of an initially rectangular bunch.

2.2.2 One-Dimensional Analytical Calculation and Simulation of End-Erosion

With no confinement, the longitudinal space-charge forces at the bunch-ends will cause the beam to expand until particles fully occupy the ring with charge (assuming a ring topology), as shown in Fig. 2.5.

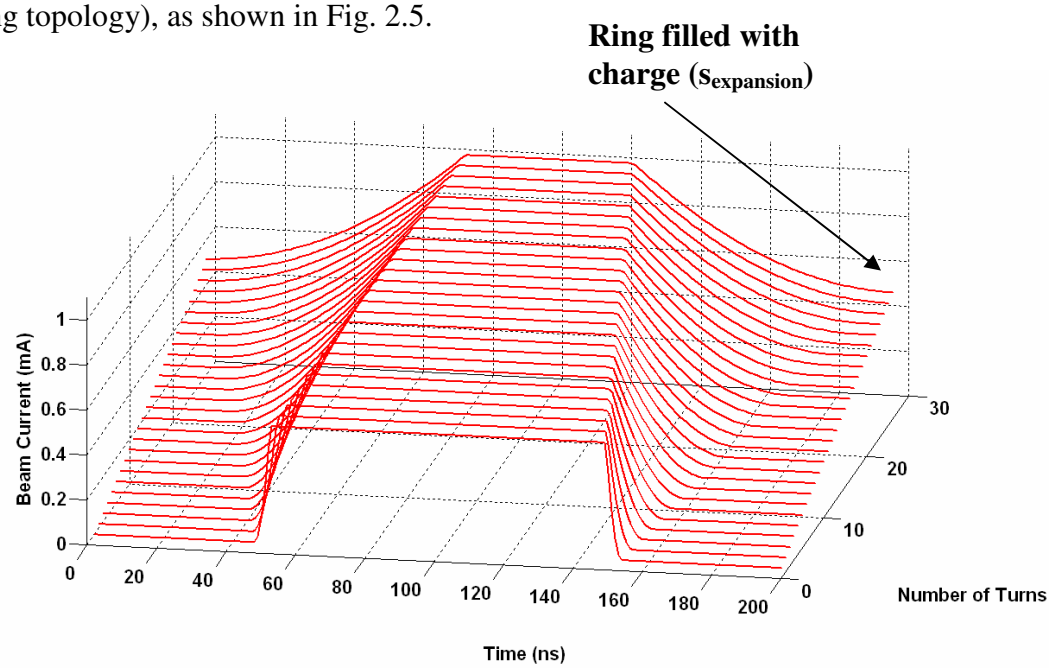

Fig. 2. 5. Analytical beam current calculation of the head and tail evolution, assuming an injected beam length that is longer than $\frac{1}{3}$ the total lap time.

The plot above is a mountain range plot of beam current chopped at the revolution frequency. The flat central region of the beam is decreasing in length, due to the rarefaction waves eroding the beam center. For charge to be conserved, the bunch

must also elongate, hence the expansion of the bunch edges (expansion waves). The analytical solutions are valid only within the simple-wave region and are not representative of the physics within the non simple-wave region. A Particle-In-Cell (PIC) code WARP, is used to track the bunch-end physics within the non simple-wave region [53]. The WARP simulation results for the same assumptions as in the analytical calculations are shown in Fig. 2.6.

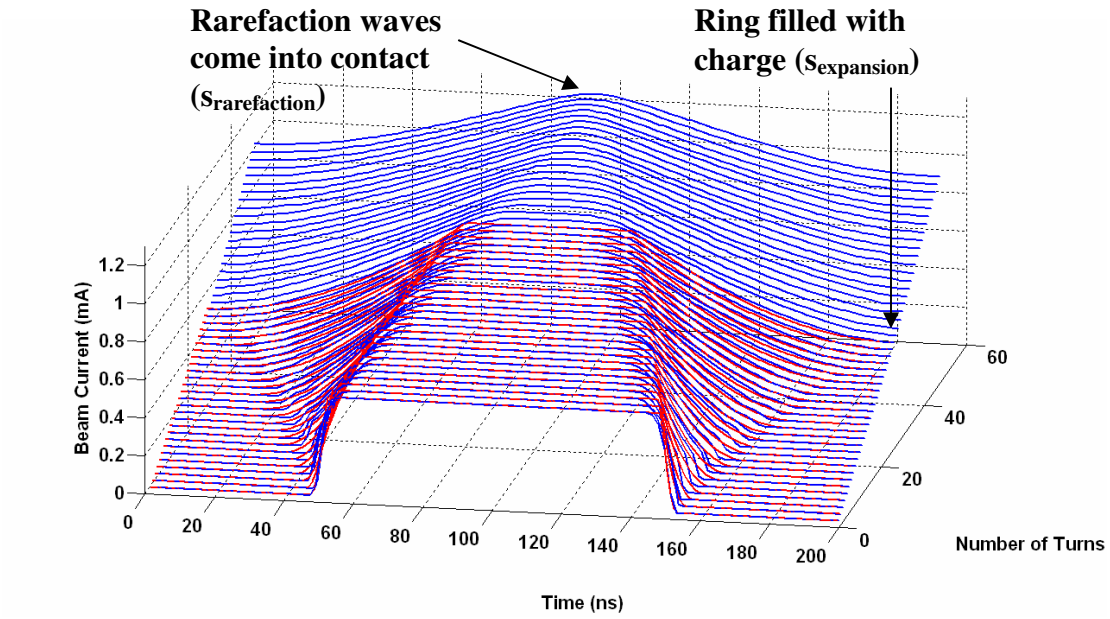

Fig. 2. 6. WARP simulation of beam current evolution using the same assumptions as in the analytical calculations is shown in blue. The analytical beam current calculation of the head and tail evolution is shown in red.

This simulation is done using an RZ field-solver with uniform focusing and a total grid array in z equal to the circumference of the ring. A periodic boundary condition is set in z, for both the particles and the fields. The number of cells in r and z was 64 and 256. The total number of macro-particles in the simulation was 10 million with a step of 10 cm or approximately 1.71 ns. The initial longitudinal thermal spread in the simulation was 1.5×10^5 m/s or 50 eV.

The PIC code includes the physics of the non simple-wave region; including both the point when the ring fills with charge as well as the point when the rarefaction waves come into contact with each other. The simulation agrees well with the analytical calculations in representing the rates of the expansion wave and the rarefaction waves at a given injected beam current but it does not capture the discontinuous shape of the analytically calculated current profiles. The next section, Section 2.3, analyzes the result of bunch elongation on circular lattice dependent parameters.

2.3 Transverse Correlation of Bunch Elongation

The transverse correlation to bunch elongation is explored in this section with an emphasis on circular machines. In the previous section, we explored the peak beam current dependent evolution of bunch elongation using both analytical calculations and PIC simulations. In this section, we perform a simple analysis to understand the correlation of the head and tail effects with bunch centroid.

2.3.1 Longitudinal Velocity Profile

The longitudinal velocity profile can be used to calculate the mean longitudinal beam energy profile. The peak energy difference between the beam head to mid region of the bunch is, $\Delta E_{\max}$ a quantity limited by the maximum wave speed at the edges of the beam or $2C_s$ within the beam frame. There is a similar energy difference between the beam tail to mid region. As the beam continues to expand longitudinally, the head and tail regions of the beam constitute a larger fraction of the

overall bunch length. Depending on beam current and on the dispersive properties of the lattice, the large energy difference at the head and tail from the nominal energy can push particles in the head and tail outside the aperture of the lattice, resulting in localized particle loss due to scraping. Even when the energy difference is small, chromatic effects in the lattice can change the operating ring tune sufficiently to bring portions of the head and tail into a resonance.

The maximum difference in energy can be calculated, for non-relativistic beams, in the Galilean frame from Eqn. 2.13.

$$\Delta E_{\max} = \frac{1}{2} m \left(\mathrm{v}_{\mathrm{o}} + 2C_s \right)^2 - \frac{1}{2} m \mathrm{v}_{\mathrm{o}}^2 \qquad \text{(Eqn. 2. 13)}$$

The peak changes in particle energies occur at the very edges of the bunch, in both the head and tail. The analytically calculated velocity profile (shown in Fig. 2.7) using the same set of assumptions used to calculate Fig 2.5 and 2.6, reaches a maximum velocity that is equal to $\mathrm{v}_{\mathrm{o}} + 2C_s = 5.975 \times 10^7$ m/s for the bunch head, with the bunch tail reaching a minimum velocity equal to $\mathrm{v}_{\mathrm{o}} - 2C_s = 5.867 \times 10^7$ m/s.

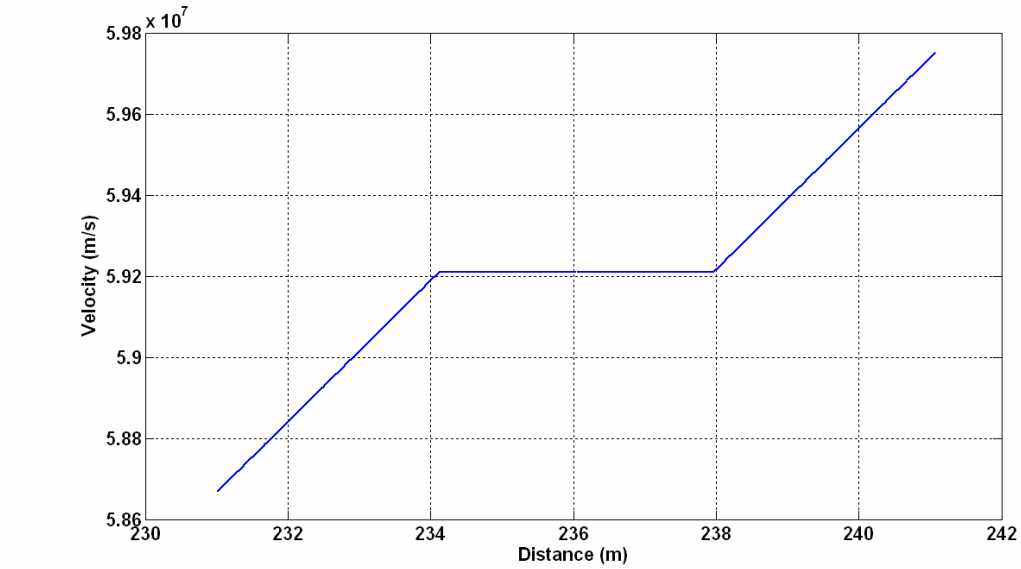

Fig. 2. 7. Longitudinal z-v_z phase space of an analytical calculation using the same beam parameter assumptions throughout Ch 2.

The WARP simulation results (shown in Fig. 2.8 below) is a snapshot in z, of the longitudinal phase space for the same beam parameters and propagation distance as in the analytical calculations. It illustrates the same increase in peak energy at the head and a decrease in peak energy at the tail from the injected energy.

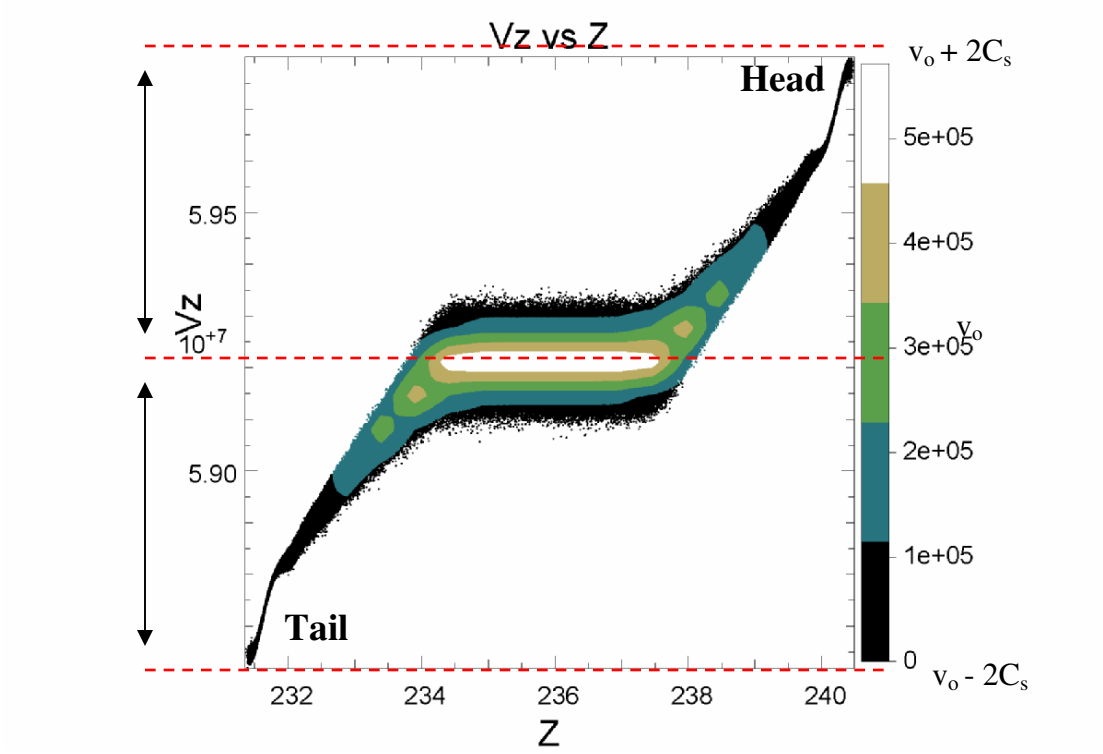

Fig. 2. 8. Longitudinal z-v_z phase space from WARP, calculated for the same propagation distance as in the analytical calculations.

The simulated bunch head reaches a maximum velocity that is equal to $v_o + 2C_s = 5.98\times10^7$ m/s and the bunch tail reaches a minimum velocity, which is equal to $v_o - 2C_s = 5.86\times10^7$ m/s. The simulated velocity profiles agree fairly well with the analytical calculations, resulting in only a 0.12% difference between simulation and calculations for the maximum and minimum velocities at the bunch edges. Both methods also capture the nonlinear profile that changes as the beam propagates through the lattice. The benefit of the WARP simulation is that it includes the uncorrelated energy spread in the calculation.

The following two sections, Sec. 2.3.2 and Sec. 2.3.3, correlate the longitudinal energy (velocity) profile to transverse centroid motion along the bunch.

2.3.2 Correlation between Lattice Dispersion and Bunch-Ends

The dispersion function (Eqn. 2.14) is a lattice-dependent function that equates displacement from the central orbit to a change in momentum ΔP from the injected momentum P_o.

$$x_e(s) = D_e(s)\frac{\Delta P}{P_o} \qquad \text{(Eqn. 2. 14)}$$

By summing the displacement of a particle due to the betatron oscillation amplitude $x_b(s)$ and that due to the dispersion function $x_e(s)$, we obtain the total displacement from the central orbit $x(s) = x_b(s) + x_e(s)$ [12].

The correlated energy differences of the head and tail make the head and tail travel different equilibrium orbits from the central bunch. Knowing the dispersion at a particular location in the ring, allows us to calculate the change in orbit of the head and tail particles at that location.

The simple analytical calculation of the average dispersion within a ring can be calculated using $D_e = \frac{R}{\nu_o^2}$, where R is the ring radius and ν_o is the zero-current tune of the machine [12]. If we assume a machine operating tune of 6.165 and ring radius of 1.8333 m, the average dispersion function will be 0.0482 m.

The dispersion function can be calculated for an ideal ring using an optics code such as WinAgile [54]. The optic elements used in this model are based on the UMER lattice parameters, which will be discussed in Ch. 3.

The figure below displays the dispersion function for an ideal ring assuming no injection section.

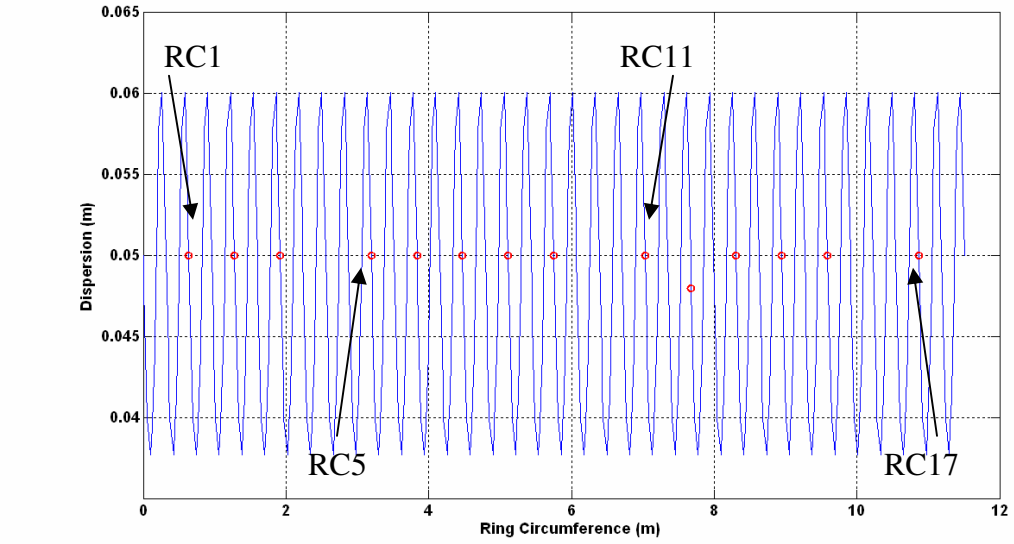

Fig. 2. 9. WinAgile calculations of the dispersion function with a horizontal tune of 6.165.

The red circles in Fig 2.9, represent locations of Beam Position Monitors (BPMs) used around the UMER ring to obtain centroid information. The WinAgile calculated dispersion function has an average of 0.0498 m, which agrees fairly well with the analytically calculated average dispersion to within 3.2%.

Knowing the average dispersion, we estimate the maximum orbit displacement as a function of peak head and tail energies.

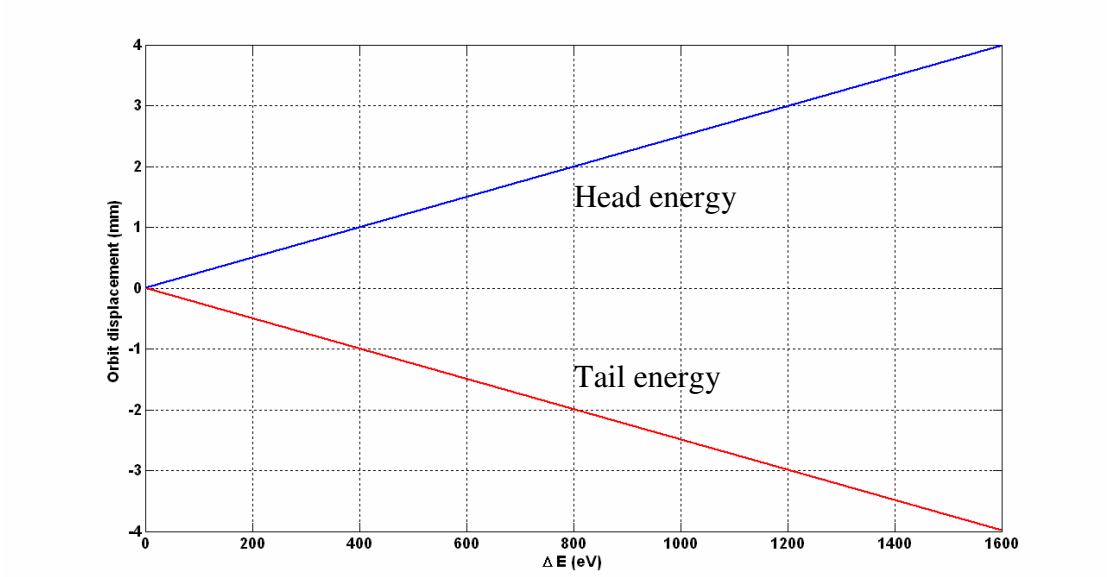

Fig. 2. 10. Orbit displacements at a mean dispersion function of 0.0498 m versus bunch head and tail peak energies, for a design beam energy of 10 keV.

Figure 2.10 above is a calculation of orbit displacement versus peak head and tail energies, using 0.0498 m for the mean dispersion function. If the head has an $\Delta E_{\max}$ of +800 eV, the displacement from bunch head to central region would be +2 mm. If the bunch tail has an $\Delta E_{\max}$ of -400 eV, the displacement will be -1 mm. If the injected beam current is smaller, resulting in a smaller sound speed, than the orbit displacements at both the head and tail would result in a smaller displacement. This correlation of peak head and tail energies to orbit displacement is both a function of bunch length and propagation distance. The following section extends this correlation to betatron tune.

2.3.3 Tune Shift

Strong focusing or alternating-gradient focusing machines allows the number of betatron cycles (tune) to be larger than one revolution around the ring, in contrast to weak focusing machines, where the number of betatron cycles is restricted to less then one [55]. Operating a strong focusing machine with a tune near an integer resonance can be catastrophic, leading to beam scraping from closed orbit distortions and eventual loss of the entire beam. The bunch in these conditions will experience dipole kicks on each revolution that causes the orbit amplitude to grow and eventually result in beam scraping. This is a result of the betatron oscillation returning with the same phase at each revolution. Resonances are also possible at higher orders but are "basically survivable" beyond the half-integer [56].

If the tune is selected away from a resonance for a given injected energy, particles at that energy will survive. However, since the head and tail experiences different energies than the rest of the beam, they will correspondingly experience different tunes. Thus even if the tune for the center of the bunch is away from a resonance, the head and tail particles can be driven into a resonance. Here we estimate the tune shift in the head and tail as a result of longitudinal bunch expansion.

The tune dependence on beam energy for N FODO cell periods in a ring is shown in Eqn. 2.15 and 2.16,

$$v = \frac{N\sigma}{2\pi}$$
$$v = \frac{N}{2\pi}\cos^{-1}\left(\cos\theta\cosh\theta + \frac{L}{l}\theta\left(\cos\theta\sinh\theta - \sin\theta\cosh\theta\right) - \frac{1}{2}\left(\frac{L}{l}\right)^2\theta^2\sin\theta\sinh\theta\right) \quad \text{(Eqn. 2. 15)}$$

$$\theta = \sqrt{\frac{qB_o}{\gamma ma\mathrm{v}_o}}\,l \quad \text{(Eqn. 2. 16)}$$

where θ represents the focusing strength of the lenses as defined in [12], l the magnet effective length, L the drift space within the FODO cell and N the total number of FODO cells in the ring.

At the far edges of the beam, the tune will be at a minimum in the head and at a maximum in the tail from the injected energy. Figure 2.11 below, displays the calculated tune as a function of peak head and tail energies.

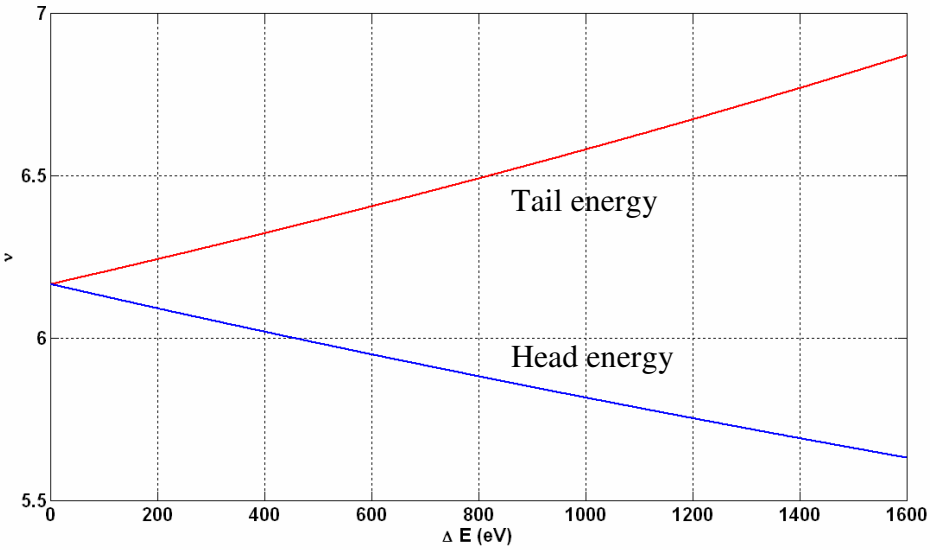

Fig. 2. 11. Tune dependence on peak head and tail energy.

If the beam head has an $\Delta E_{\max}$ of + 400 eV from the injected energy E_o, the local tune at the head of the beam will decrease by 0.147 from 6.165, approaching the integer line. For the same $\Delta E_{\max}$ in the tail, the tune will increase by 0.156 from 6.165. If the tune shift at the head and tail of the bunch is sufficiently large to cross a resonance, those particles could be blown off the beam as they fall into the resonance. This would result in a loss mechanism that reduces the overall length of the injected bunch as it propagates.

In summary, it is necessary to use longitudinal focusing to prevent bunch elongation otherwise space-charge forces will lengthen the bunch, resulting in a correlated centroid motion along the bunch that could be detrimental over a long or short path length. The last section, Sec. 2.4, derives the energy stored in the bunch-ends in order to confirm the formulations in Sec. 2.2.

2.4 Energy Stored in Bunch-Ends

Keeping the beam bunched over a long path length requires longitudinal focusing fields that prevent the beams expansion (as discussed in Sec. 2.2). With longitudinal containment, the axial space-charge fields become contained by the periodically applied focusing fields, maintaining an average bunch length. In this section we derive the energy stored in the eroding edges of the bunch.

2.4.1 Bunch Edge Erosion

As discussed in Sec. 2.2, the bunch-ends expand as a result of the expansion wave with a rarefaction eroding the central region of the beam. This is shown within the beam frame in Fig. 2.4. The beam end is a function of both z and t, where t is the propagation time within the accelerator structure. If the line-charge density for the bunch head, defined as an Eqn. 2.17, is frozen at a time t_o then the axial electric field (Eqn. 2.18) is a linear function of z.

$$\lambda(z, t = t_o) = -\lambda_o \frac{z^2}{L_o^2},\ 0 \le z \le L_o \qquad \text{(Eqn. 2. 17)}$$

$$E_z\left(z,t=t_o\right)=\frac{-g}{4\pi\varepsilon_o}\frac{d\lambda(z)}{dz}=\frac{g2\lambda_o z}{4\pi\varepsilon_o L_o^2},\ 0\le z\le L_o \qquad \text{(Eqn. 2. 18)}$$

The length of either bunch-end is defined as L_o assuming time is frozen at t_o, where the line-charge density and electric field reaches a peak. If the force is computed (Eqn. 2.19) using the electric field, then the peak force also exists at $z=L_o$.

$$F_z\left(z,t=t_o\right)=\frac{-eg2\lambda_o z}{4\pi\varepsilon_o L_o^2},\ 0\le z\le L_o \qquad \text{(Eqn. 2. 19)}$$

A pictorial diagram of the normalized line-charge density, electric field and force is shown in Fig. 2.12 below.

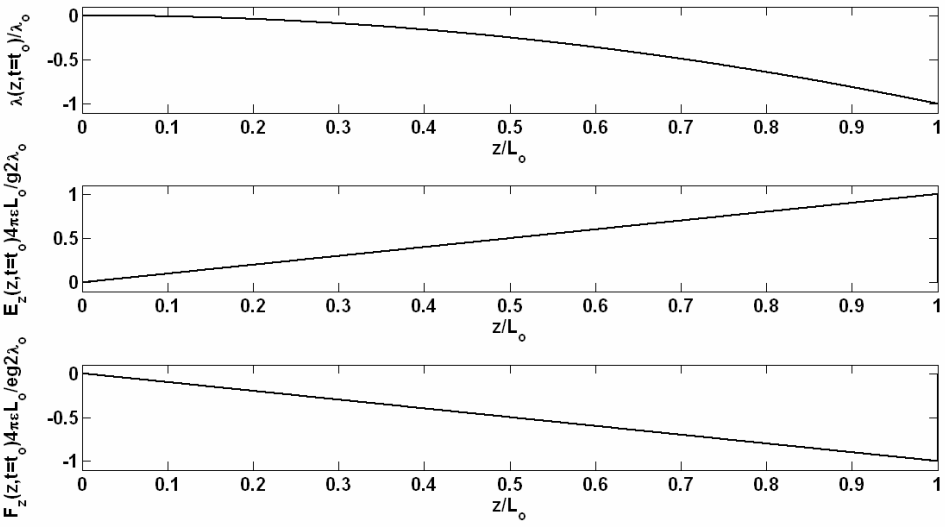

Fig. 2. 12. Normalized line-charge density, axial electric field and force at the bunch head.

In the central region of the bunch where the line-charge density remains constant, beyond L_o, the electric field and force is zero. This is shown in Fig. 2.13 below.

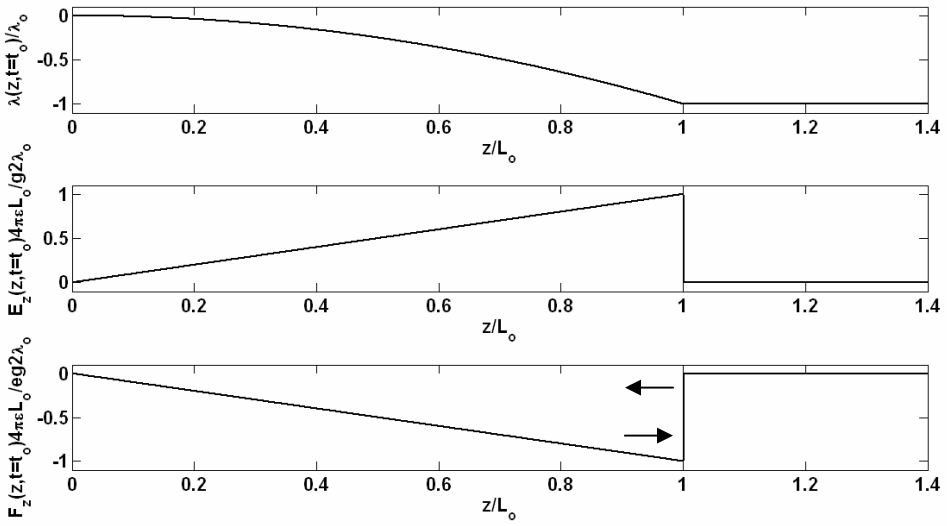

Fig. 2. 13. Normalized line-charge density, axial electric field and force beyond the bunch head, where the electric field and force is zero while the line-charge density remains constant.

If an assumption is made that a test particle within the head of the bunch is placed at the peak electric field $z = L_o$ (Eqn. 2.18), the test particle will "see" an image field as a result of the grounded central region. The test particle within head of the bunch will experience twice the force. The total force can be computed using (Eqn. 2.20).

$$F_z\left(z, t = \zeta\right) = \frac{-eg4\lambda_o z}{4\pi\varepsilon_o L_o^2},\ 0 \le z \le L_o \qquad \text{(Eqn. 2. 20)}$$

If the total work is computed over same length, we obtain the total energy (in Eqn. 2.21).

$$W = \Delta E = \int_0^{L_o} \frac{eg4\lambda_o z}{4\pi\varepsilon_o L_o^2} dz = \frac{2eg\lambda_o}{4\pi\varepsilon_o} \qquad \text{(Eqn. 2. 21)}$$

Using $E = \frac{1}{2} m\mathrm{v}^2$, we obtain the maximum velocity of the test particle in the bunch head within the beam frame (in Eqn. 2.22).

$$v = 2\sqrt{\frac{eg\lambda_o}{4\pi\varepsilon_o m}} \approx 2C_s \qquad \text{(Eqn. 2. 22)}$$

This derivation of the maximum expansion wave velocity assumes that the beam is non-relativistic, but it also confirms the theory presented in Sec. 2.2 of rectangular bunch erosion. The rarefaction wave velocity can be computed using the conservation of mass, since the total charge within the ends of the bunch is always conserved. The rarefaction wave, rarifies the central region of the beam at a velocity of C_s.

In order to put some of the theory presented in this chapter into perspective, Ch. 3 presents the University of Maryland Electron Ring, basic parameters, calculations as well as a few of the diagnostics that will be used throughout Ch 4, 5 and 6.

Chapter 3: UMER Diagnostics, Induction Focusing and Parameters

In this chapter we review the diagnostics used in the subsequent chapters; including the wall current monitor, beam position monitors (BPMs) and fast phosphor diagnostics. We then review the induction focusing system and end with a parameter description of UMER. The purpose of this chapter is to establish, for the reader, an understanding of UMER and the available diagnostics and tools.

3.1 Diagnostics

This section initially discusses how to use a parallel RLC circuit to measure the image current traveling on the beam pipe. A description of the BPMs is presented and then we end with a description of the fast gated camera and phosphor screen diagnostic.

3.1.1 Wall Current Monitor

The University of Maryland Electron Ring contains three breaks in the beam pipe with a glass insulator installed between the sections of pipe for the vacuum inside the system. These glass gaps (shown in Fig. 3.1 below) create the discontinuity in the conduction path for the image current or return current traveling along the beam pipe

[29]. The return current path is completed because of ground loops within the supporting structure of the accelerator.

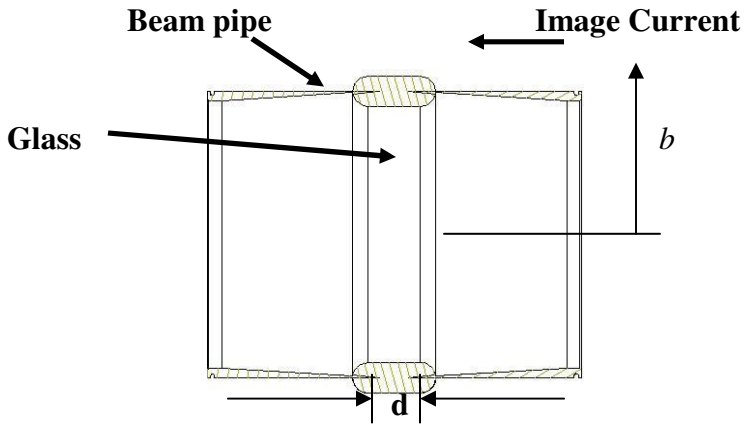

Fig. 3. 1. Cross-sectional view of a glass gap in the beam pipe. The gap length is 5.08 mm, where the pipe radius is 2.54 cm.

The radius b of the beam pipe is 2.54 cm and the gap separation, d, is 5.08 mm. The beam pipe is mounted to a support plate called a cluster plate with brackets that support the pipe. The electrical contact is made by the bracket and the pipe on either side of the glass gap (as shown in Fig. 3.2).

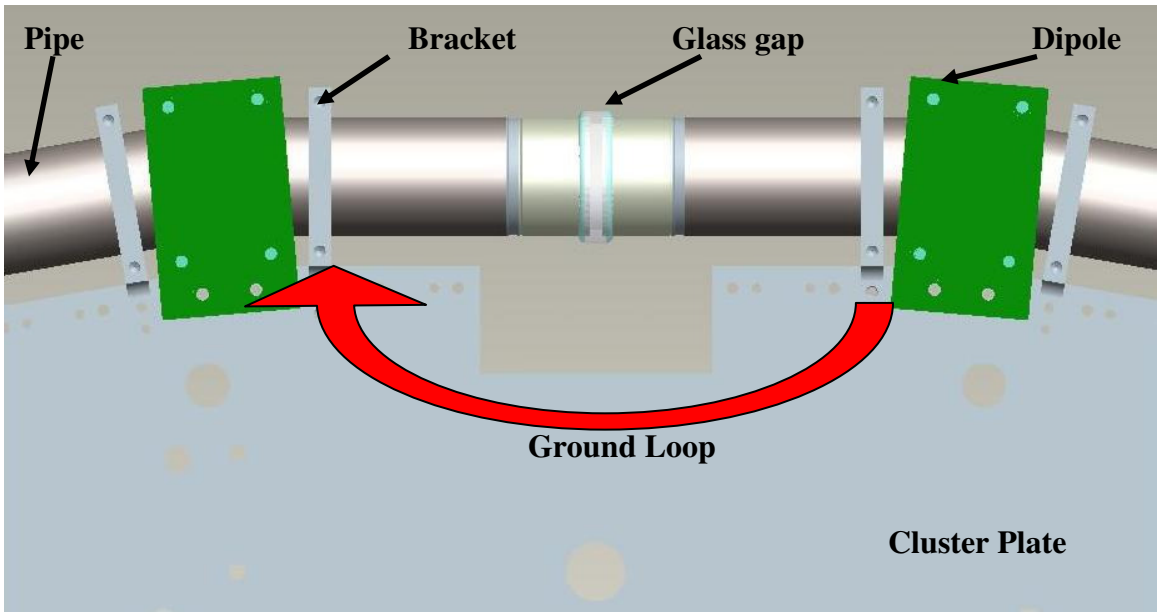

Fig. 3. 2. Cluster plate assembly. The beam pipe is held in place by the brackets mounted to the cluster plate. The green rectangles are the bending dipoles.

The inductance of the circuit is due to the ground loop through the cluster plate, which was estimated to be 7.5 nH. This inductance calculation will be reviewed in Sec. 3.3.3.

The L/R time constant for this circuit is extremely small, as a result of the large resistance of the glass gap. This leads to an induced voltage drop, across the gap, only during the rising/falling edges of a square beam current pulse. A short time constant for a high-pass filter means that the -3 dB point of the filter is large in frequency space.

In-order to lower the frequency of the pole so that we are able to measure the entire 100 ns beam pulse with minimal droop, we need to extend the time constant of the circuit by both adding resistance across the gap and loading a ferrite torrid to increase the inductance of the circuit. An acceptable L/R time constant for a 100 ns beam with a 2 % droop would be 4.95 μs using $1-e^{\frac{-t}{\left(\frac{L}{R}\right)}}$. Figure 3.3 below shows the current

directions in order to prevent any accidental shorts of the measurement using the oscilloscope.

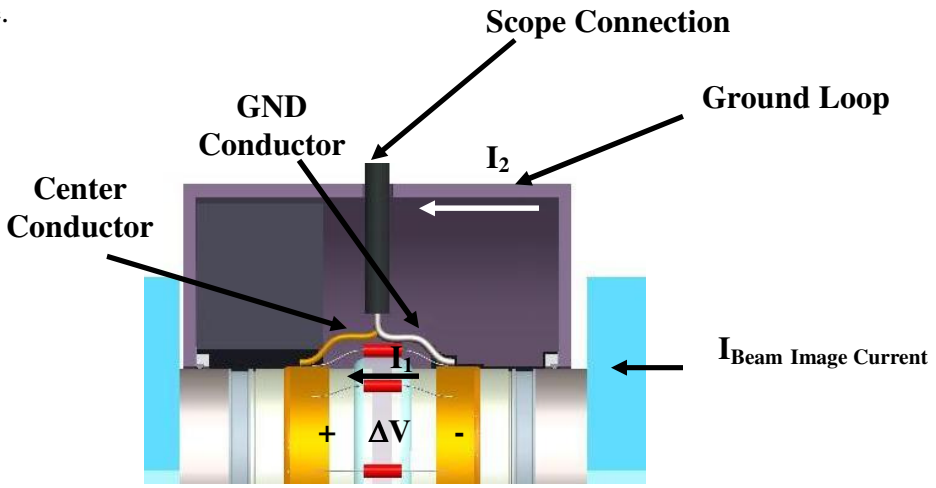

Fig. 3. 3. Diagram of the wall current monitor. The cyan rectangles are the quadrupoles on either side of the wall current monitor.

The beam image current is estimated from Eqn. 3.1, where R, L and ΔV is the total resistance, inductance and the measured voltage drop across the circuit.

$$I_{BeamImageCurrent} = I_1 + I_2 = \frac{\Delta V}{R} + \frac{1}{L}\int \Delta V dt \qquad \text{(Eqn. 3. 1)}$$

The capacitance term associated with the equivalent RLC circuit (shown in Fig. 3.4) has been neglected in the calculation as a result of the small RC time constant. Using the measured gap capacitance, 22 pF with a 2 Ω resistor across the gap, we obtain an RC time constant of 0.044 ns which corresponds to a frequency of 3.61 GHz. If the fastest rise time of the square beam current pulse is ~1 GHz, then the circuit will not loose any information in the beam up to the -3 dB point. The beam image current may also be calculated using a circuit solver, including the capacitive term. Similar calculations are shown in Sec. 4.1.1-4.1.2.

If we use a ferrite toroid with a measured inductance of 9.81 μH, then the low-frequency pole of the circuit will have a 4.9 μs time constant which would correspond

to a 2 % droop [57]. The ferrite properties relevant to its choice for UMER along with a calculation of the inductance will be discussed in Sec. 3.3.1-3.3.3.

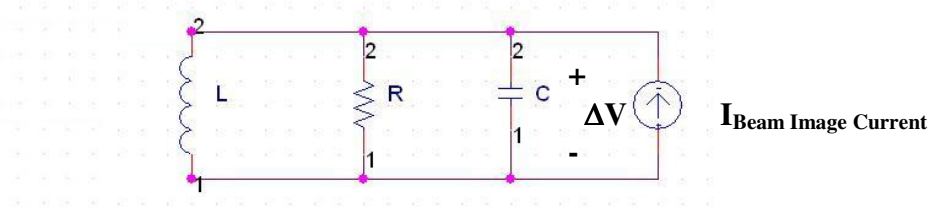

Fig. 3. 4. Equivalent RLC circuit with the beam image current displayed as an ideal current source.

In this equivalent circuit model, the beam image current is treated as an ideal current source with infinite impedance. The circuit contains two poles, a high-pass pole with a -3 dB point at $s = L/R$ and a low-pass pole with a -3 dB point at $s = 1/RC$. The net circuit forms a band-pass filter and has a frequency response shown in Fig. 3.5.

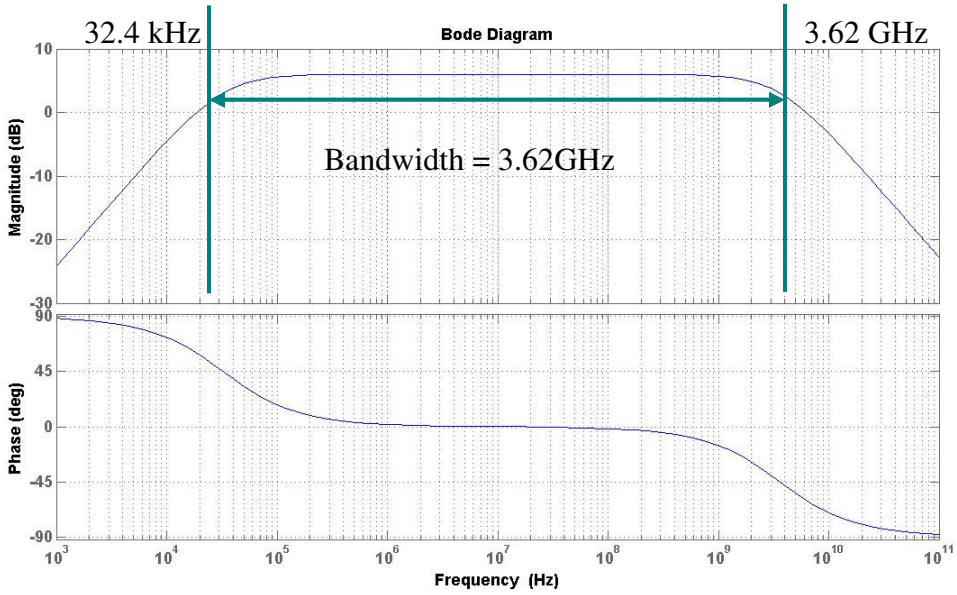

Fig. 3. 5. Bode plot of the wall current circuit model, where the lumped circuit components are (R = 2 Ω, L = 9.81 μH, C = 22 pF).

If any of the beam image current frequencies are within the pass-band of the circuit, then the impedance seen by the current will be 2 Ω. If any of those frequencies are outside of the pass-band, they will be attenuated. The following two sections, explain the available transverse diagnostics on UMER.

3.1.2 Beam Position Monitor (BPM)

One of the methods used to measure transverse position around the ring is with the capacitive beam position monitors (shown in Fig. 3.6). With these BPMs, located around the ring at discrete locations, we are able to obtain transverse position as a time-dependent electrical signal.

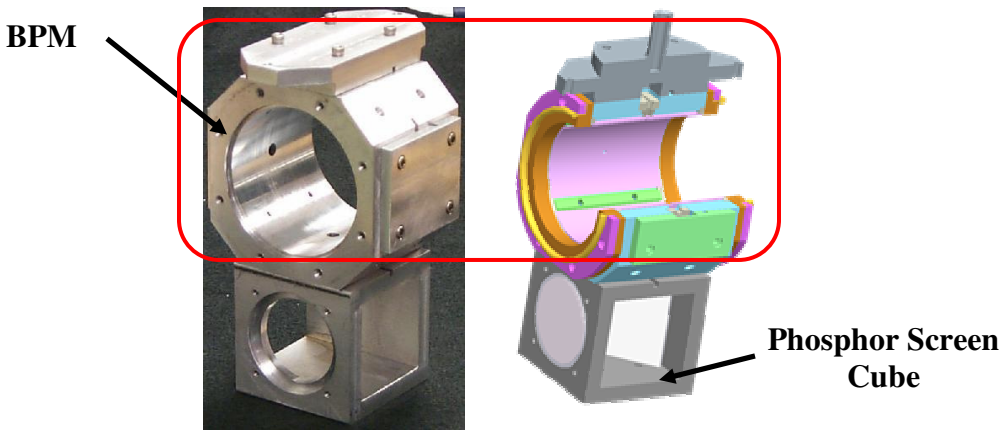

Fig. 3. 6. Beam position monitor (BPM) and phosphor screen cube assembly. Including both a picture and Pro-E drawing of the assembly.

The BPMs are composed of four individual plates that are equally spaced on four quadrants as shown in Fig. 3.7.

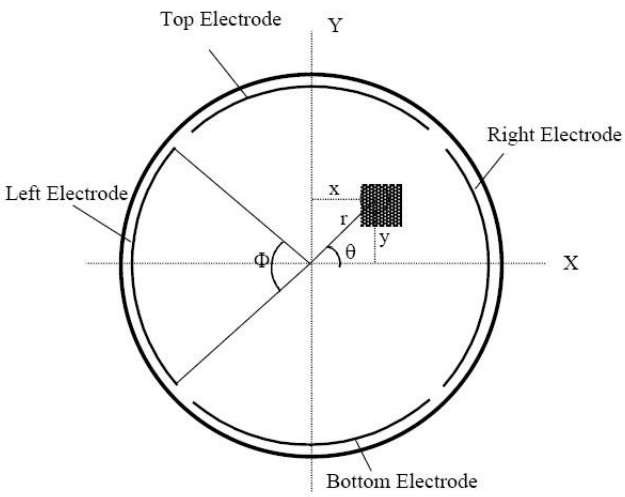

Fig. 3. 7. Beam position monitor (BPM) and phosphor screen cube assembly.

The voltage induced on any plate by a centered beam is calculated using Eqn. 3.2,

$$V = \frac{Q}{C} = \frac{\Phi L}{2\pi \mathrm{v}_o C} I_b \qquad \text{(Eqn. 3. 2)}$$

where C is the capacitance, L the electrode length into the page, Φ is the angle of the electrode and I_b is the beam current [57, 58].

If the beam is displaced from the center of the pipe, the induced voltages on the electrodes will change. It has been shown that the voltage induced may be calculated using Eqn. 3.3 and 3.4,

$$V_R(t) = \frac{-I_b(t)\ln(b/a)}{2\pi\varepsilon \mathrm{v}_o}\left[1 + \frac{4}{\Phi}\sum_{n=1}^{\infty}\frac{1}{n}\left(\frac{r}{b}\right)^n \cos(n\theta)\sin\left(\frac{n\Phi}{2}\right)\right] \qquad \text{(Eqn. 3. 3)}$$

$$V_L(t) = \frac{-I_b(t)\ln(b/a)}{2\pi\varepsilon \mathrm{v}_o}\left[1 + \frac{4}{\Phi}\sum_{n=1}^{\infty}\frac{1}{n}\left(\frac{r}{b}\right)^n \cos(n\theta)\sin\left[n\left(\pi + \frac{\Phi}{2}\right)\right]\right] \qquad \text{(Eqn. 3. 4)}$$

where θ and r relate to the beam position within the BPM (shown in Fig. 3.7). In order to decouple the left and right signals when the difference is taken to find position, the electrode angle Φ must be chosen such that the expansions in Eqn. 3.3

and 3.4 result in only odd terms. Each plate has a circular arc length that corresponds to 77^{o} [58]. The same is repeatable for the top and bottom plates.

3.1.3 Fast Phosphor Screen and Gated Camera

The another means of measuring transverse position of the beam is with the use of the 16-bit PIMAX2 ICCD camera (shown in Fig. 3.8) and fast-phosphor screen installed in the cubes below the BPMs (shown in Fig. 3.6).

Fig. 3. 8. 16-bit PIMAX2 ICCD Camera from Princeton Instruments.

With the Princeton camera, we are able to resolve first turn measurements of position and size at a minimum gate width of ~3 ns. This minimum gate width allows us to capture consecutive sliced images along the bunch, obtaining a third dimension of beam information. The imaging array of the camera is a 512 x 512 16-bit array that is sensitive in the regions between 280-to-780 nm [59].

As a result of the low light level from a 3 ns image, the number of integrations must be increased to approximately 100 integrations. UMER operates at 60 Hz (to be discussed in Sec. 3.4) and so the camera is triggered at that same frequency. One

hundred images of 16.66 ms totals 1.666 s of time required to capture each gated image. This is feasible only on a stable system, such as UMER otherwise any drift between images during the integration process will skew the images.

The phosphor screen (shown in Fig. 3.9) installed in the cube under the BPM, is a special fast phosphor with a time response of 2.4ns [60]. This is unlike typical P-43 phosphor screens where the time response of the phosphor is on the order of 1 ms [61]. The screen used in the experiments presented in Sec 4.2.1, is composed of a ZnO:Ga formula on a quartz plate. The screen is then coated with a conductive aluminum coating to protect it from current loading.

Fig. 3. 9. Fast Phosphor Screen.

When the beam pulse hits the screen, it emits light in the near UV which is within the spectral limits of the camera. The next section summarizes the induction cell system including comparisons between simulations and bench tests [62].

3.2 Induction Cell System

In this section, we will discuss how to use the parallel RLC circuit to apply a time varying potential difference across the glass gap. In this section we examine the simple high-voltage modulator model that will be used to produce the focusing fields

and compare the results to a bench test of the real circuit. We then combine the entire circuit model, including coaxial transmission line and induction cell, comparing both simulation to bench tests.

3.2.1 Simple High-Voltage Modulator Model

A prepackaged switch made by BEHLKE was the best candidate for this application since we needed to apply focusing fields (to be explained in Sec. 5.1) with varying amplitude and short width into a low impedance load [63]. The specifications for the HTS 80-12-UF are displayed in Table 3.1.

Table 3. 1. Specifications of HTS 80-12-UF [63]

Parameter	Value
V_{MAX}	8 kV
I_{PEAK}	120 A
Pulse Width	10 ns
Closed-state Resistance	4.5-11.3 Ω
t_{ON} Delay	60 ns
t_{ON} Rise-time	2.0 ns

The high-voltage modulator is composed of two HTS units connected in a bipolar arrangement to provide a positive focusing field as well as a negative focusing field. Since the circuit internals are not provided by the manufacturer, a simple switch model (shown in Fig. 3.10) that takes into account the specifications of the HTS units was developed in-order to simulate the circuit in Cadence [64].

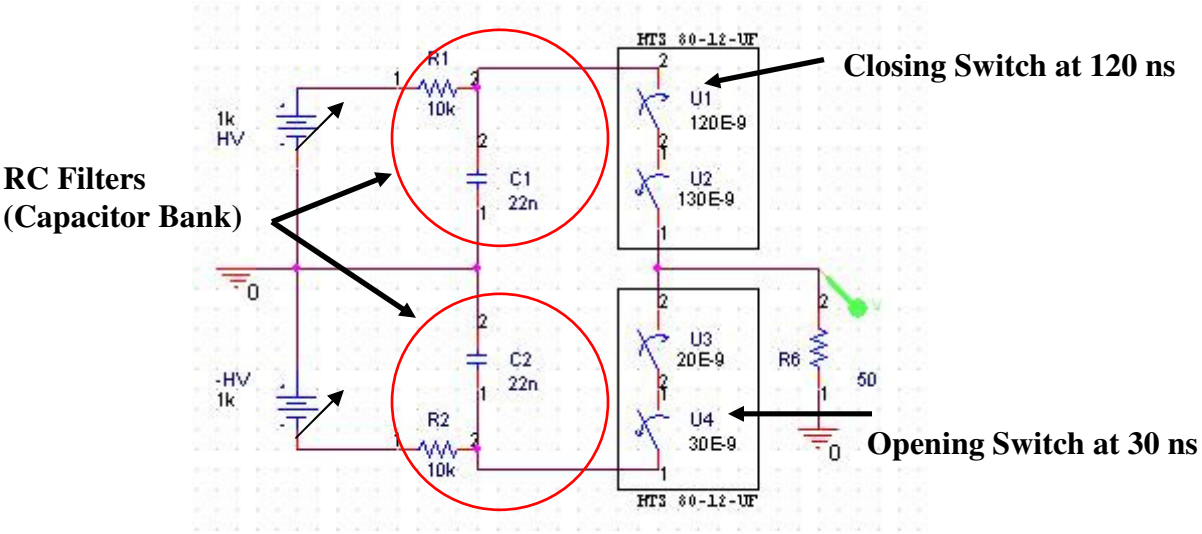

Fig. 3. 10. Simple high-voltage modulator circuit model comprised of two HTS units with a capacitor bank. Each HTS unit is modeled as a series combination of both an on-switch and an off-switch.

Each HTS 80-12-UF unit was modeled with both an ideal on-switch and an ideal off-switch in series with a rise and fall time of 2.0 ns each. The closed-state resistance of the individual switches is 2.25 Ω so that each pair is equal to 4.5 Ω. The open-state resistance was arbitrarily set to 1 Meg Ω since it was not specified in the BEHLKE literature. Each switch pair was modeled such that the period of time that both the positive and negative pair is **on** was 10 ns, as specified in the literature. The RC filters (Capacitor Bank) shown in the circuit are used as charge storage elements. The charging time for both of them is 0.22 ms, thus if the system is pulsed at 60 Hz the filters have plenty of time to re-charge between each 16.666 ms period.

A Cadence circuit simulation of the modulator was performed where both HTS units were pulsed and compared with bench test results of the same circuit. The voltage across a 50 Ω resistor is shown in Fig. 3.11.

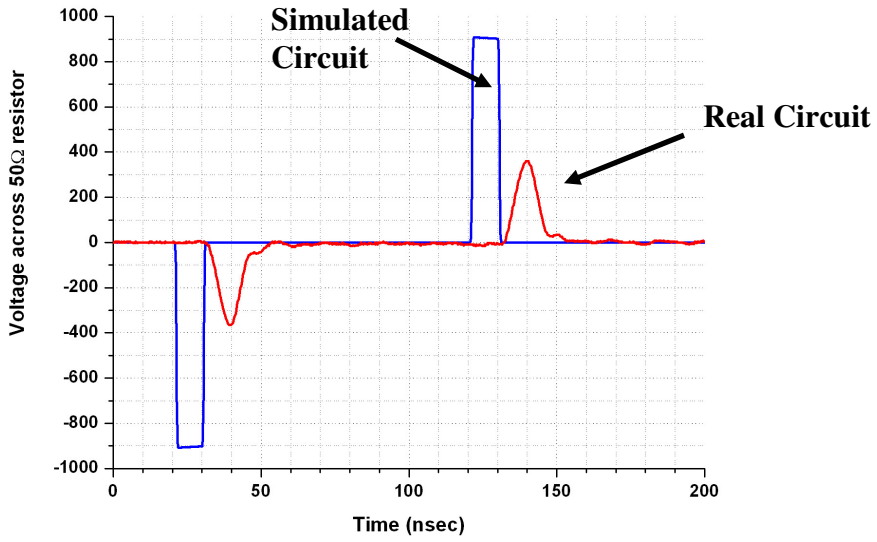

Fig. 3. 11. Simulated (blue) and bench test (red) results of the modulator output across a 50 Ω resistor.

The comparison of bench test results and simulation shows that the simulation does not model the actual circuit as a result of the inaccurate specifications from the manufacture. Both the peak amplitude of the pulses and the rise times do not correspond with the bench test results. The bench test data was taken with a 1 GHz oscilloscope and a 1 GHz 100x probe, so the measurement apparatus should not be the cause of this discrepancy. There may be parasitic capacitances affecting the pulse from the switches or there may be a problem with the specifications of these switches.

In either case, in order for the Cadence model to better simulate the real modulator, the rise and fall times of each switch as well as the period of time that both switches are closed was modified. The rise and fall times of the ideal switches were changed from 2 to 40 ns and the period of time that both switches are "closed" was changed from 10 to 15.3 ns. The simulation was repeated with the modifications to the switch specifications as discussed and the results are shown in Fig. 3.12.

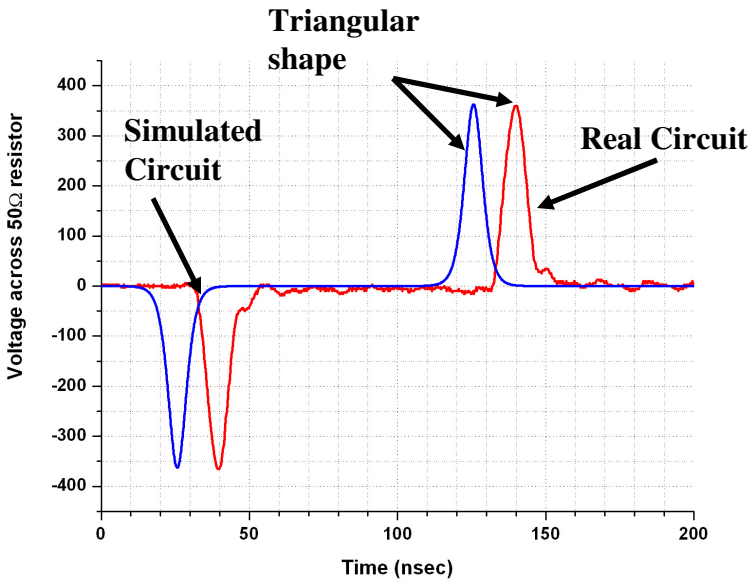

Fig. 3. 12. Comparison between bench tests and circuit simulations, including the added modification to the ideal switch specification. Simulated (blue) and bench test (red) results of the modulator output across a 50 Ω resistor.

These particular pulse specifications reproduce the triangular shaped pulses from bench test results across a 50 Ω resistor. The FWHM from the bench was 8.8 ns and the simulated FWHM was 7.39 ns, such that the real circuit is slightly wider in width. The reason that the pulse does not reach the full potential provided by the resistive divider, including the internal switch resistance and the 50 Ω, is a result of a shorter switch **on** period then the actual rise time of the switch; there by reducing the pulse amplitude by 62%. The following section presents the circuit model for a coaxial transmission line that will be used to connect both the cell and the modulator together.

3.2.2 Transmission Line Circuit Model

General two-wire transmission lines are used everywhere in the lab. In the induction cell system, a segment of transmission line connects the high-voltage

modulator to the induction cell. The type of transmission line used is RG-58 coaxial cable. Such a transmission line is modeled as a differentially lumped circuit distributed along the length of the transmission line (as shown in Fig. 3.13). For a differential length Δx, the elements that make up the model are two series elements, the resistance per unit length and inductance per unit length and a shunt element as the capacitance per unit length.

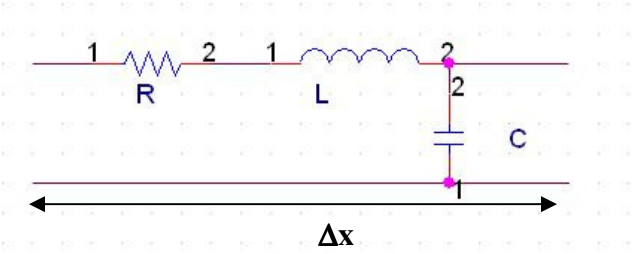

Fig. 3. 13. Lumped circuit model for a differential length Δx of transmission line.

The capacitance and inductance per unit length for a coaxial transmission line lumped circuit model (shown in Fig. 3.13) are the Eqns 3.5 and 3.6 respectively,

$$C = \frac{2\pi\varepsilon}{\ln\left(\frac{b}{a}\right)} \qquad \text{(Eqn. 3. 5)}$$

$$L = \frac{\mu}{2\pi}\ln\left(\frac{b}{a}\right) \qquad \text{(Eqn. 3. 6)}$$

where a is the radius of the inner conductor and b is the radius of the outer conductor [65]. The transmission line cross-sectional view of length Δx, is shown in Fig. 3.14.

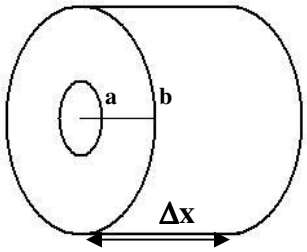

Fig. 3. 14. Cross-sectional view of a coaxial transmission line of length Δx.

The resistance is usually measured since it is dependent on the material used and if it is stranded versus solid for the center conductor. The measured values for RG-58 as given from BELDEN are displayed in Table 3.2 [66].

Table 3. 2. RG-58 Specifications [66].

Parameters	Values
Capacitance/Δx	30.8 pF/ft
Inductance/Δx	0.077 μH/ft
Resistance/Δx	10.8 Ω/1000ft

$$Z_o = \sqrt{\frac{L}{C}} \qquad \text{(Eqn. 3. 7)}$$

The impedance of the cable is calculated using Eqn. 3.7, which for the specifications listed, is 50 Ω. Section 3.2.3, analyzes the circuit model of the induction cell prior to compiling the entire circuit.

3.2.3 Induction Cell Circuit Model

The induction cell (shown in Fig. 3.18a-b) is similar to the wall current monitor (shown in Fig. 3.3), since both utilize a parallel RLC circuit. They are tuned differently and as a result the bandwidth of both devices is different. One is tuned to optimize the droop in the measured current and the other is optimized to match the modulator to the 50 Ω coaxial transmission line. This modifies the poles of the

circuit and equivalently its bandwidth. The bode plot of the pass-band range of the induction cell (shown in Fig. 3.15) is reduced from that of the wall current monitor shown in Fig. 3.5.

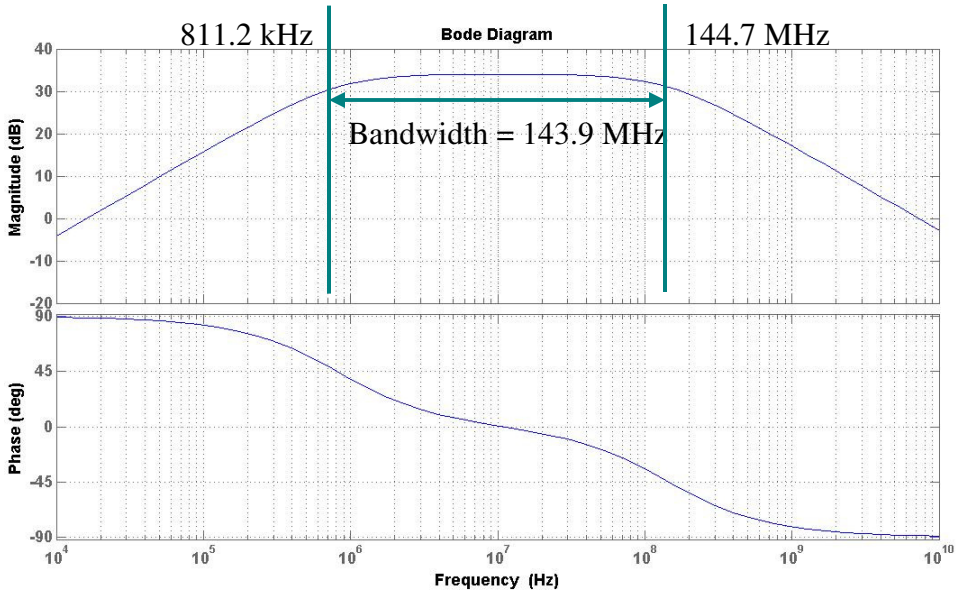

Fig. 3. 15. Bode plot of the induction cell circuit model (R = 50 Ω, L = 9.81 μH, C = 22 pF).

This modification of the resistance increases the low frequency pole to 811 kHz and lowers the high frequency pole to 144 MHz. If the induction cell was used to measure beam current, the calculated droop of the current monitor would be 40% for the 50 Ω resistor, resulting in a poor reproduction of the rectangular current pulse. Reducing the bandwidth also limits the frequency of the signal that may be applied to the induction cell. It is critical that the applied focusing fields are within the bandwidth of the induction cell, otherwise the modulator output may in effect become shorted. The last section, Sec. 3.2.4, completes this discussion and compiles the individual circuit components.

3.2.4 Induction System Circuit Model

The entire circuit (shown in Fig. 3.16) consists of the bipolar modulator, the induction cell and a segment of transmission line connecting the two.

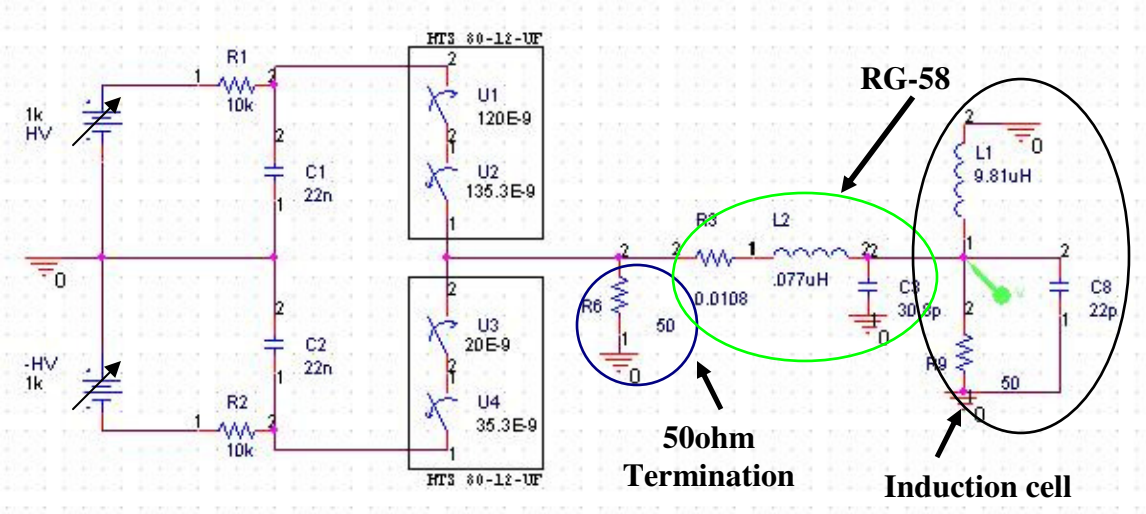

Fig. 3. 16. Induction cell system circuit model drawn in the Cadence circuit simulator.

Each section of the circuit is outlined with circles and labels. A 50 Ω resistor, before the segment of RG-58, has been added and an explanation is to follow.

Once a pulse from the modulator is sent down the transmission line to the induction cell, the current will split up into the three elements of the parallel RLC circuit. When the modulator stops pulsing, an induced pulse is reflected back up the transmission line to the modulator which reflects again back down the transmission line because of the high impedance open-state of the BEHLKE switches, as a result of the $\Gamma = \frac{Z_L - Z_O}{Z_L + Z_O} = \frac{1Meg - 50}{1Meg + 50} \approx 1$. A 50 Ω resistor is placed at the modulator side of the transmission line so that the pulse stops reflecting back into the induction cell producing more then one focusing field.

A Cadence simulation of the entire circuit allows enough time for both HTS circuit models to send a pulse to the induction cell as shown in Fig. 3.17. The simulation output along with the real circuit output displays the voltage across a 50 Ω resistor inside the induction cell.

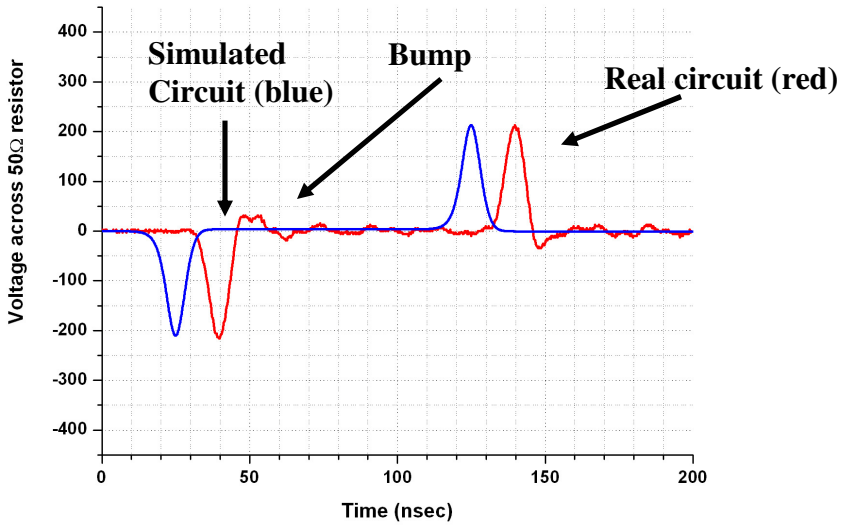

Fig. 3. 17. Simulated (blue) and bench test (red) resulting output across a 50 Ω resistor inside the induction cell.

The simulation results compare very nicely with the real circuit performance. The amplitude has decreased from 364 volts in Fig. 3.12 to 210 volts in Fig. 3.17, with the additional components attached for the same 1 kV charge on the capacitor bank. The next section details the ferrite considerations and limitations of the induction cell.

3.3 Ferrite Considerations and Limitations

In this section, we will analyze the saturation limits of the ferrite material in terms of the volt second product and briefly explain how the circuit operates to prevent

saturation of the material. We also review calculations of the power dissipated in the ferrite and suggest methods to minimize power dissipation, ending with the inductance calculation of the ferrite core.

3.3.1 Volt-Second Product

The induction-cell system is comprised of a modulator that drives a current density $\vec{J}$ around a ferrite toroid (Fig. 3.18a), creating a time varying magnetic field intensity inside the ferrite toroid equal to $\vec{H} = \frac{\vec{J}A}{2\pi r}$, where the cross-sectional area is $A = xy$. Because of Lenz's law, an equal and opposite current is generated to oppose the change in flux equal to the induced current [62, 67-70]. The maximum induced voltage across the gap is given by the $\frac{d\vec{B}}{dt}$ term of the ferrite. If this term goes to zero, an electrostatic condition in Faraday's law is reached, namely $\nabla \times \vec{E} = 0$. This condition is reached at the peak of the materials hysteresis curve, the saturation point (B_S), where the magnetic flux density does not change anymore with a change in magnetic field intensity. To calculate the maximum ΔB of the material with the given pulse parameters we use the following relationship (Eqn. 3.8),

$$\Delta V \Delta t = \Delta BA \qquad \text{(Eqn. 3. 8)}$$

where $\Delta V \Delta t$ is the volt-second product and ΔBA is equal to the product of the cross-sectional area A of the core and the change in magnetic flux ΔB. The ferrite material chosen was CMD5005, since the saturation flux is well above the typical flux swing of the circuit [62, 71].

The induction cell (shown in Fig. 3.18a) is installed on the beam pipe and is held in position by the cluster plate. The blue rectangles are the quadrupoles and the green rectangles are the dipoles. The current loop around the induction cell housing is shown in red. A more detailed view of the induction cell is shown in Fig. 3.18b, including the glass gap (discontinuity in the beam pipe) and resistor array that straddles the gap.

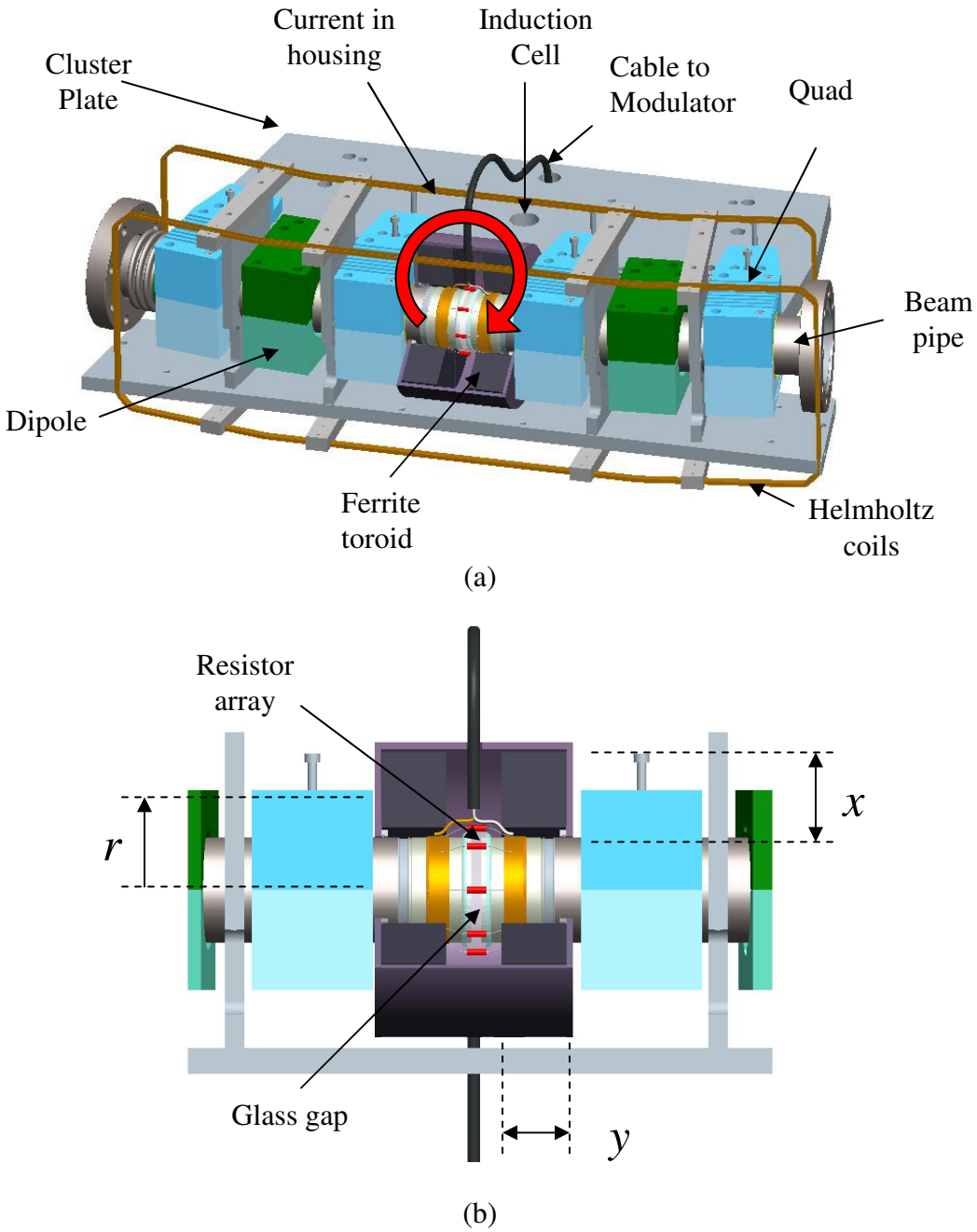

Fig. 3. 18. (a) Pictorial diagram of the induction-cell installed on the cluster plate, including a red loop to represent the curl of the electric field. A more (b) detailed view of the induction cell is shown below.

In order to pulse the ferrite cores, we must be able to reset the material as well as keep it from over heating. The following two sections, describe how to reset the cores and calculate the power loss within the core material.

3.3.2 Resetting Ferrite Core

In order to prevent the material from inducing a large back emf, we must apply a reset pulse with opposing polarity and of equal volt-seconds (as shown in Fig. 3.19).

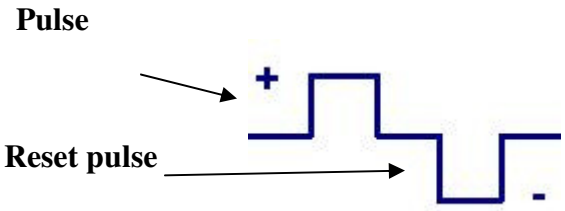

Fig. 3. 19. Pulse configuration that supports each pulse of the ferrite material with an equal and opposite reset pulse.

Typically a negative pulse in the form displayed in Fig. 3.19 is applied in the reverse direction from the initial pulse, driving the material back down the hysteresis curve, **resetting** the core [72]. This configuration may also be used to decelerate the beam coming through the induction cell if the modulator that supplies the negative pulse is triggered while the beam is still in the induction cell. The same is true for beam acceleration. The following section ends with an explanation on the calculation of power loss in a ferrite core and the inductance of the ferrite.

3.3.3 Power Loss in the Ferrite Core

The power loss within the ferrite material must also be considered in order to prevent the material from reaching the Curie temperature as a result of the joule heating, rendering it useless as a ferrite. The curie temperature of CMD5005 is 130 ^{o}C [71].

The loss is calculated using the loss curve (shown in Fig. 3.20) for the given material, where the horizontal axis is the rise-time of the applied pulse in microseconds for full saturation and the vertical axis is the loss in J/m^3. If we have a field of 57.4 gauss in the ferrite for a pulse rise time of 10 ns, then the approximate time to reach full saturation for CMD 5005 would be 557 ns, using the saturation flux density of 3200 gauss [62, 71]. The loss in the ferrite would be approximately 110 J/m^3 for full flux swing, so the loss would be 38.2 mJ assuming a material volume of 0.000347 m^3.

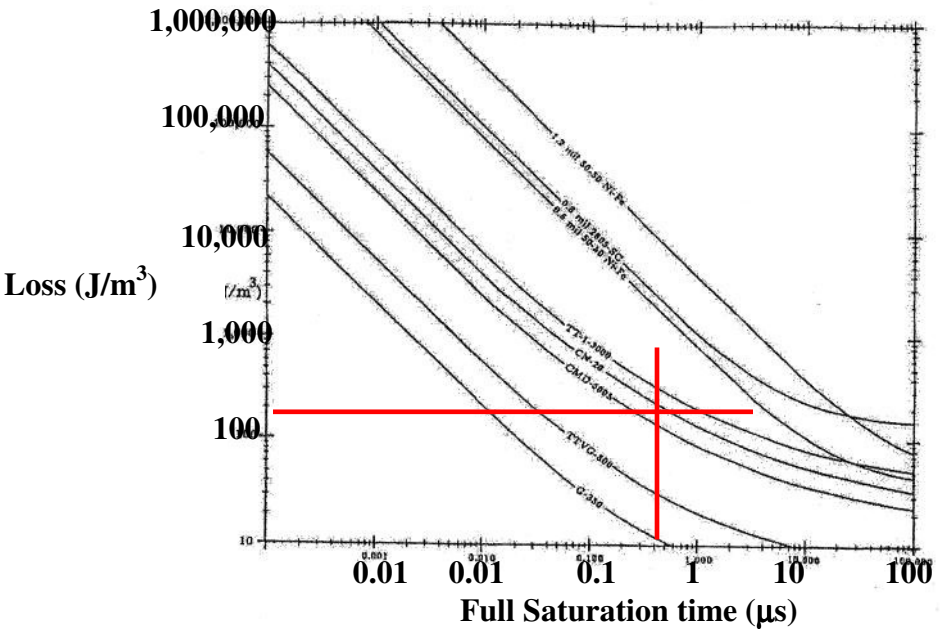

Fig. 3. 20. Power loss curve for CMD 5005 and other materials [71, 72].

Another method of minimizing the loss would be to slow the rise time of the modulator reducing the J/m^3 loss in the material. If we estimate the power loss from a DC signal, no energy would be loss in the ferrite. Most of the loss would be in the DC power dissipated in the wire wrapped around the ferrite material.

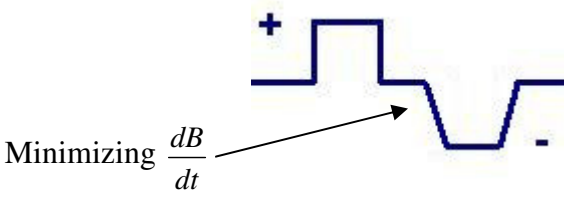

Fig. 3. 21. Reset pulse with minimized $\frac{dB}{dt}$.

To calculate the inductance of the ferrite toroid, we use the formula for the coax cable, Eqn. 3.6. The initial permeability of the ferrite as specified from CMI is 1300 [71]. The outer radius of the toroid is 6.6 cm and the inner radius is 3.0 cm. The height of the material is 3.1 cm and so the calculated inductance of the toroid is 7.93 μH. The measured value used in simulations and other calculations is 9.81 μH. The difference between the measured versus calculated inductance may be a result of an incorrect estimate of the initial permeability.

To measure the approximate inductance due to the ground loop through the cluster plate, we divide by the initial permeability of the ferrite using the ferrite as an amplifier. The calculation yields 7.5 nH. The next section presents a basic outline of UMER.

3.4 UMER

The University of Maryland Electron Ring (UMER) system parameters, used throughout this document, are described in this section. The calculations of beam size and experimental setup are shown in the appendix, sections A.1 and A.2. The system parameters include the basic details of the ring, beam energy, average bunch size and emittance for each of the injected beam currents.

The beam bunch emerges from the gun as a constant current, constant velocity rectangular pulse measured by the Bergoz non-intercepting current monitor (shown in Fig. 3.22).

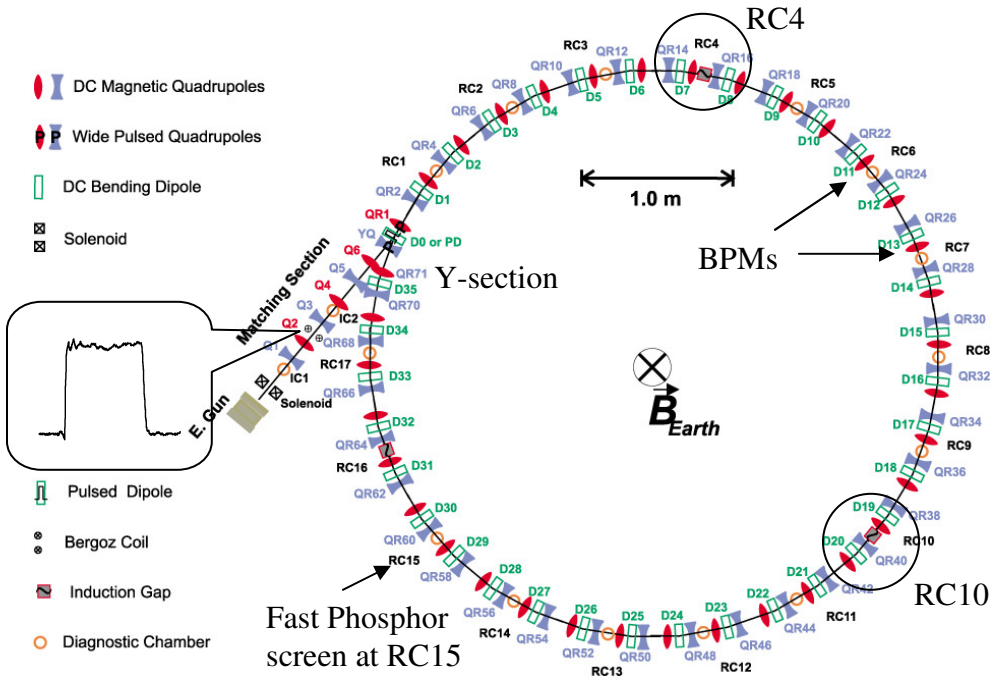

Fig. 3. 22. Lattice optics diagram with the RC4 induction-cell and RC10 wall current monitor circled. An example rectangular beam current profile is shown in the caption. Two of the 14 available BPMs are labeled in the figure as well as the placement of the fast phosphor screen at RC15.

Figure 3.22 is a schematic diagram of the UMER ring showing the placement of the various ring elements, from BPMs to the induction cell and wall current monitor as well as the fast phosphor screen at RC15. The beam and lattice parameters for the experiments presented in this document are displayed in Table 3.3.

Table 3. 3. UMER main parameters.

Injected Beam Energy (keV)	9.967
$\beta = \mathrm{v}/c$	0.19467
Pulse Length (ns)	101.56
Ring Circumference (m)	11.52
Lap Time (ns)	197.39
Pulse Repetition Rate (Hz)	60
FODO Period (m)	0.32
Zero-Current Phase Advance σ_0	66.5^o
Zero-Current Betatron Tune v_0	6.65

An aperture wheel, approximately 1 cm downstream of the anode, is used to inject different beam currents. The aperture radius and corresponding beam currents are listed in Table 3.4 below.

Table 3. 4. Aperture radius and beam current exiting the gun

Aperture Radius	Beam Current (mA)
0.25 mm	0.6
0.875 mm	6
1.5 mm	21
2.85 mm	78
Full Beam	104

Once any of the five possible beams are injected into the ring, 36 FODO cells contain the beam transversely within a pipe radius of 25.4 mm. The average beam radii of the five different beam currents, calculated using the smooth focusing approximation, for two ring operating points with quadrupole currents equal to 1.82 and 1.84 A, are displayed in Table 3.5 and 3.6 respectively [12, 60].

Table 3. 5. Beam parameters at quadrupole read current of 1.820 A.

Beam current (mA)	0.6	6	21	78	104
Average Beam radius (mm)	1.58	3.38	5.16	9.60	11.03
$\varepsilon_{n,\,rms}$ (μm)	0.39	1.3	1.5	3.0	3.2

Table 3. 6. Beam parameters at quadrupole read current of 1.840 A.

Beam current (mA)	0.6	6	21	78	104
Average Beam radius (mm)	1.57	3.35	5.10	9.49	10.89
$\varepsilon_{n,\,rms}$ (μm)	0.39	1.3	1.5	3.0	3.2

The injector is a single turn injection scheme where the gun and injection magnets are pulsed every 16.666 ms, resulting in a new beam on every cycle. The induction-cell is installed at ring chamber 4 (RC4) located 3.74 m from the gun and the wall-current monitor is installed at ring chamber 10 (RC10) located 3.84 m away from RC4 (as shown in Fig. 3.22). The distance between BPMs installed in the ring is 0.64 m or two FODO cells where a FODO cell period is 0.32 m (as shown in Table 3.3).

The next three chapter's present experiments on longitudinal dynamics using the hardware described in this section. Longitudinal containment of the bunch is investigated as well as the correlation of the transverse dynamics to the longitudinal physics.

Chapter 4: Experimental Investigations of Rectangular Bunch Erosion and Longitudinal-Transverse Dynamics

Before exploring the effects of longitudinal confinement, we present a study on the bunch-end dynamics of the unconfined bunch, comparing experimental measurements with analytical solutions and Particle-In-Cell (PIC) simulations. Particles accelerated out from the central region of the bunch are affected by the transverse effects as a result of the correlated longitudinal energy profile along the bunch. Using the information gained in this chapter about the various measurements, calculations and simulations, we are able to estimate bunch-end energies and, correspondingly, the induced tune shifts and centroid displacements as a result of the lattice dispersion. Understanding the bunch dynamics without the use of longitudinal focusing establishes its necessity.

4.1 Study of Rectangular Bunch Erosion

We first compare measurements of beam current profiles with theoretical calculations and simulations, to confirm our understanding of the rectangular bunch erosion.

4.1.1 Experimental Observations and Comparison to Theory

We measure the bunch-end erosion per turn using the RC10 wall-current monitor, to check agreement with analytical calculations (as discussed in Sec. 2.2, within the simple-wave limit). Using experimental beam parameters (presented in Sec. 3.4) and Eqns. 2.7, we analytically calculate the current profiles which are then provided to a cadence circuit solver to emulate the response of the wall current monitor (discussed in Sec. 3.1.1) at RC10 [64]. Figures 4.1, displays the comparison between experimental measurements and analytical calculations for three injected beam currents. The theoretical model (in Sec. 2.2) assumes a linac geometry such that the calculations do not account for overlapping within the simple-wave region. We terminate the experiment after a given number of turns because the head and tail begin to overlap, diverging from the assumptions used in the theory.

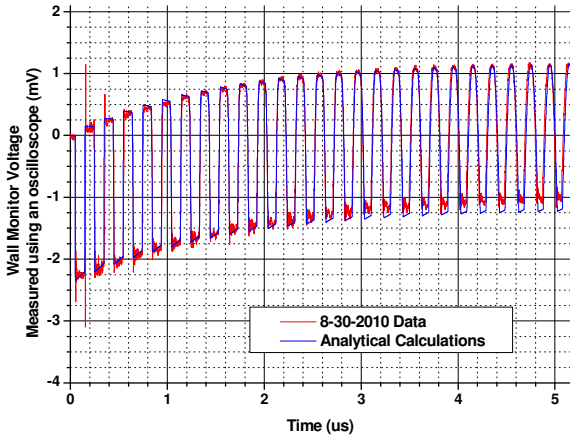

(a) 0.6 mA

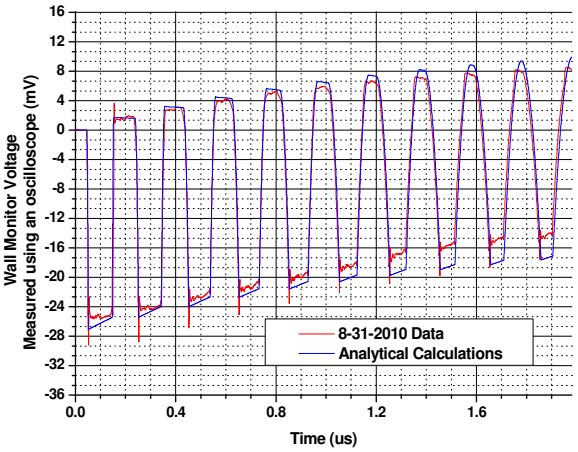

(b) 6 mA

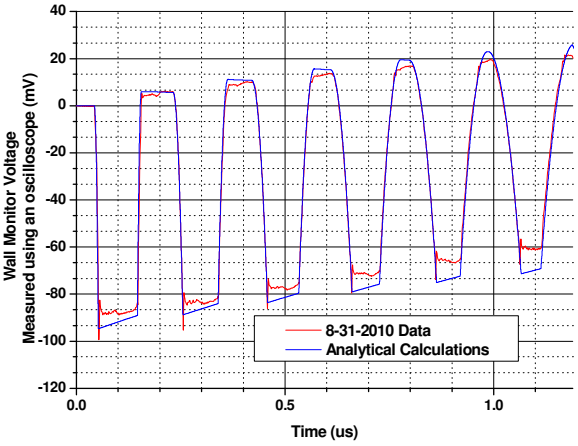

(c) 21 mA

Fig. 4. 1. Beam current (at the RC10 wall-current monitor) as a function of time for (a) 0.6 mA; (b) 6 mA; (c) 21 mA peak injected current, comparing experiment (red) with analytical calculations (blue).

The measured current profiles (shown in Fig. 4.1) are similar to the analytical profiles. The erosion rates of the head and tail appear to match fairly well with the calculated current profiles (analyzed in Sec. 5.1.1), though the peak currents are not equal. There appears to be a current loss mechanism in the experiment that is not represented in the calculations. The erosion rate is a function of C_s (Eqn. 2.3), which is then a function of beam current as well as beam size. In order for the sound-speed C_s (or erosion rate) to remain constant, the ratio $g\lambda_o$ in Eqn. 2.3, must remain the same. For example, if the beam current drops by 15% for the 21 mA beam at the 6th turn (as in Fig. 4.1c); the g-factor must increase by 17.6%. Using the g-factor definition (in Eqn. 2.4), the beam radius must decrease by 24.6% in order for C_s to remain constant. This compensating mechanism may be one of the reasons that the erosion rate remains constant over the first few turns, resulting in a current loss and decrease in beam size for the 21 mA beam.

Since the analytical calculations are not valid outside the simple-wave region, other means must be used to track the physics beyond the point where the beam begins to overlap. Numerical simulations allow us to get around that difficulty by using self-consistent field solvers. The following section presents the same experimental data along with WARP simulations.

4.1.2 Particle-In-Cell (PIC) Simulations

The simulated current profiles using WARP (as discussed in Sec. 2.2.2) were processed in a similar fashion to the analytical calculations. The current profiles at

each turn are provided to the circuit solver, resulting in the emulated voltage profiles shown below in Figures 4.2 for the three beams.

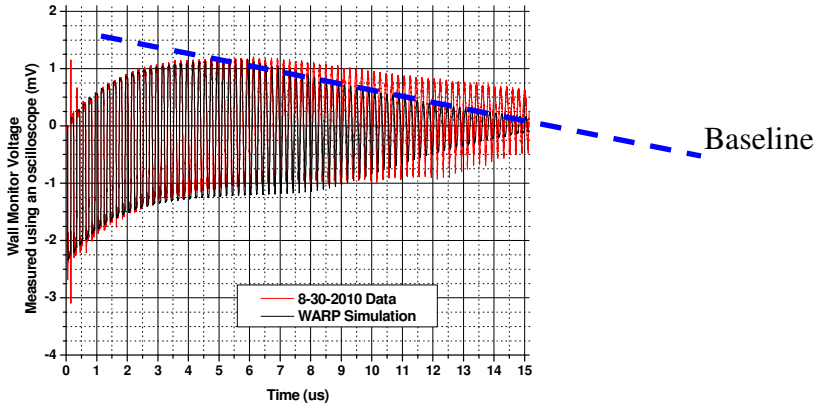

(a) 0.6 mA

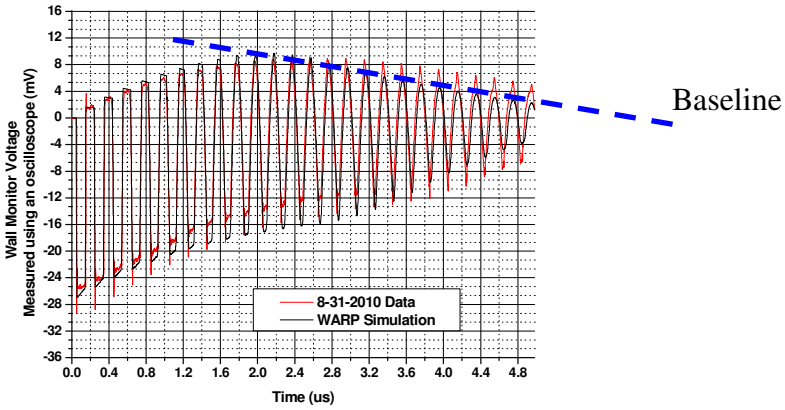

(b) 6 mA

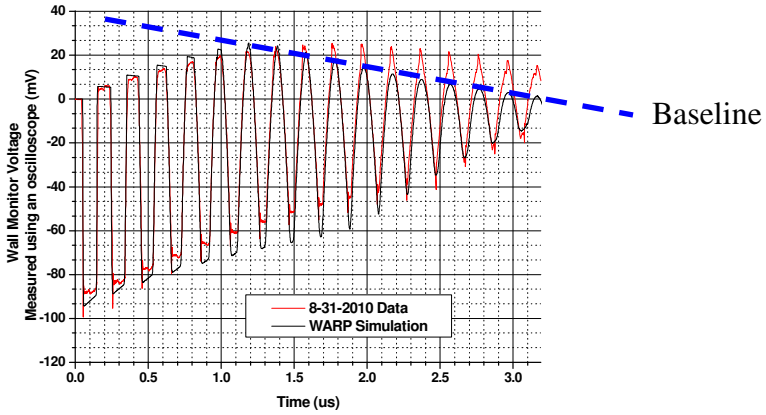

(c) 21 mA

Fig. 4. 2. Beam current (at the RC10 wall-current monitor) as a function of time for (a) 0.6 mA; (b) 6 mA; (c) 21 mA peak injected current, comparing experiment (red) with PIC simulations (black).

The simulations were completed using the R-Z model of WARP, with a 64 x 256 grid that moves with the beam (beam-frame simulation). The total number of macroparticles in the simulation was 10 million with a step of 10 cm or approximately 1.71 ns. The initial longitudinal thermal spread in the simulation was 1.5×10^5 m/s corresponding to a 50 eV intrinsic energy spread. The simulated current profiles (shown in Figure 4.2 above) are similar to the analytical profiles, as they do not represent the current loss within the experiment. Because the R-Z model assumes a perfectly centered beam, the simulation is less susceptible to transverse losses from scraping [73]. Despite the observed losses, the agreement between experiment and simulated current profiles is still fairly good. The erosion rates at the beginning of the multi-turn transport appear to agree with simulations in all three cases (analyzed in Sec. 5.1.1). As the beam enters the non simple-wave region of transport, the simulated baselines do not agree with the experimental measurements. These comparisons may be difficult to interpret without other experimental means, though simulation may be used to estimate the current-dependent baseline shifts [74, 75].

In order to obtain better agreement between simulation and experimental results, one method of imposing a loss mechanism within the simulation is through the modification of the particle weights. This results in a current loss mechanism that is programmable over the duration of beam transport. Using this method of current loss, we have been able to obtain much better agreement with experimental measurements [75].

Both analytical calculations and simulation reconstruct the rectangular bunch profiles. The analytical calculations are valid only within a given period of transport,

though they require less time to calculate as opposed to PIC simulations. The PIC simulation can take a day or more, given the correct simulation parameters, but we are able to reconstruct the profiles beyond the simple-wave region where the analytical solutions are not valid.

4.2 Measurements of Chromatic Effects due to a Correlated Energy Profile

This section describes three experimental methods I have used to indirectly measured tune and energy as a function of beam length. These methods come out as a result of the lack of an energy analyzer in UMER to directly measure the energy profile along the bunch. Two of the techniques are primarily single turn measurements and the other is averaged over multiple turns.

The following section, presents the correlation between the longitudinal and transverse dynamics as well as the resulting effects of bunch-end erosion on the transverse measurements.

4.2.1 Head and Tail Sliced Centroid Displacement

As space-charge pushes particles in the head and tail of the bunch to different energies from the injected energy, the ring dispersion causes a measurable correlated centroid displacement along the bunch. The diagnostic used was the combination of a fast phosphor screen and a fast-gated imaging camera (schematic shown in Fig. 4.3),

allowing us to measure the transverse beam displacement as a function of beam length. This method is feasible since it is able to resolve screen images to ~3 ns (minimum camera gate width), which is short relative to the length of the head and tail at RC15 for the 21 mA beam on the first turn.

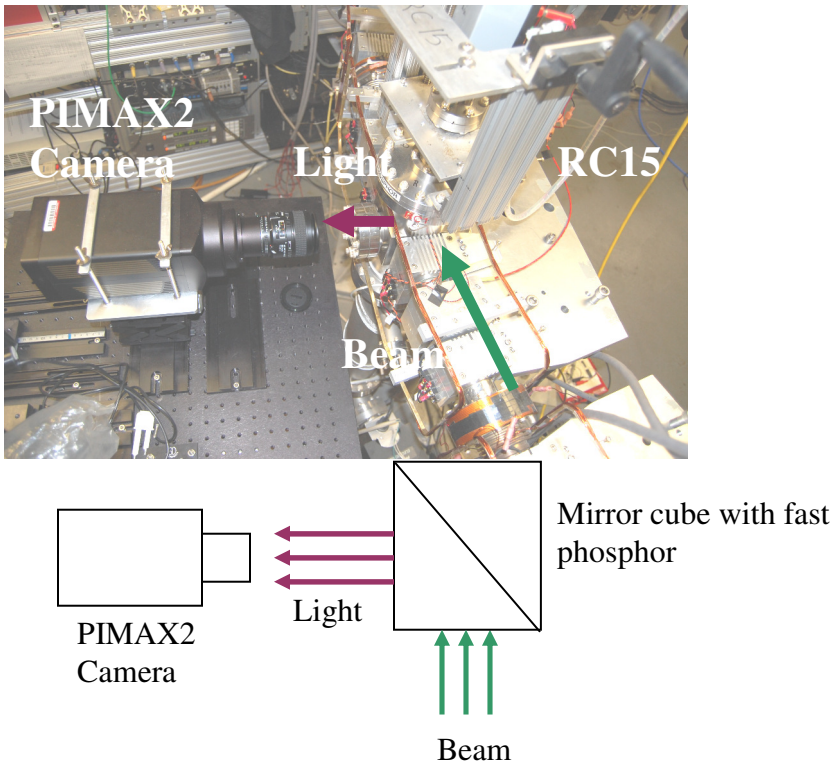

Fig. 4. 3. Fast imaging experimental setup schematic with the 16-bit PIMAX2 ICCD camera installed at RC15.

The 21 mA beam has a head length of 16.0 ns and tail length of 18.0 ns at RC15 (using the BPM in that chamber on the 1st turn). Both lengths are longer than the gate width of the camera.

The 16-bit PIMAX2 ICCD camera is installed at RC15. We integrate each image over 100 beam pulses (frames) to compensate for the low level of light. The camera gate delay is then sequentially shifted by 2 ns per image, such that we image the entire beam along the length of the pulse. Figure 4.4 and 4.5 displays the images

taken from the camera as a function of beam length for the 21 mA beam. The injected pulse length is 101.56 ns.

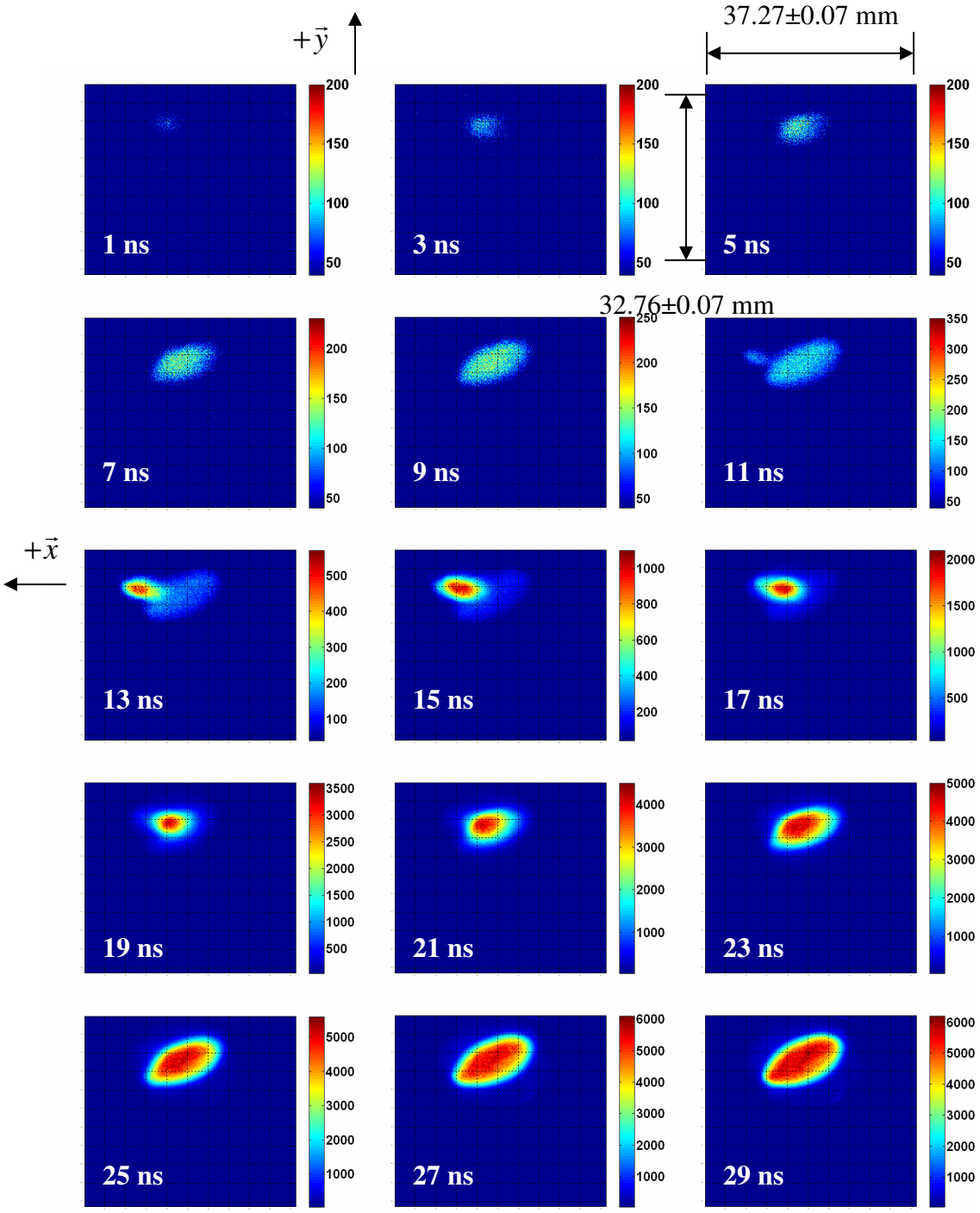

Fig. 4. 4. 3-ns gated camera images of the 21 mA beam **head**, measured at RC15 as a function of time along the beam pulse.

An interesting feature that the beam head exhibits is the recoiling movement of the charge distribution over the consecutive sliced images (shown in Fig. 4.4).

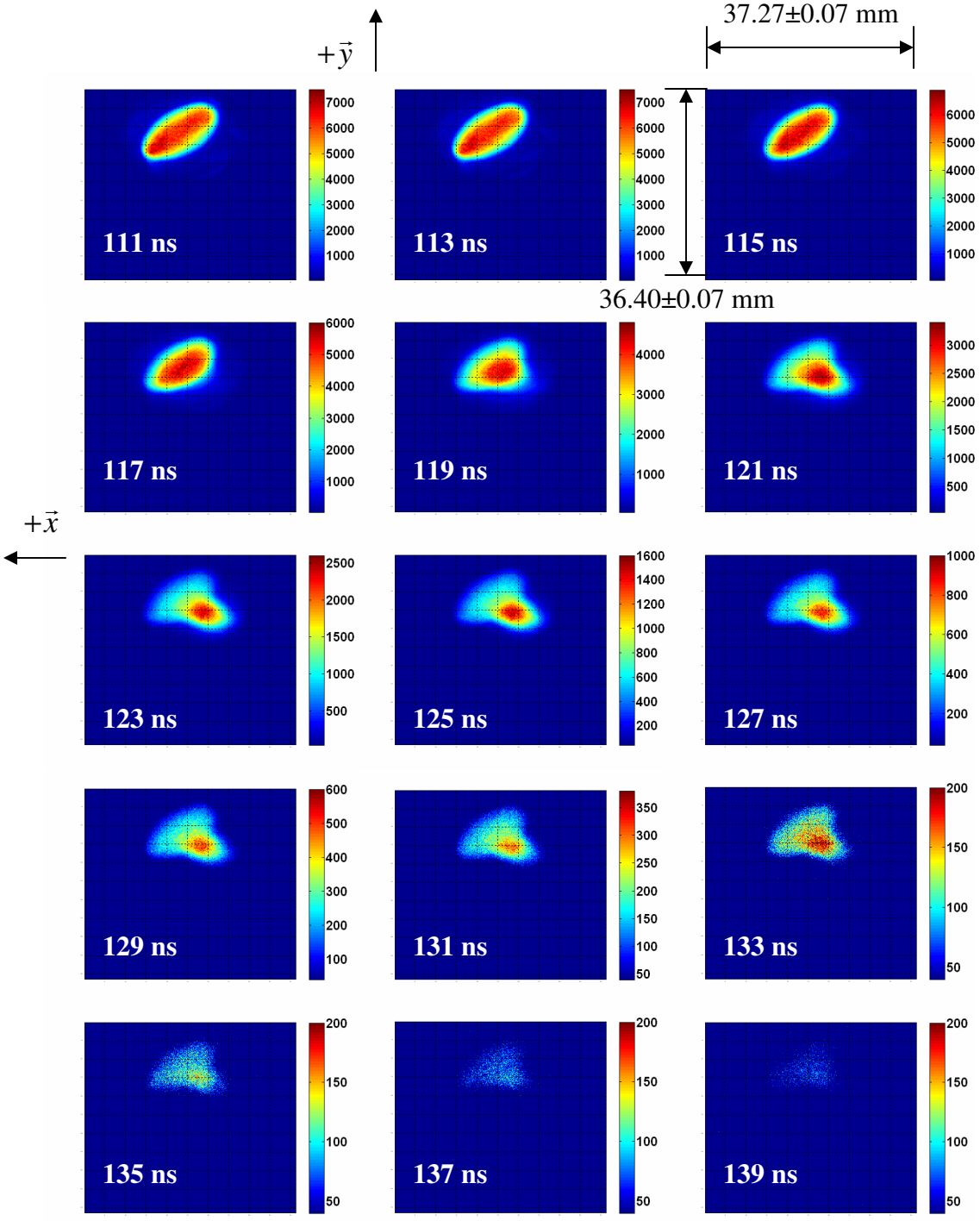

Fig. 4. 5. 3-ns gated camera images of the 21 mA beam **tail**, measured at RC15 as a function of time along the beam pulse.

The beam tail also exhibits a similar movement of the charge distribution over the consecutive sliced images (shown in Fig. 4.5) but not such a large recoiling behavior as with the beam head (shown in Fig. 4.4).

The outermost edge of the bunch head theoretically has particles with energies of $\frac{1}{2}m(\mathrm{v}_o + 2C_s)^2$, where $\frac{1}{2}m\mathrm{v}_o^2$ is the particle energy in the central region of the beam. The theoretical energy at the outermost edge of the bunch tail is $\frac{1}{2}m(\mathrm{v}_o - 2C_s)^2$. The beam images display a centroid shift from the head of the beam to the tail of the bunch. The pictures also appear to display a vertical displacement as well as the horizontal displacement. This is likely due to vertical dispersion as a result of the earth's field.

Beam position, from the images shown in Fig. 4.4 and 4.5 is illustrated in Fig. 4.6. We estimate a calibration of 0.07 mm / pixel from the optical system.

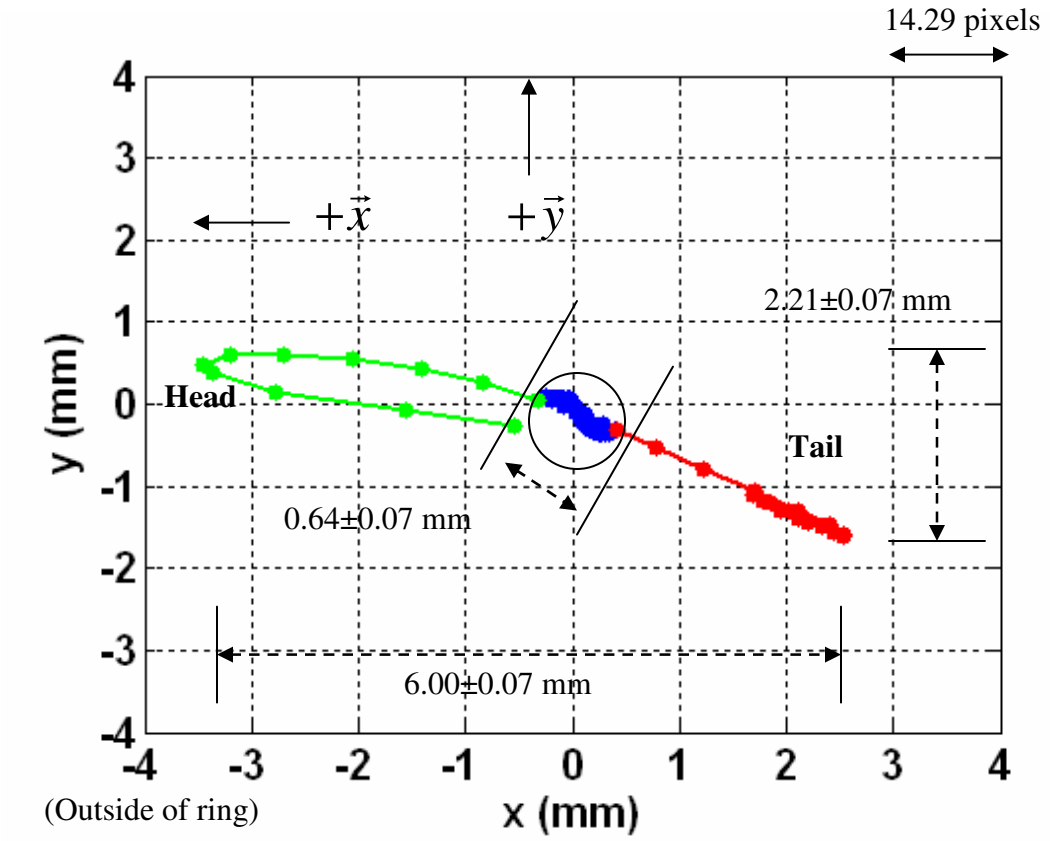

Fig. 4. 6. Centroid measurements from the 3 ns gated camera images of the 21 mA beam, measured as a function of beam length at RC15. We subtract the position where (0, 0) refers to the centroid of the bunch center from all data points. (Calibration was 0.07 mm/pixel)

The overall maximum horizontal and vertical displacement caused by the beam head and tail regions is 6.00±0.07 mm and 2.21±0.07 mm, respectively. The blue region of data (shown in Fig. 4.6) at the origin, is a movement of the bunch center by 0.64±0.07 mm. The green and red regions in Fig. 4.6, corresponds to the bunch head and tail regions.

The head recoiling that was observed in Fig. 4.4 is apparent in the centroid measurement, by the green loop. This recoiling effect appears to be a sampling of the change in the betatron motion from the very edge of the head to the main core of the beam. This is a result of the fact that we are sampling along the beam length while

the measurement position (at RC15) is fixed, from high energy to lower energy (where the central core of the beam is at 10 keV). There was also a loop in the tail (shown in red in Fig. 4.6), but it was substantially smaller then the corresponding green loop for the head.

This measurement is feasible as a result of the system stability. During a period of 1.66 s, 100 integrations are taken per image for each point along the bunch.

In order to correlate the measured centroid motion with particle energy, we independently measure the dispersion function of the transport line from RC1 to RC17. To do this, we systematically change the injected beam energy (by sweeping the high voltage power supply in the gun) and observe the change in transverse position. Using the central region of the bunch at each of the BPMs, we then obtain the dispersion displayed in Fig. 4.7.

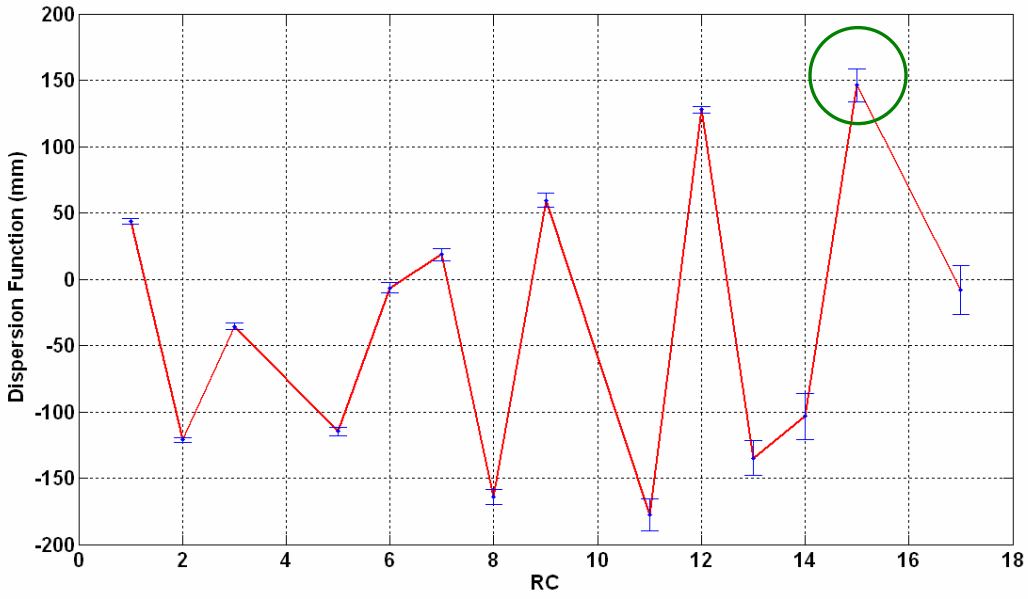

Fig. 4. 7. "Linac" dispersion measured around the ring for the 21 mA beam. This differs from the ring measurement in [76] since we are looking at the 1st turn data as opposed to the equilibrium orbit.

A caveat of using this method of measuring the dispersion is that it is not entirely the same as an end particle accelerating or decelerating from the gun, starting at the injected energy. The bend angle at injection will vary with various beam energies, whereas the particle accelerating from the injected energy will have a constant bend angle. Since calculations show that the 21 mA bunch reaches its peak energy prior to exiting the injection section, this method of measuring dispersion can be used to estimate the centroid dependence on beam energy.

The "linac" dispersion, measured at RC15, was 146.2±12.6 mm. Using Eqn. 3.6 and the measured maximum horizontal displacement for the bunch head region as 3.45±0.07 mm (from Fig. 4.6) up to the point the centroid loops back, the approximate energy deviation measured at RC15 on the 1st turn is 869±111 eV. This assumes that the point which the centroid loops back is not at the peak head energy of $\frac{1}{2}m\left(\mathrm{v}_o + 2C_s\right)^2$ and thus we add the recoil length relative to the maximum centroid deflection. A better method would be to measure the tune along the head and tail regions of the beam and then relate that through the natural chromaticity in order to measure the head and tail energies (This is presented in the Sec. 4.2.2).

The same measurement method is repeated for the tail, obtaining 543±111 eV with a mean of 706±111 eV for both the head and tail. The theoretical bunch-end energy using Eqn. 2.11 in Sec 2.3.1, is 871.3±1.6 eV. The bunch head agrees well with theory but the bunch tail is outside of the error bars of the measurement. This may be a result of the limited aperture of the system as was shown in [76]. An error in the steering solution decreases the transportable aperture, resulting in current loss due to scraping when tail or even head particles are deflected as a result of the energy loss.

4.2.2 Orbit Perturbation for Head and Tail Tune Measurements

The following section presents an experimental measurement that allows us to measure the tune along the bunch using a perturbation technique, from which we estimate the corresponding bunch-end energies.

The two methods that have been used to measure tune of the UMER beam in the past have utilized either many BPMs or many turns of information [55, 76, 77]. Using either of these methods to measure the tune along the bunch length becomes complicated by the bunch-end expansion. If the particles at the ends of the bunch result in a centroid displacement from energy gained and lost, then the correlated tune along the bunch will depend on the location of the beam in the ring (as discussed in Sec. 2.2.1) since the longitudinal energy profile is continually varying as the bunch propagates. By perturbing the 1st turn orbit with a dipole error while keeping the measurement point fixed, we gain the induced phase error from the resulting dipole error [78]. Utilizing this method over a set of dipoles allows us to measure the tune at a fixed location.

The observation point in the experiment was RC15 and the perturbation dipoles were D18 to D29 (the last dipole prior to RC15) a distance of 3.68 m; long enough for the beam to complete at least two betatron oscillations. The current in each dipole was varied from $I_{default} - 0.2$ to $I_{default} + 0.2$, where $I_{default}$ is the default current in the dipole. A line was fitted to obtain the resulting deviation measured at the RC15 BPM

as a function of the perturbation current. The slope is equal to $m = \frac{\Delta x}{\Delta I}$, where Δx is the change in transverse position (not equilibrium orbit) from the default and ΔI is the change in dipole current from the default.

By fitting a sinusoidal function to the slopes as a function of dipoles, one obtains the frequency (tune) of the perturbed centroid motion (as shown in Fig. 4.8).

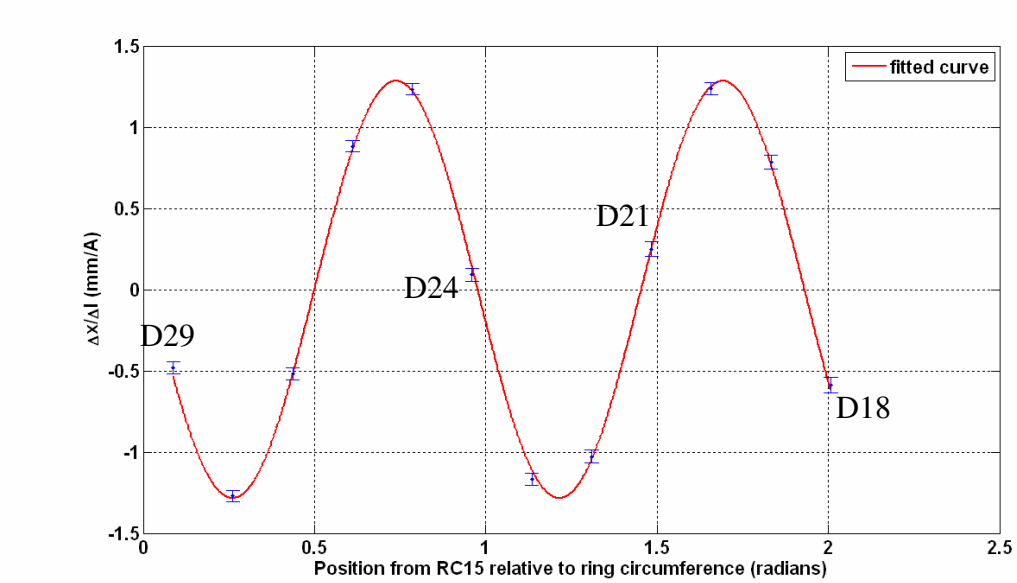

Fig. 4. 8. Measured perturbed **horizontal** centroid motion (within the central region of the beam using a 2 ns window) around the ring using a single beam position monitor (BPM at RC15). The measured tune is 6.49±0.1 with a fit goodness of 0.994. The average error per point is 0.1 mm/A. The quadrupole currents in this experiment are at 1.826 A.

Figure 4.8, displays the perturbed centroid motion as a function of distance (in radians) from the BPM at RC15, relative to the ring circumference. The fitted tune within the middle of the beam, over a 2 ns window, is 6.49±0.1 with a fit goodness of 0.994 and average error per point of 0.1 mm/A. The quadrupole currents for this experiment were set to 1.826 A.

The 2 ns data window is slid along the bunch length and the measurement is repeated, producing the tune along the bunch length (shown in Fig. 4.9) measured at a fixed point within the ring (at BPM RC15).

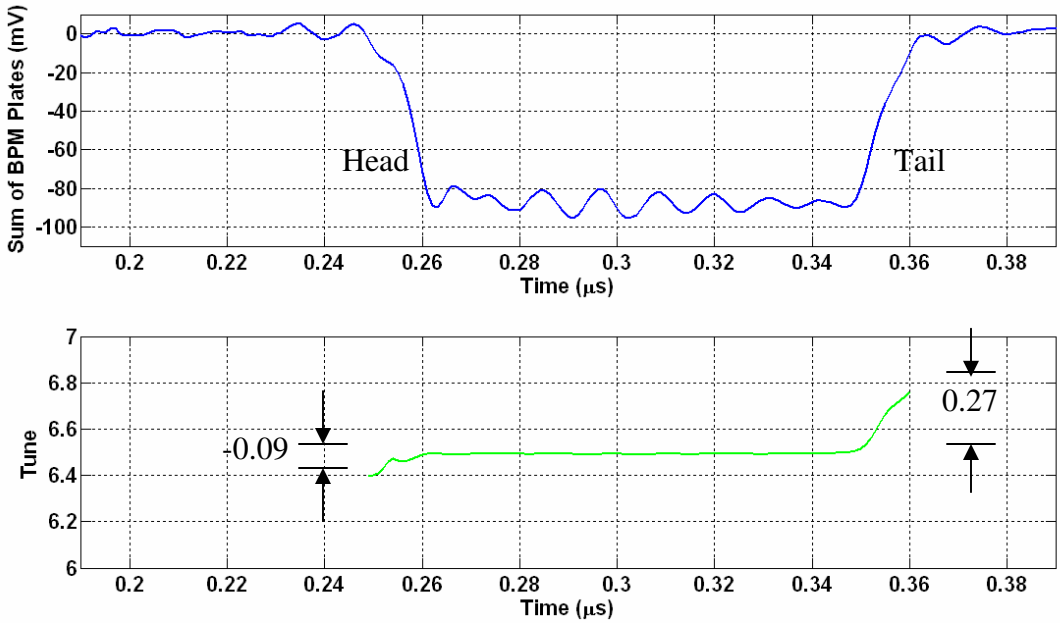

Fig. 4. 9. (a) Sum of all BPM plates at RC15. (b) Horizontal tune as a function of beam length, measured using a single beam position monitor (BPM) at RC15 and dipole scans.

The minimum measurable head tune (shown in Fig. 4.9) using this technique is 6.40±0.1, and the maximum tail tune is 6.76±0.1. The tune shift due to the head of the beam is -0.09 and that due to the bunch tail is 0.27. The tune shift at the head of the bunch is also less then the error bars of the measurement.

The central region of the beam is fairly close to the half-integer tune; whereas the tail of the beam is 0.24 from the integer tune of 7 and the head of the bunch is 0.4 from the integer tune of 6. The tail of the bunch is closer to the integer tune and has more potential to be affected by a resonance during multi-turn operation as opposed to the bunch head. Since this is a 1st turn measurement, where resonant effects

require many turns to develop, the different tune shifts at the bunch head and tail could be a result of misalignments (errors in the steering solution). If the equilibrium orbit is greater than the radius of the machine, particles at the head will interact with the beam pipe sooner than particles at the tail, leading to scraping of the head. This could be the cause of the non symmetric tune shifts at the head and tail. Comparing these numbers with theory, we expect an energy gain at the bunch head/tail of 871.3±1.6 eV, which corresponds to a tune shift of -0.309/0.358, using Eqns. 2.13 and 2.14 in Sec. 2.3.3. The measured tune shift induced at the bunch tail (0.27) is significantly closer to the analytical values than the induced tune shift by the head of the beam.

4.2.3 Head and Tail Harmonic Components

The next method for measuring head and tail energies relies on the fact that (for a non-relativistic beam), particles with higher energies than the injected energy will require less time to complete one lap as opposed to particles with lower energies.

Using an FFT analysis of the bunch current profile, we have obtained multiple harmonics of the bunch where a few correspond to the bunch-ends of the beam. Because the injected bunch in UMER is rectangular, the current measurement will exhibit most of the signal power within all odd harmonics of the main revolution frequency [79]. Using Eqns. 4.2, we are able to obtain the Fourier series coefficients a_0, a_n, b_n of a periodic signal $x(t)$ (Eqn. 4.1),

$$x(t) = a_0 + \sum_{n=1}^{\infty} a_n \cos(\omega_o t n) - \sum_{n=1}^{\infty} b_n \sin(\omega_o t n) \qquad \text{(Eqn. 4. 1)}$$

$$a_0 = \frac{1}{T}\int_{-T/2}^{T/2} x(t)dt\,,\; a_n = \frac{2}{T}\int_{-T/2}^{T/2} x(t)\cos(\frac{2\pi tn}{T})dt\,,\; b_n = \frac{-2}{T}\int_{-T/2}^{T/2} x(t)\sin(\frac{2\pi tn}{T})dt \quad \text{(Eqn. 4. 2)}$$

where T is the period of the signal and n is the harmonic multiplier. An example of a rectangular current profile, as would be initially injected into UMER, is shown in Fig. 4.10a for one period. The periodic pulse train begins at $t = 0$ and has a period of T.

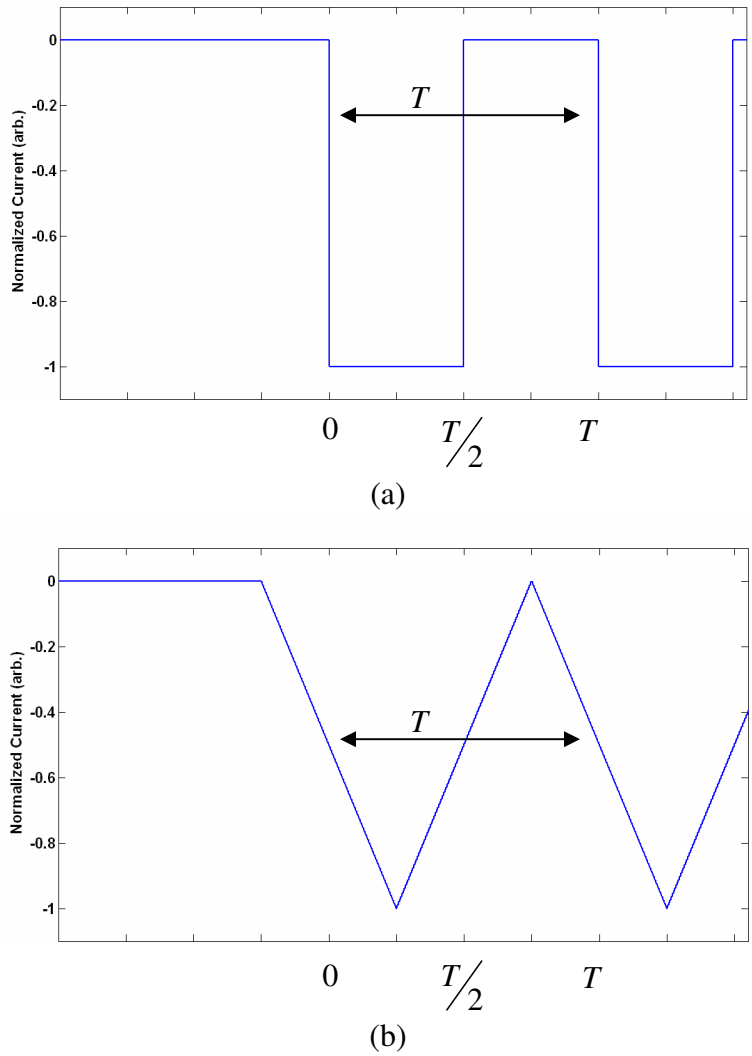

Fig. 4. 10. Top plot (a) displays an example injected rectangular current profile where as the bottom plot (b) displays an example triangular current profile.

Computing the Fourier series coefficients of an initial rectangular current profile (shown in Fig. 4.10a), we obtain $a_0 = -\frac{1}{2}, a_n = -\frac{\sin(\pi n)}{\pi n}, b_n = \frac{1-\cos(\pi n)}{\pi n}$. Evaluating this expression for all $n \neq 0$, results in $a_n = 0, b_1 = \frac{2}{\pi}, b_2 = 0, b_3 = \frac{2}{3\pi}, b_4 = 0, \ldots$; where the non-zero multiples of the revolution frequency are the odd multiples of n. Since the bunch is also expanding as a result of the longitudinal expansion, the current profile becomes more triangular and/or trapezoidal in shape and less rectangular (as shown in Fig. 4.1 and 4.2). If we compute the Fourier series coefficients of a triangular current profile (shown in Fig. 4.10b), only the odd multiplies of the revolution frequency are present but at a reduced amplitude from the coefficients of a rectangular profile. The coefficients are $a_n = 0, b_1 = -\frac{4}{\pi^2}, b_2 = 0, b_3 = \frac{4}{9\pi^2}, b_4 = 0, \ldots$. Since there are only odd harmonic multiples, even multiples will have no signal power from the main revolution frequency. Similar to a saw tooth or trapezoidal waveform, the bunch-end expansion excites both odd and even harmonics. By observing the even harmonic multiples of the revolution frequency, we are able to resolve both head and tail frequency peaks that are otherwise not clear in the odd multiples.

Fast Fourier Transform (FFT) measurements of the wall-current monitor (at RC10) are shown below (in Fig. 4.11a), up to the seventh harmonic. The FFT was computed within the oscilloscope using the function, FFT Spectral Magnitude on the Tektronix DPO7154. The measurement was repeated for three different beam currents; 0.6 mA, 6 mA and 21 mA. Baseline compensation is not needed in this measurement since the frequency content of the signal is much faster than the changing baseline.

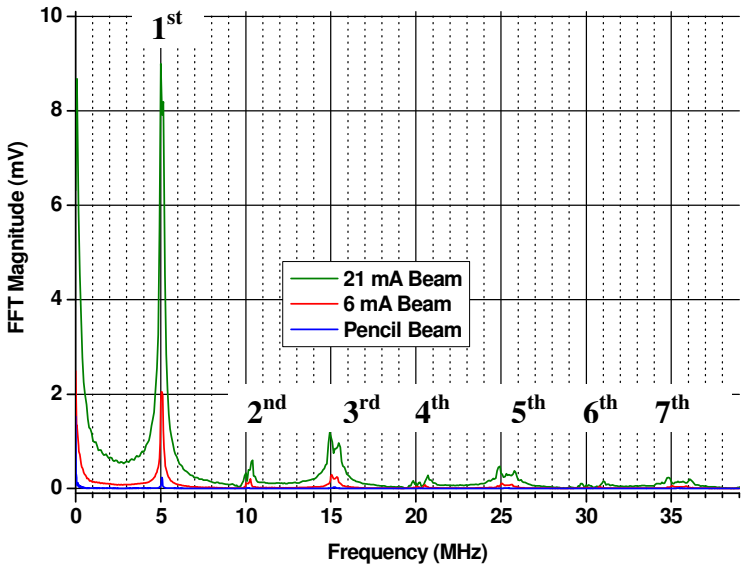

(a)

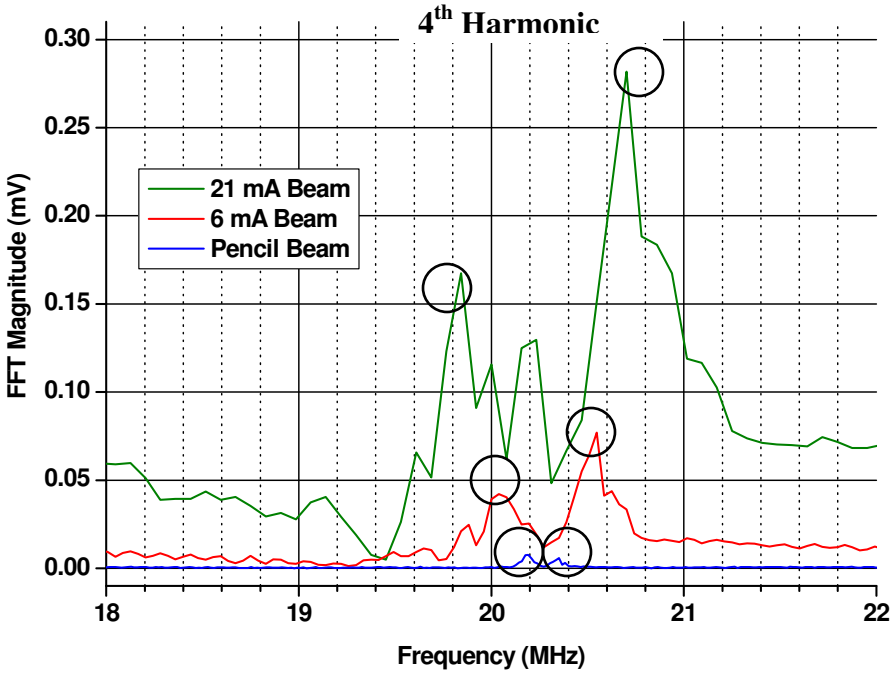

(b)

Fig. 4. 11. FFT Comparison of experimental measurements at the RC10 wall-current monitor for three different injected beam currents; 0.6 mA, 6 mA and 21 mA. Top plot (a) displays seven harmonics whereas the bottom plot (b) displays a close-up of the 4th harmonic.

The fourth harmonic (shown in Fig. 4.11b), clearly displays a head and tail component of the revolution frequency that is otherwise not clear in the 1st harmonic.

The frequency span is from 18 MHz to 22 MHz. By utilizing the higher order even harmonics to measure bunch-end frequencies, we force a wider separation between the peaks, so that the separation is greater than the error bars associated with the measurement. Table 4.1, displays the measured side peaks from Fig. 4.11b.

Table 4. 1. Measured side peaks at the 4th harmonic resulting from the bunch-ends as well as calculated energies using Eqns. 2.13 and 2.14 in Sec. 2.3.3.

Beam Current (mA)	**Head Frequency (MHz)**	**Head energy (eV)**	**Tail Frequency (MHz)**	**Tail energy (eV)**
0.6	20.352±0.016	+89±1	20.184±0.016	-81±1
6.0	20.547±0.039	+288±59	20.039±0.039	-227±59
21.0	20.720±0.078	+467±60	19.840±0.078	-425±60

As the beam current increases, the separation between the peaks also increases in frequency space. This is a result of the longitudinal expansion (the energy gained and lost at the ends) scaling with injected beam current through the sound speed C_s. Using the head and tail frequencies at the 4th harmonic, we estimate the energy gained at the bunch-ends using the default energy for UMER (specified in Table 3.3 in Sec. 3.4.1). This is calculated using Eqns. 2.13 and 2.14 in Sec. 2.3.3 and dividing the frequencies by 4. The calculated energies are shown in Table 4.1.

One complication with this measurement is that it does not resolve the peak head or peak tail energy, at the extreme edges of the beam. It also averages over many turns and thus if the head and tail dynamics are changing over the measurement window, with either beam size or current, then the measured energy will also change. This FFT method was repeated on the WARP simulation (where no current loss or change beam size is incurred) data presented in Fig. 4.2 of Sec. 4.1.2, obtaining similar results. The method resolves overall a lower head and tail energy then the actual

value obtain from phase-space plots or that calculated via the analytical formula based on the sound speed C_s. It appears as if the method resolves the head and tail centroid energy, which is not the peak bunch head energy of $\frac{1}{2}m\left(\mathrm{v}_o + 2C_s\right)^2$ or the peak tail energy of $\frac{1}{2}m\left(\mathrm{v}_o - 2C_s\right)^2$.

4.3 Summary and Comparison of Different Measurements

To conclude this chapter, we compare the measured bunch-end energies and tunes from the resulting longitudinal expansion as a result of space-charge for three different beam currents; 0.6 mA, 6 mA and 21 mA. We will compare the three experimental methods in Sec. 4.2.1-4.2.3 with each other as well as with analytical calculations from the 1-D cold fluid theory and WARP simulations. Figure 4.12 displays the peak bunch-end energy measurements, calculations, simulations described in this chapter.

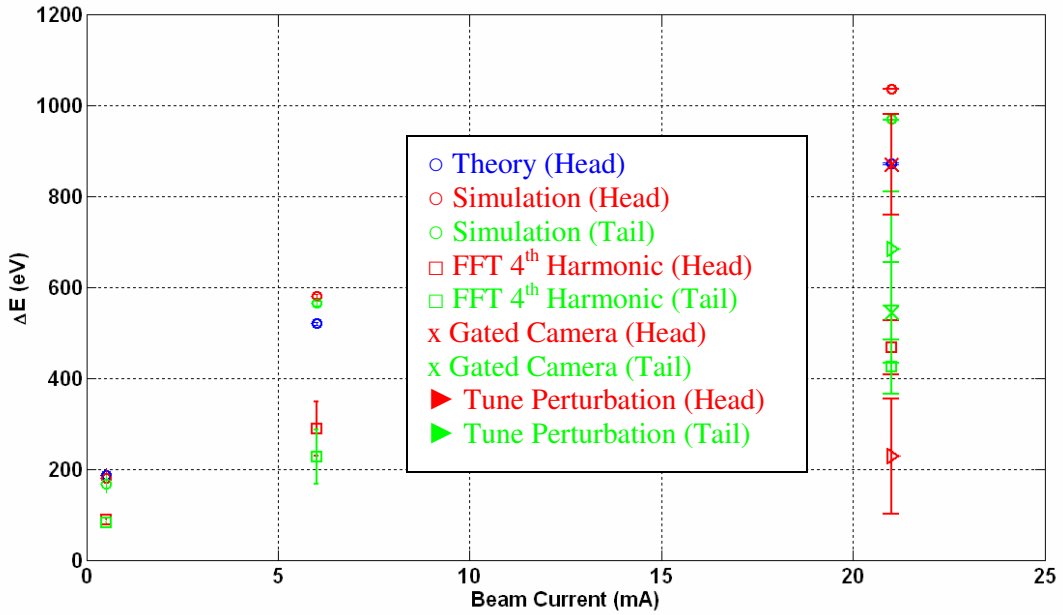

Fig. 4. 12. Calculated, simulated and measured (using the three experimental methods described in this chapter) maximum bunch-end energies for the three injected beam currents (0.6 mA, 6 mA and 21 mA).

The orbit perturbation tune measurement in Sec. 4.2.2 was converted to energy using the natural chromaticity of the lattice, $n = -7.9$ [76]. The data is shown in Fig. 4.12 as red and green triangles.

The some of experimental measurement methods agree with each well within the error bars whereas some do not. The gated camera measurement for the 21 mA beam agrees well with theory and simulation, within the error bars for the bunch head peak energy. The same is not so true for the bunch tail peak energy; the value measured is outside of the error bars. The tune perturbation method is also low for both the head and tail peak energies when compared with the simulation and theoretical values. This may be a result of current loss as a result of scraping during the measurement, especially if the beam is too close to the beam pipe from miss steering. The FFT measurements are low for all three beam currents measured when compared with

simulation and theory, which may be a result of the method and its ability to resolve only the bunch head and tail centroid energy and not the peak energies at the extreme edges of the beam.

The tune is correlated to beam energy as well as the bunch-end energy. Figure 4.13 displays the induced tune shifts for the three beam currents.

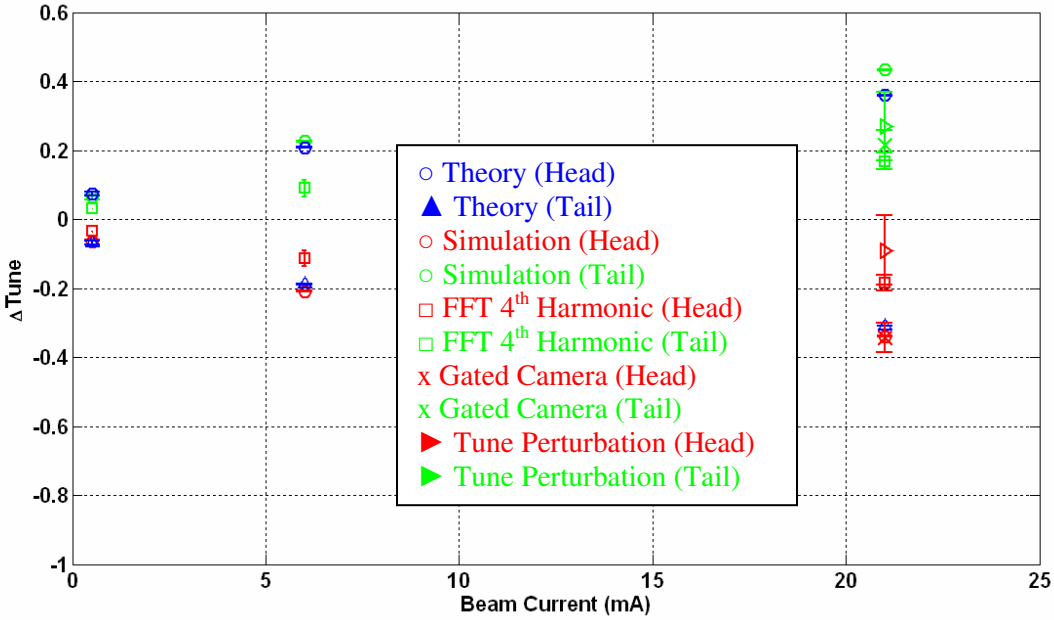

Fig. 4. 13. Calculated, simulated and measured (using the three experimental methods described in this chapter) induced tune shifts for the three injected beam currents (0.6 mA, 6 mA and 21 mA).

As the injected beam current increases, the bunch-end energy increases and thus the tune shift (at the edge of the beam) becomes larger (as shown in Fig. 4.13).

Similarly with the data presented in Fig. 4.12, simulation results and analytical calculations agree fairly well within error bars of the gated camera measurement for the 21 mA bunch head. The tune shift at the tail falls outside of the error bars, for the same measurement. The tune perturbation technique for the 21 mA bunch tail agrees with theory, within the error bars of the measurement, but the technique disagrees for

the bunch head. With both of these measurements, only (head or tail) agrees within the error bars and the other is outside of the error bars. The value is low and may likely be a result of scraping as described earlier. The gated camera measurement doesn't perturb the beam orbit, but the tune perturbation does and that may be the reason why the agreement flips from the head to tail for both measurements. Once again as with the previous figure, FFT measurements estimate a lower tune and this is likely a result that the method does not resolve the peak head and tail energy but the head and tail centroid energy.

These discrepancies will hopefully be understood once an energy analyzer is installed in the ring and/or other experimental methods are implemented for both first turn and eventual multi-turn studies to approximate the peak head and tail energies.

Chapter 5: Longitudinal Confinement

Having examined the bunch-end current/energy profiles due to space-charge, we now present an experimental investigation of longitudinal confinement. The purpose of this chapter is to analyze the trade-offs between focusing frequency and gradients at long-path lengths in order to find one of the many optimal focusing solutions to contain the bunch. Through various experimental measurements, we are able to understand the beam dynamics, with optimized as well as non-optimized focusing parameters.

5.1 Initial Matching

Before any longitudinal focusing is applied to the bunch-ends, we need to measure the end lengths in order to match them to the applied fixed width focusing fields. In this scenario, we are allowing the bunch-end to lengthen until it is equal to the focusing field length.

A comparison between measurements, analytical calculations and simulations of the bunch lengths per turn allows us to extrapolate the expansion rates. All measurements in this chapter are done using the 0.6 mA beam.

5.1.1 Beam Expansion without Longitudinal Containment

As the bunch reaches the focusing gap inside the induction cell, the bunch head and tail profiles will have finite lengths arising from the longitudinal spreading explained

in Sec. 2.2.1 and Ch 4. The application of the initial focusing pulse should be timed so that the beam head and tail durations are matched to the applied focusing fields (which are a fixed value in the current circuitry). This is necessary to avoid a scenario where the initial focusing fields are applied to bunch-ends that have expanded beyond the length of the focusing fields, resulting in electrons outside the containment fields.

For consistency, we define the head/tail duration as the rise time (10% to 90%) of the peak bunch current measured at RC10. The analytical (shown in Fig. 4.1a in Sec. 4.1.1) and simulated (shown in Fig. 4.2a in Sec. 4.1.2) values are measured using the same approach. The lengthening of the overall bunch is also quantified by defining the beam length as the duration between the rise time (10%) points at the head and tail. Results are displayed in Fig. 5.1 below.

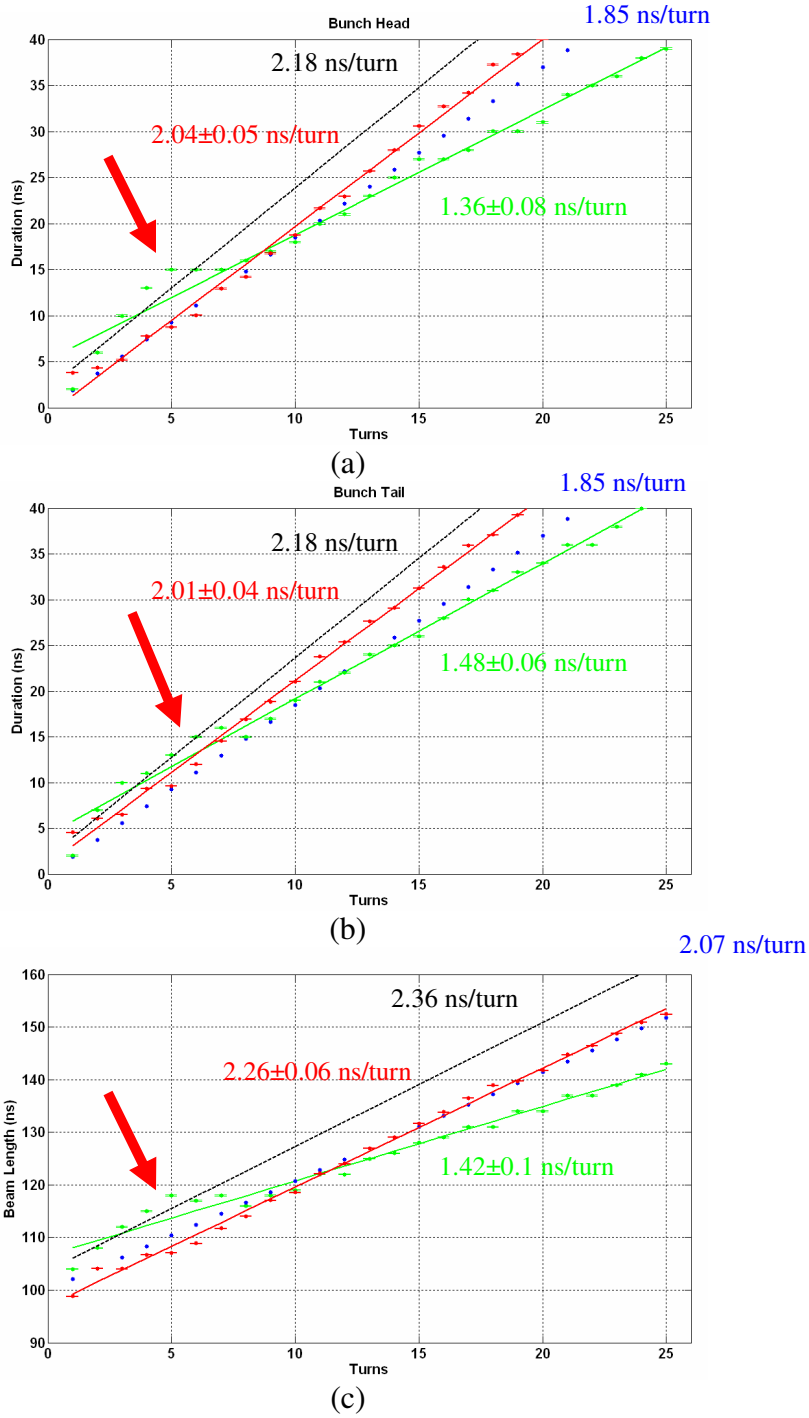

Fig. 5. 1. Bunch-end durations ((a) head, (b) tail) as well as (c) bunch length measured at RC10 for an injected beam current of 0.6 mA and beam length of 100 ns. Linear fits are displayed on each figure. Analytical calculations (blue), WARP simulated (red) results and measurements (green) are displayed for the same beam parameters. Large red arrows point out the kink in the measured data. Black dashed line is a fit to the first seven measured data points.

Figures 5.1a-b, displays the bunch-end durations measured at successive turns with the RC10 wall current monitor when no confinement fields are applied and Fig. 5.1c displays the beam length over the same turns. The expansion rates for the measured data, WARP simulation and analytical calculations are shown in green, red and blue, respectively. The sum of both bunch-end (analytically calculated and simulated) growth rates is larger than the incremental increase in beam length, as a result of the beam rarefaction wave propagating into the beam at a C_s (explained in Section 2.2.1).

A comparison between the three measured data sets shows a decrease in the experimental expansion rate, occurring at approximately turns 5-7 (pointed out by the large red arrows). This is true for both the bunch-ends expansion rates as well as the beam length. Waveform profile comparisons (in Sec. 4.1 in Fig. 4.1 and 4.2) do not show any significant current loss for the 0.6 mA beam as with the other beams until the 10^{th} turn. A potential cause of the varying erosion rate may be due to a change in the beam radius.

If we fit a line to the first seven measured data points in all three cases (shown in black), we obtain erosion rates that are within 4-8% of the WARP simulations linear fits. The erosion rates for both the head and tail are 2.18 ns/turn and the bunch length rate is 2.36 ns/turn. In all three cases, the seven point fits are significantly closer than the fits that include all the data. This shows that the erosion rate discrepancy occurs during beam propagation within the lattice.

If we assume the beam sized increased by a factor of 3 on the 7^{th} turn, as a result of an emittance growth from mismatch at the Y-section, it would cause the rates to

decrease by 20% (calculated using theory presented in Ch. 2). Using the analytical erosion rate, 1.85 ns/turn (on Fig. 5.1a-b), we obtain 1.48 ns/turn resulting in at most an 8% disagreement between theory and measured values, yielding better agreement.

Assuming that the erosion rate remains constant as the beam propagates over many turns is incorrect. Since the beam is continually evolving and is subject to many errors, such as mismatch and miss-steering resulting in scraping, this will lead to an erosion rate that is changing from turn to turn.

5.1.2 Application of Focusing Fields

This section presents the voltage profile that is periodically applied to the bunch-ends using the induction cell.

The durations are important as they are used to determine the point of initial application and to verify erosion rates from calculations. Since we must match the bunch-ends to the focusing fields, there must be knowledge of the fixed length focusing fields.

The negative head focusing field rise time (10% to 90%) is 10.1 ns and the positive tail focusing field is 5.4 ns. The peak field is adjustable via the power supply charge voltage, which changes the focusing gradient over the fixed durations seen by the beam [62, 83]. Figure 5.2 displays an example induction cell voltage versus time for one application of focusing at an arbitrary power supply charge voltage.

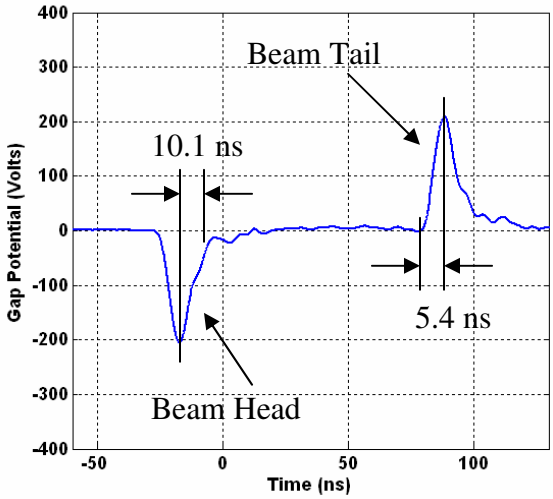

Fig. 5. 2. Induction cell voltage versus time (at an arbitrary focusing voltage).

The voltage profile shown in Fig. 5.2, displays a peak focusing field of 200 eV. During multiple applications of focusing, subsequent fields are applied at a frequency that is synchronous with the revolution frequency of the bunch. This occurs since the beam propagates through the induction cell every turn. Throughout the rest of this document we will refer to the focusing frequency as a multiple of the revolution period. For example, if the focusing fields are applied every 10 turns, then there are 10 revolution periods (or 1.9739E-6 μs) between every application of focusing or $\frac{T_{focus}}{T_{rev}} = 10$. Where, T_{focus} is the period of the focusing frequency and T_{rev} is the period of the revolution frequency.

The erosion rates presented in the previous section are also used to estimate the rate of increase or decrease from chambers RC4 to RC10. From Fig. 5.1, the bunch head expansion rate is 1.36±0.08 ns/turn and tail expansion rate is 1.48±0.06 ns/turn. Since the distance from RC4 to RC10 is 1/3 the ring circumference, the beam head

will expand between those to chambers by 0.45±0.03 ns/turn. Similarly for the tail, we obtain 0.49±0.02 ns/turn.

For the initial application, I selected the turn in which the length of the beam end is closest to the length of the corresponding focusing field. The initial 10.1 ns head focusing field is applied at the 3rd turn where the head duration is 9.58 ns (as shown in Fig. 5.1a) at RC4. The initial 5.4 ns tail focusing field is applied on the 2nd turn where the tail duration is 6.54 ns (as shown in Fig. 5.1b) at RC4. Because we only have one induction cell currently operating, this limits our ability to fine-tune the focusing.

This full length matching is not necessary, since the real importance is in the match of the focusing gradient to the axial field gradient of the beam. The fields may be longer then the axial fields of the beam, but as long as the fields are appropriately timed around the bunch, focusing of the bunch will still occur.

5.2 Long Path-Length Confinement

Since we are uncertain as to the correct axial field gradient that is necessary to keep the bunch contained on a periodic basis, this section will present experimental results that investigate the bunch dynamics through observation of the long-path length (gross) effects.

In this section, we present the use of periodically applied longitudinal focusing fields to confine the bunch, in order to observe the long term evolution and behavior of the bunch to the longitudinal confinement. We present a correlation between the

bunch-end dynamics, focusing parameters and the impact on the charge contained. We also demonstrate that with the proper choice of parameters, we can confine the bulk of the beam for greater than 1000 turns, limited only by the charging power supplies in the main UMER system.

5.2.1 Dependence of Bunch Length on Focusing Parameters

Once the initial focusing pulse is applied, the subsequent pulses will periodically confine the bunch from turn to turn. Figure 5.3a-b, displays the beam current without confinement as well as with confinement at a set of optimized focusing parameters (to be discussed later in this section). One of the difficulties with maintaining a constant bunch length with minimal distortion to the bunch is in obtaining a focusing period that is a multiple of the revolution frequency.

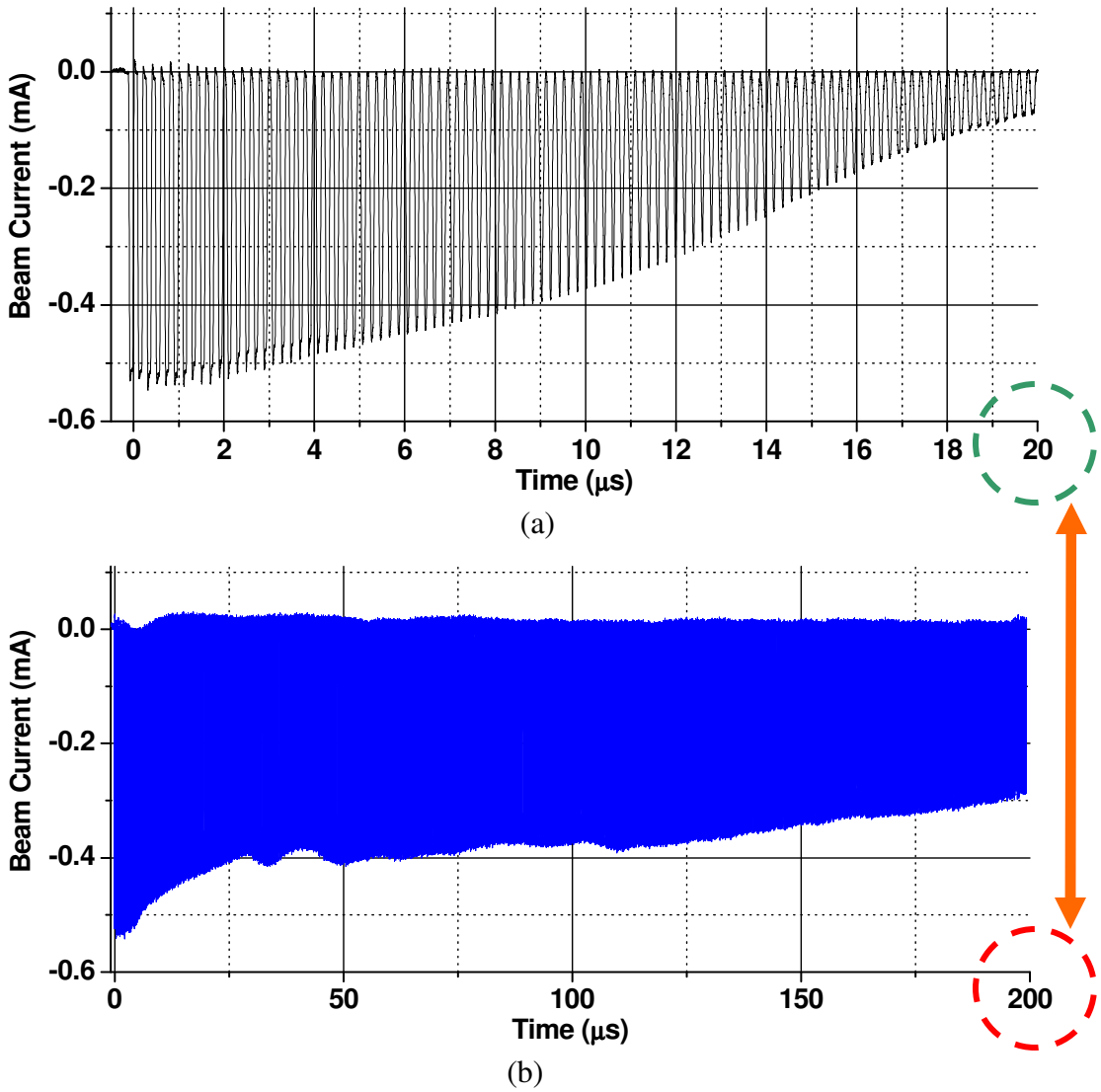

Fig. 5. 3. Beam current measured at the RC10 wall current monitor, (a) without focusing and (b) with focusing. With confinement, the bunch propagation is extended by a factor of ten.

The periodic focusing fields (Fig. 5.3b) allow the bunch to propagate for at least 200 μs or 1000 turns, a factor of ten greater than the unconfined beam (Fig. 5.3a). Since we do not currently have the ability to modulate the focusing field amplitude or focusing period from pulse to pulse, we allow the beam to match itself to the fixed-amplitude and fixed-period containment fields. Implementing a modulation of the

focusing period would be trivial using the programmable arbitrary function generator discussed in the appendix A2.

In the following experiments, we vary the focusing amplitudes and periods over a broad range where both the head and tail fields are equal in amplitude. This means that the gradients are different, as a result of the different rise times, but both fields were independently matched to the beam.

Figure 5.4 displays the evolution of the beam length, for over a thousand turns at various values of the applied focusing amplitudes. The frequency is fixed at 6 periods per application. The total beam length is measured in the same method as in Sec. 5.1.1.

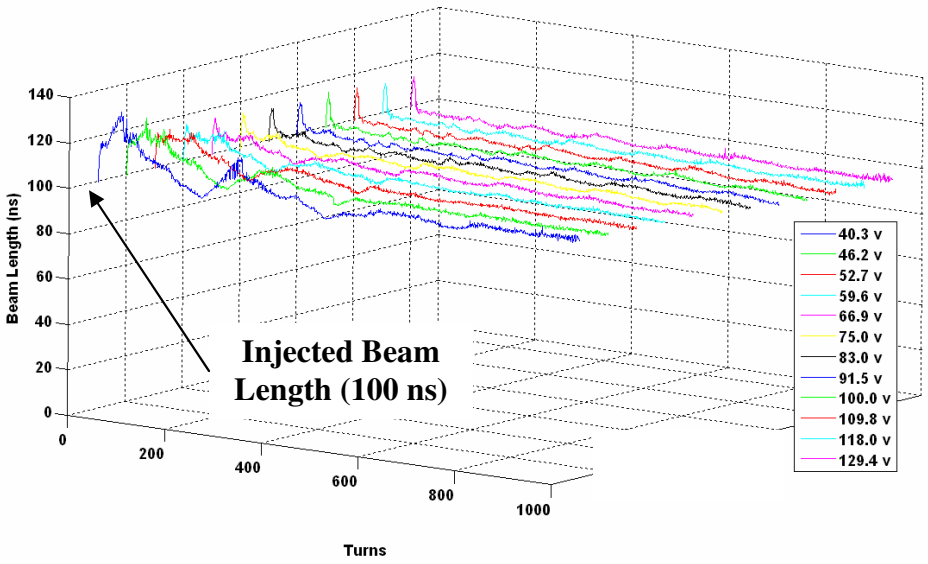

Fig. 5. 4. Total bunch length in ns, measured at the RC10 wall current monitor for various focusing amplitudes. The focusing frequency is fixed at one application every 6 periods. The injected beam length is 100 ns.

There is a strong correlation between the transients in beam length and the focusing amplitude. As the focusing amplitude increases, over the ranges indicated in the legend (shown in Fig. 5.4), the transients in bunch length dampen sooner. The beam

length also settles down to a constant length despite the periodically applied fields. Note that the plotted beam length does not account for differences in current loss, such that total charge is not conserved amongst the traces.

The next experiment was to vary both the focusing period and amplitude. In each case, the average beam length and ripple amplitude are calculated over a thousand turns (shown in Fig. 5.5).

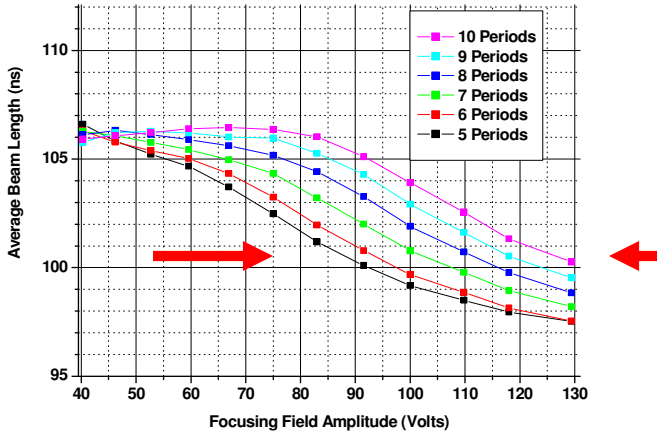

(a)

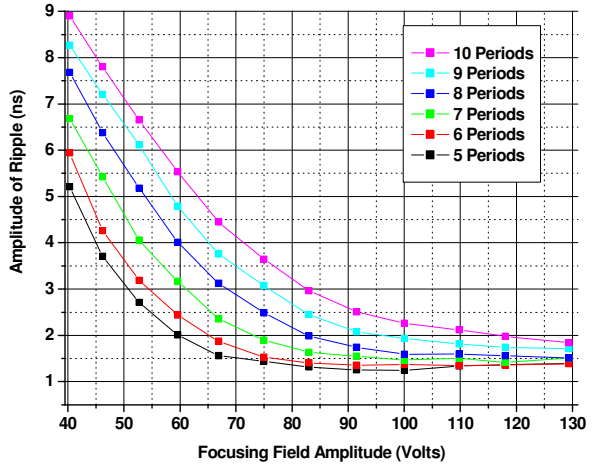

(b)

Fig. 5. 5. Average beam length and ripple for various focusing amplitude at six different periods, calculated over a thousand turns. The plotted beam length and standard deviation does not account for current loss.

Figure 5.5a-b, displays the average beam length and ripple for each focusing period and amplitude. As the focusing period increases, the peak amplitude required to maintain a constant bunch length and ripple must increase. The average force imparted onto the bunch-ends remains constant as long as the focusing period and amplitude are adjusted accordingly. Alternatively, if the focusing amplitude is fixed, than the average bunch length must increase if the focusing period increases.

The focusing amplitude scales linearly with focusing period if the bunch length is to remain constant. Figure 5.6, is a plot of focusing amplitude versus focusing period at a constant average beam length of 101 ns (from data in Fig. 5.5a).

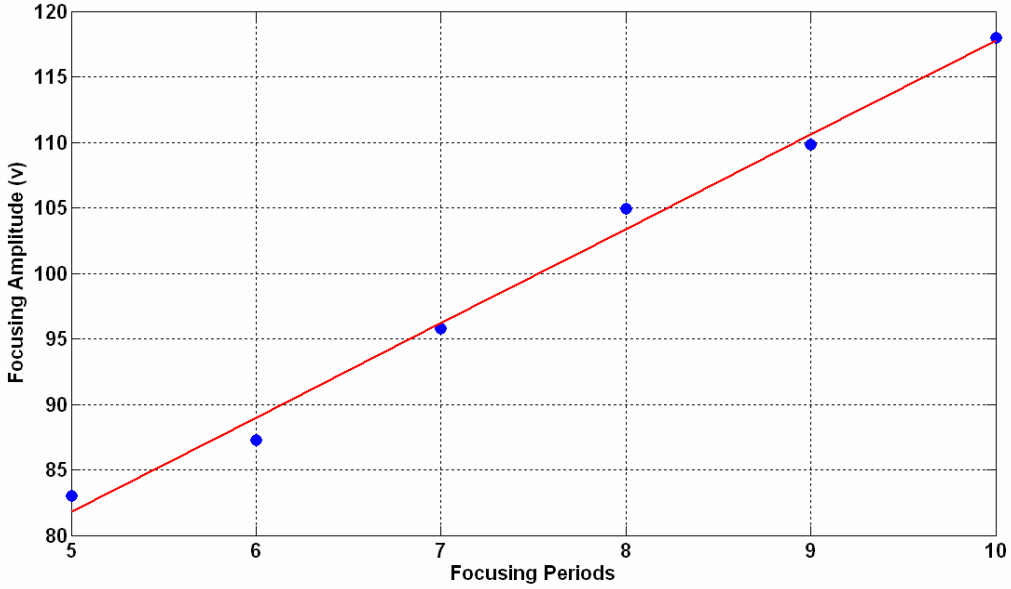

Fig. 5. 6. Focusing amplitude versus focusing period at a constant average beam length of 101 ns.

Figure 5.6, shows that the absolute amplitude and period does not matter as long as the linear relationship is maintained, as you would expect.

So if the bunch could be confined every turn, then the amplitude required to maintain the bunch length at 101 ns would be approximately 53 volts (using this curve). This is substantially smaller than 118 volts required when focusing is applied at a period of 10.

5.2.2 Sensitivity to Timing Errors

This section presents experimental measurements on the beam sensitivity to timing errors. By using the confinement system to keep the beam bunched for over 1000 turns, we can study the resulting timing sensitivity over that time scale. Both head and tail focusing fields are independently controlled, which enables us to vary one while keeping the other constant. The following two figures display the beam current measured at the RC10 wall current monitor. The red arrow points to the 1011^{th} turn in each case.

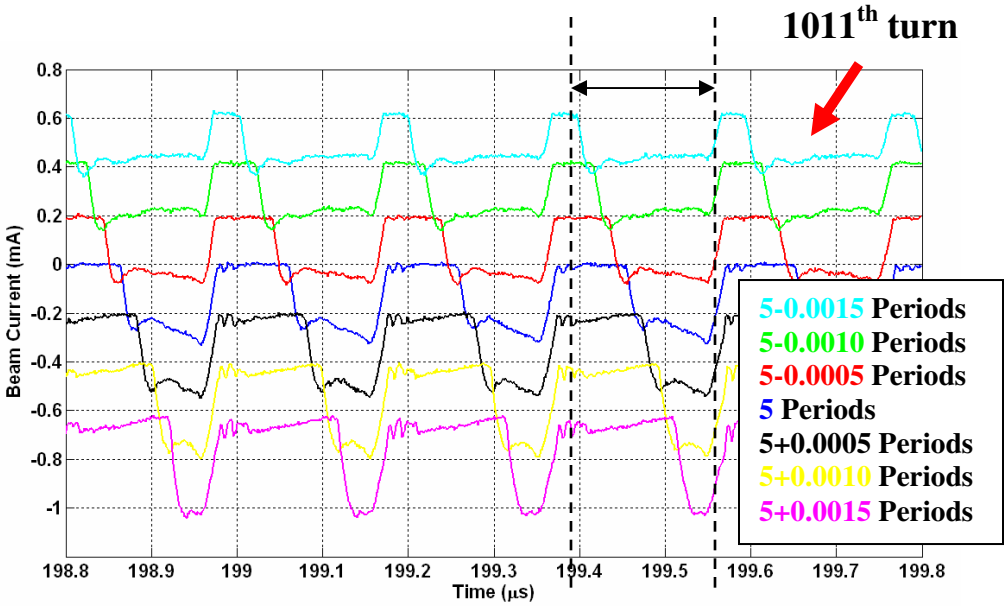

Fig. 5. 7. Beam current measured at the RC10 wall current monitor with the varied *head* focusing field and fixed *tail* field. The nominal focusing period of 5 is displayed in blue while the varied ones (in other colors) are shifted by ±0.2 mA for every ±0.0005 periods from 5. Red arrow highlights the 1011th turn.

Figure 5.7 displays the beam current at a focusing period of 5 in blue as well as the variations about that. The head focusing field is varied in steps of ±0.0005 periods and shifted by ±0.2 mA for each step. The same is repeated for the tail focusing field, by keeping the head field fixed (as shown in Fig. 5.8).

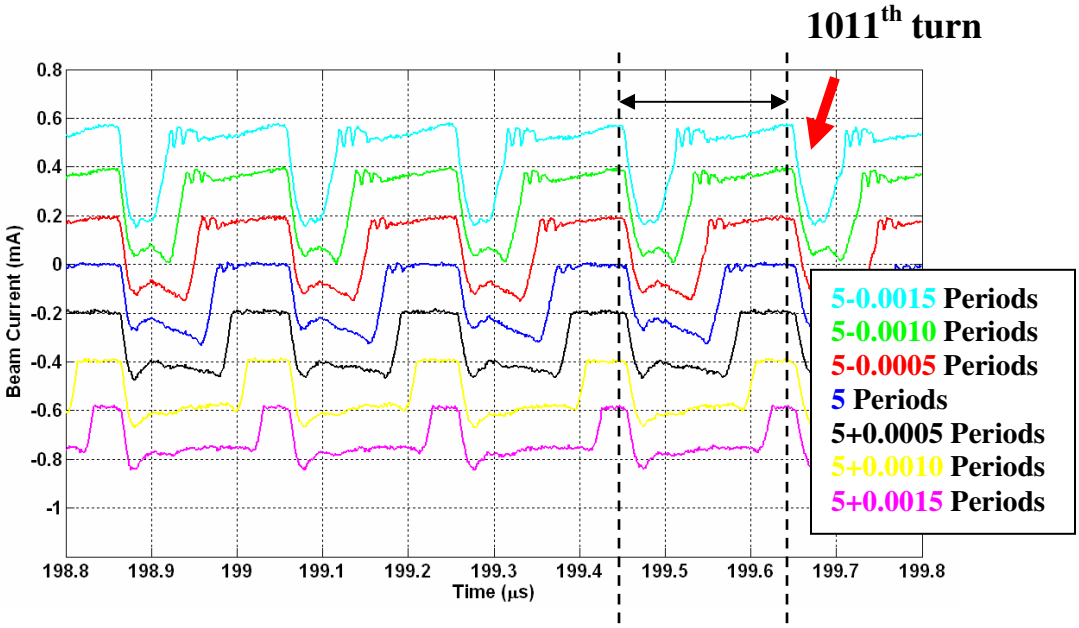

Fig. 5. 8. Beam current measured at the RC10 wall current monitor with the varied *tail* focusing field and fixed *head* field. The nominal focusing period of 5 is displayed in blue while the varied ones (in other colors) are shifted by ±0.2 mA for every ±0.0005 periods from 5. Red arrow highlights the 1011th turn.

As the fields are adjusted about the integer focusing period, the beam responds by increasing and decreasing in length. For every 0.0005 increase in the period, the bunch length changes by approximately 20 ns at the 1011th turn. This is true for both the variation of the head focusing (shown in Fig. 5.7) as well as the variation of the tail focusing (shown in Fig. 5.8). In order to obtain a 20 ns error at the 1011th turn, the initial application of focusing must be off by (20 ns ÷ 1011 turns) = 19.8 ps. This means that if one of the focusing periods is off by 19.8 ps, the beam length at the 1011th turn will result in a 20 ns increase or decrease in length. If we want to keep the bunch length constant over a 1000 turns, the focusing periods for both the head and tail must be known to within 19.8 ps if the acceptable error is 20 ns by the 1011th turn.

5.2.3 Bunch Shape and Charge Losses

The following section presents measurements of total charge confined and the bunch shape for a few sets of focusing parameters described in Sec. 5.2.1.

When the longitudinal confinement system is operating, the rectangular bunch shape is maintained over the thousand turns (as shown in Fig. 5.3b and 5.9b-f below). Whereas, without confinement the bunch erodes, resulting in approximately only a hundred turns of transport (shown in Fig. 5.3a and Fig. 5.9a).

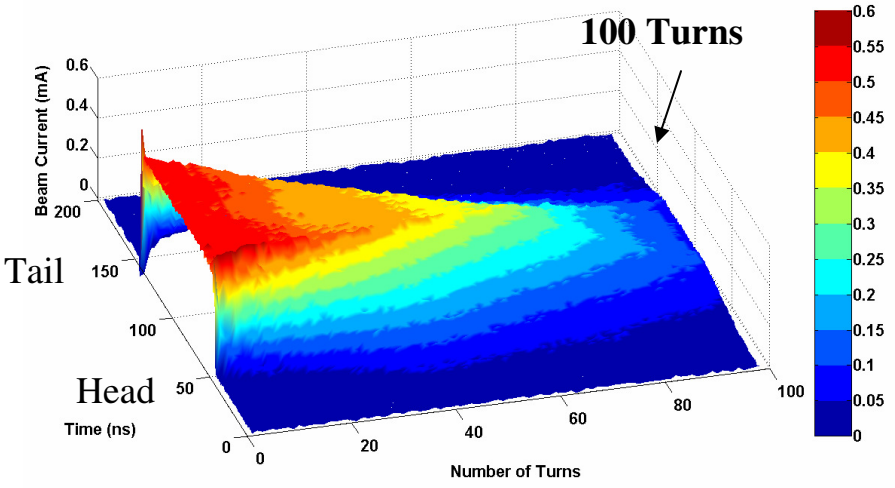

(a)

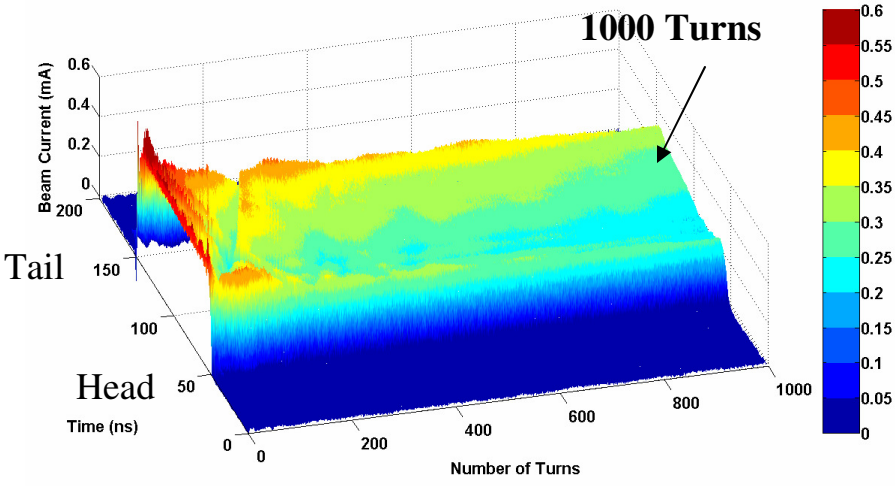

(b)

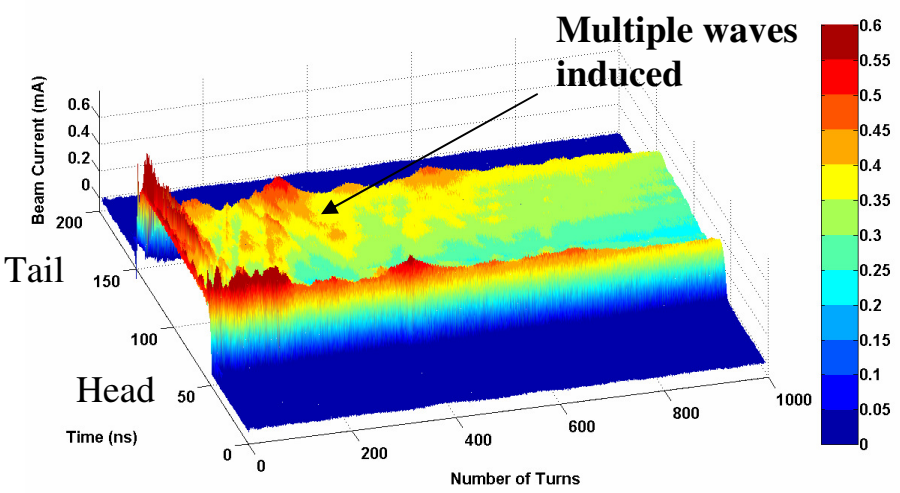
Multiple waves induced
Beam Current (mA)
0.6
0.4
0.2
0
Tail
200
150
100
Head
50
0
Time (ns)
0
200
400
600
800
1000
Number of Turns
0.6
0.55
0.5
0.45
0.4
0.35
0.3
0.25
0.2
0.15
0.1
0.05
0

(c)

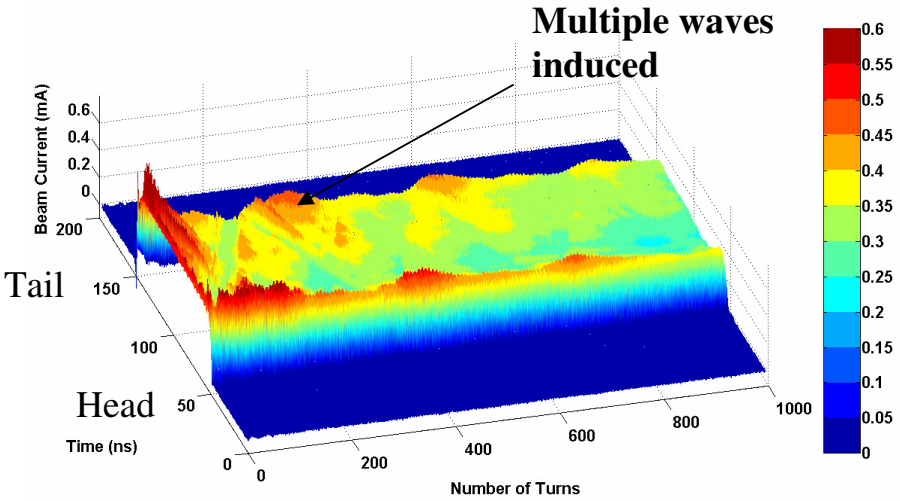
Multiple waves induced
Beam Current (mA)
0.6
0.4
0.2
0
Tail
200
150
100
Head
50
0
Time (ns)
0
200
400
600
800
1000
Number of Turns
0.6
0.55
0.5
0.45
0.4
0.35
0.3
0.25
0.2
0.15
0.1
0.05
0

(d)

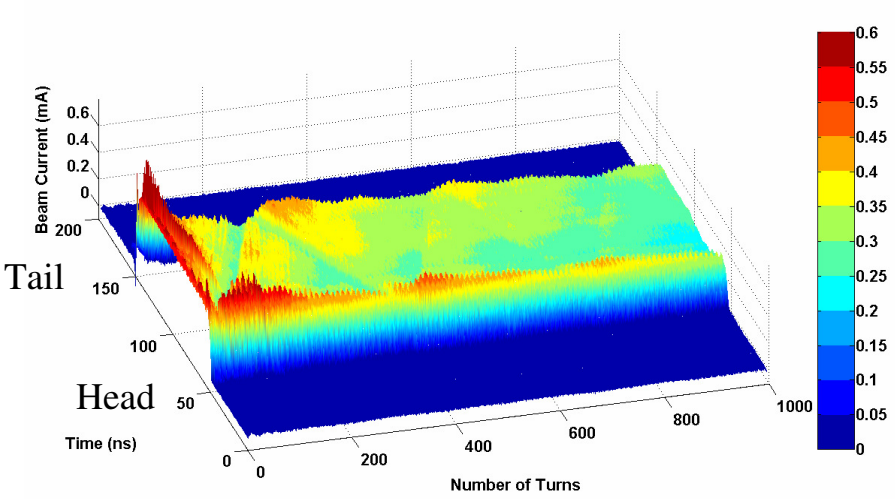

(e)

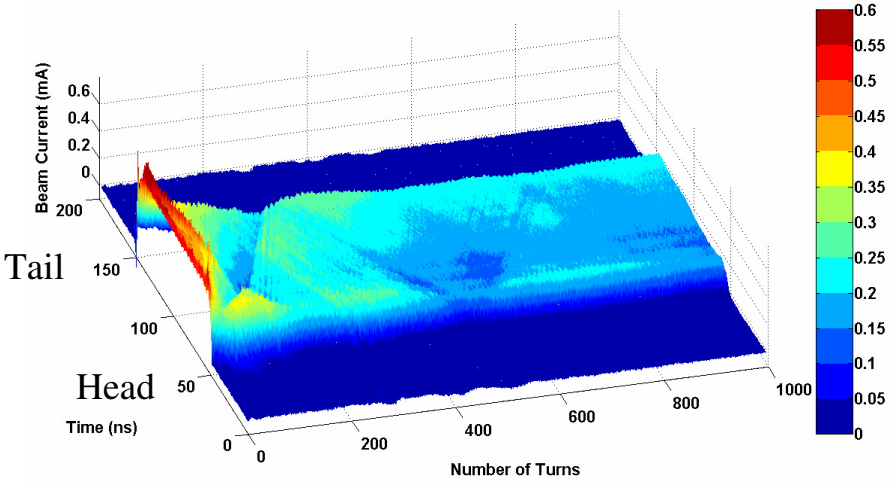

(f)

Fig. 5. 9. Three-dimensional view of the measured beam current at RC10 as a function of the number of turns. Color bar indicates the peak current amplitude in mA. Red indicates 0.6 mA.

Table 5.1, displays the corresponding focusing periods and amplitude for each case presented in Fig. 5.9a-f.

Table 5. 1. Focusing periods and amplitude for Fig. 5.9a-f.

Fig. 5.9.	**Focusing Periods**	**Focusing Amplitudes (V)**
(a)	*No focusing*	*No focusing*
(b)	5	59.6
(c)	5	129.4
(d)	7	118.0
(e)	10	129.4
(f)	10	59.6

Despite the initial losses at the beginning of transport with confinement, the overall bunch shape remains rectangular with space-charge waves induced at the bunch edges (see Ch 6). If the focusing amplitude is too large, multiple waves are induced at the edges, resulting in a distortion of the constant current pulse shape (as shown in Fig. 5.9c-d). When the focusing amplitude and period is not appropriately set, the bunch is not contained by the fields and, in effect, "leak out" (as shown in Fig. 5.9f). The total charge in the bunch per turn is displayed in Fig. 5.10 for each of the cases in Fig. 5.9a-f.

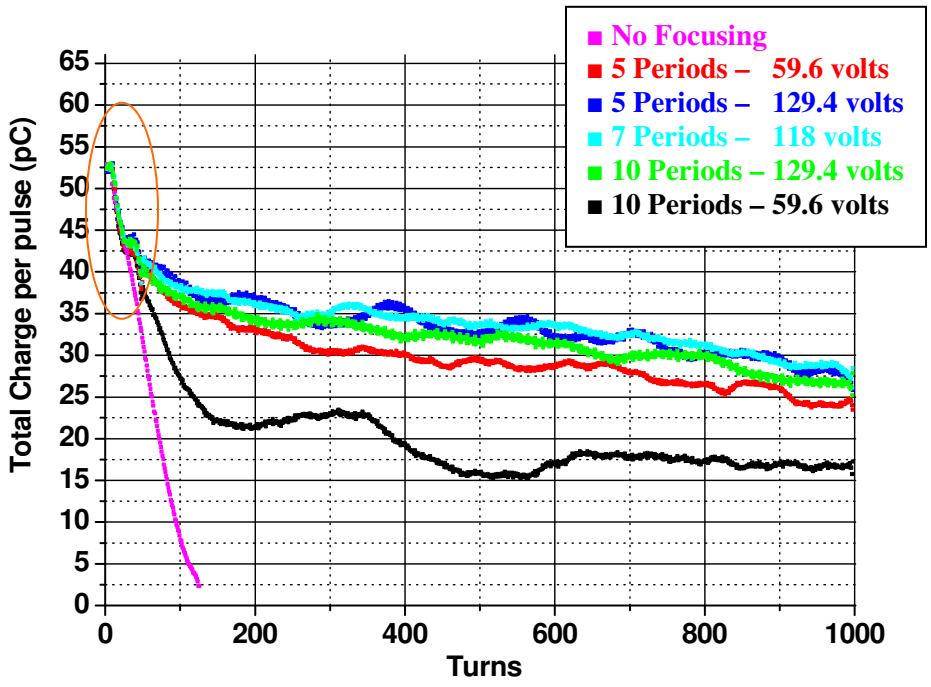

Fig. 5. 10. Total integrated charge per turn measured from the RC10 wall current monitor with and without confinement.

The total charge per turn was obtained by removing the baseline of the wall current monitor (see Sec. 3.1.1) and then integrating each current pulse multiplied by the pulse width.

Without confinement, the charge redistributes and approximately becomes constant throughout the circumference of the ring. The peak-to-peak signal also drops in amplitude, resulting in what appears as less current [74, 75]. This is shown in Fig. 5.10 as the magenta trace.

When the bunch is confined using the induction cell, the rectangular shape of the line-charge density is maintained. The other colored traces in Fig. 5.10, represent the confined total charge per pulse at the focusing parameters listed in Table 5.1.

There is a 17.8% current loss within the first fifty turns that affects all the traces independent of longitudinal focusing. This loss mechanism could be caused by a mis-

steering, transverse mismatch, halo, or an emittance growth (as discussed in Sec. 5.1.1), that would cause the beam to scrape against the beam pipe on each turn.

The longitudinal confinement contains at most 60% of the charge over a thousand turns with a loss rate of 0.01 pC/turn over the last 900 turns, as opposed to the 0.19 pC/turn within the first 50 turns. The fast loss rate will be discussed in the following chapter. The slower loss rate could be the result of the focusing parameters being imperfectly set, thus allowing some charge to "leak out." The difficulty with containment of the bunch-ends is that the longitudinal space-charge forces are current dependent. If there is a transverse current loss that causes the beam to scrape, the focusing must compensate accordingly and correlate with the current loss. Unfortunately in the present configuration, the fields are fixed amplitude and fixed period and thus modulation effects on the focusing fields can not be imposed to compensate for the loss mechanisms.

When the focusing fields are too large, multiple space-charge waves are induced at the edges of the bunch, resulting in the distortion of the bunch shape. By lowering the field amplitude, we are able to obtain a so called "optimized" solution that keeps the beam bunched with minimal distortion to the central region (as shown in Fig. 5.9b). This is relevant in scenarios where a clean rectangular pulse shape is desired as opposed to distorting the transported charge, when other loss mechanisms preexist.

5.3 Summary of Longitudinal Confinement

In this chapter we have investigated the erosion rates of both the bunch-ends as well as the overall bunch length. By performing linear fits to the first seven measured data

points in all three cases as opposed to all the data points, we obtain erosion rates that are within 4-8% of the WARP simulations fits. This shows that the experimental erosion rate is a quantity that varies throughout the beams lifetime as a result of mechanisms which are not accounted for in the simulations performed for this work.

When the longitudinal confinement system is operated, it contains 60% of the charge with minimal loss over the last 900 turns. By reducing the field amplitude slightly, we are able to maintain the transported charge and reduce the number of waves generated on the flat region, "optimizing" the rectangular pulse shape.

We have also been able to show the linear relationship between focusing amplitude and focusing period. If the focusing period is increased, the focusing amplitude must also be increased in order to compensate and maintain the average beam length of 101 ns. If this relationship is not respected, the average beam length will change as a result.

Finally we have also been able to explore the beam sensitivity to timing errors. If there is a 19.8 ps difference between the head and tail focusing periods, the overall beam length by the 1011^{th} turn will increase or decrease by approximately 20 ns. In order to maintain a constant beam length over 1000 turns with a 20 ns error, we must know the focusing period for the head and tail field to an accuracy of 19.8 ps.

Chapter 6: Measurements of Space-Charge Waves

This chapter presents an investigation of the space-charge waves induced at the edges of the bunch as a result of containment field errors.

6.1 Induced Space-Charge Waves

In this chapter, we estimate the beam radius using measured sound speeds while comparing to analytical calculations. We then explore the polarity dependent non-linear steepening effects of induced and reflected waves and finally present measurements on wave reflections at the bunch edges.

6.1.1 Sound speeds and Approximate Transverse Beam Size

As apparent from Fig. 5.9b-f, the transition to periodic focusing over the first few turns produces energy modulations at the beam edges that propagate as space-charge waves across the beam. Eventually, these waves reflect off the edges of the bunch and propagate in the opposite direction back toward the center, in some cases, sustaining multiple reflections. When focusing is applied at a focusing period of 5 and amplitude of 59.6 volts, we obtain a solution where both the head and tail waves launched from imperfections in the application of the end-containment fields are damped. This occurs between the first and second wave reflections (shown in Fig. 5.9b).

It is possible to estimate the propagation velocity (or sound speed C_s), using the rate at which the wave propagates across the bunch. Figure 6.1 below, is representative of the current profiles from the case in Fig. 5.9b, without interpolation. Space-charge waves are launched at the edges of the bunch and propagate to the other side of the beam.

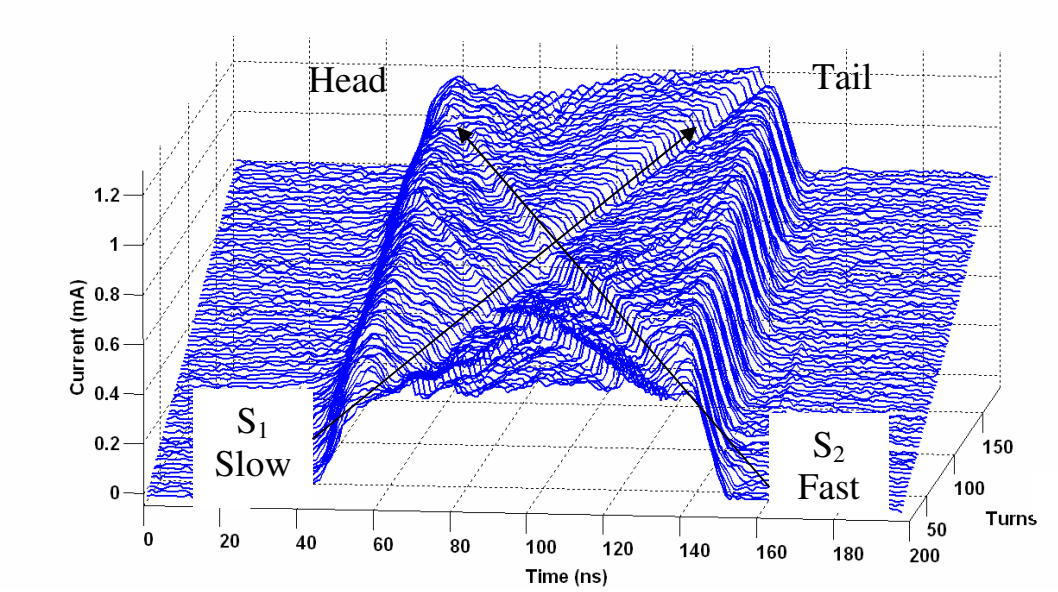

Fig. 6. 1. Individually measured beam current profiles per turn, displaying the waves launched from imperfections in the applications of the confinement fields. For clarity, starting from turn 21, each trace is shifted by 0.01 mA from the previous turn.

The S_1 and S_2 arrows (shown in Fig. 6.1) represent the wave propagation paths as they cross the length of the bunched beam. If the wave position within the beam pulse is measured for each turn, then the sound speed of the wave is calculable from the slope of the data. The position is found by recording the minimum (or valley) of the flat region of the rectangular beam pulse. Figure 6.2 below, displays the wave positions and slopes of the waves propagating along the beam pulse in Fig. 6.1 above.

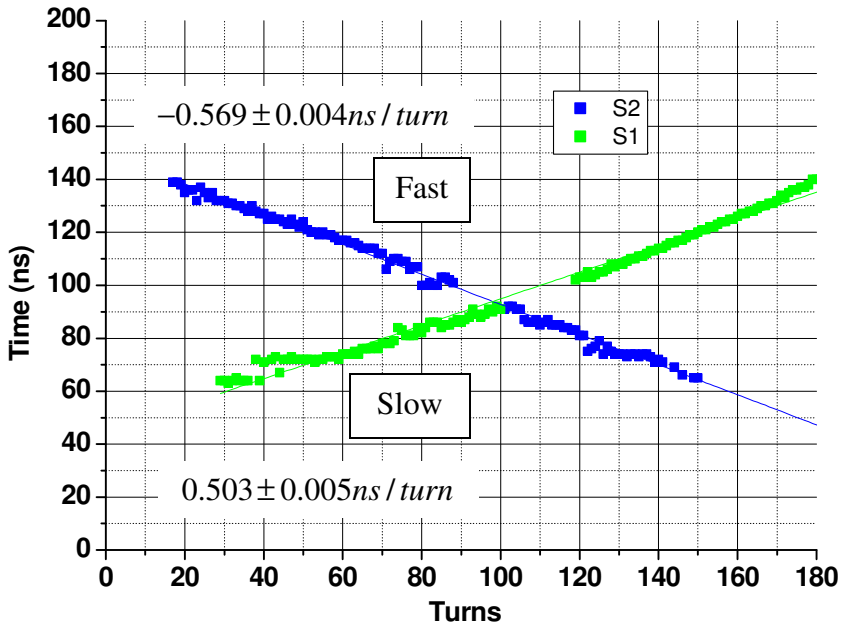

Fig. 6. 2. Measured wave positions within the bunched beam as a function of turns. Both S_1 and S_2 propagation rates are given on the figure.

The wave propagation rates for S_1 and S_2 paths, are shown in Fig. 6.2 above. The slow wave data (in green) is initiated from the head focusing field and the fast wave data (in blue) is initiated from the tail focusing field.

The sound speed C_s is calculated with the slopes listed in Fig. 6.2, using the formula $C_s = slope \times \frac{v_o^2}{11.52}$, where v_o is the beam velocity 5.83616±0.00003x10^7 m/s. The measured and analytical sound speeds C_s are displayed in Table 6.1 for the data displayed in Fig. 6.2. The average beam current over the 160 turns shown in Fig. 6.1 was 0.43±0.1 mA.

Table 6. 1. Measured and analytical calculation of C_s. The beam velocity v_o is 5.83616±0.00003x10^7 m/s and beam radius at the current listed in the table, using the smooth focusing approximation, is 1.56±0.02 mm.

Paths	**Average Beam Current (mA)**	**C_s – Theory (1 x10^5 m/s)**	**C_s – Measured (1 x10^5 m/s)**
S_1	0.43±0.1	2.52±0.28	1.49±0.02
S_2	0.43±0.1	2.52±0.28	1.68±0.01

The analytical C_s (using Eqn. 2.3 in section 2.1), differs by 33-41% from the measured C_s with longitudinal focusing (shown in Table 6.1). If we estimate beam radius and emittance using the measured sound speeds (in Table 6.1) we obtain 11.31±2.76 mm and 463±254 mm-mr for S_1 and 8.44±2.65 mm and 258±188 mm-mr for S_2. In order for the sound speed to slow down to the measured values, the beam radius must increase by a factor of $(5-7)$ and the emittance must increase by a factor of $(32-60)$ from the initial values. If we assume the disagreement between theory and measured values was a result of an emittance growth per turn, then the emittance must grow by a factor of 0.21-0.37 per turn in order to obtain the final values after 160 turns.

If we compare measurements from the previous chapter in Sec. 5.1.1 without longitudinal focusing, we obtained 1.36±0.08 ns/turn and 1.48±0.06 ns/turn for the bunch head and tail erosion rates, respectively. Converting these erosion rates to sound speeds C_s, first requires that we multiple these numbers by $\frac{1}{3\left(\sqrt{0.9}-\sqrt{0.1}\right)} \approx 0.5097$ in order to convert them into full bunch-end lengths (see discussion in Sec. 5.1.1). We obtain slopes of 0.69±0.04 ns/turn and 0.75±0.03

ns/turn for the bunch head and tail. The measured sound speeds without longitudinal focusing; using the relation $C_s = slope \times \frac{v_o^2}{11.52}$, is 2.04±0.12x$10^5$ m/s and 2.22±0.09x10^5 m/s for the bunch head and tail, respectively.

The measured values without longitudinal focusing are only 12-19% from the analytical C_s calculated above. The difference is substantially smaller than the measured values in Fig. 6.2. Though, this comparison is not a one for one comparison. The case without longitudinal focusing measures the erosion rates of the bunch-ends; where as, the case with focusing is an actual space-charge wave traveling along the length of the beam. In the case with focusing, the beam is also propagating around the accelerator substantially longer than without focusing.

The disagreement between the analytical calculations and with longitudinal focusing is due to a growth in beam size as a result of recent turn by turn transverse profile measurements (with the help of Dr. Timothy W. Koeth). This measurement is a relative measurement to the 1st turn as it is not yet calibrated. The measurement is also only horizontally valid as the voltage pulse used to deflect the beam, streaks the profile vertically. Figure 6.3 displays the beam profile for the 1st turn, the 100th turn and the 1000th turn.

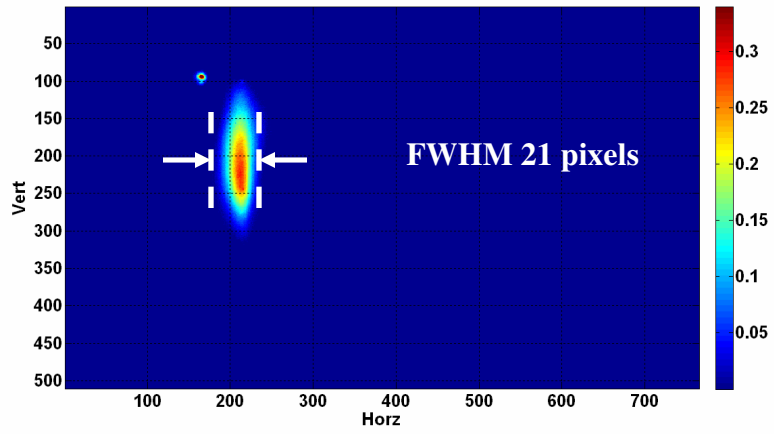

(a) 1st turn

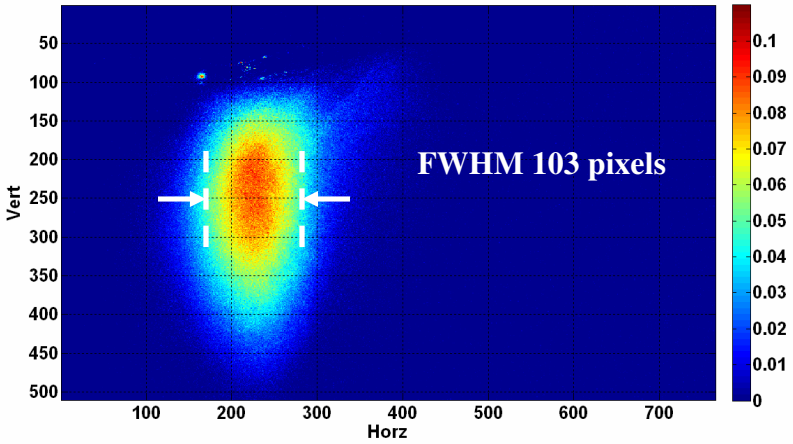

(b) 100th turn

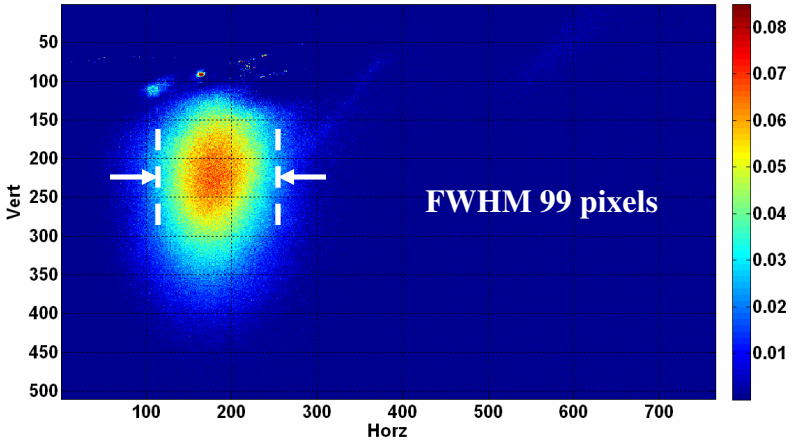

(c) 1000th turn

Fig. 6. 3. Measured beam profile on the (a) 1st turn, (b) 100th turn and the (c) 1000th turn.

The full width at half maximum (FWHM) number of horizontal pixels across is shown in Figures 6.3a-c. The relative increase in the beam distribution shows that the beam size increases by approximately a factor of five. Figure 6.4 displays the FWHM over a 1000 turns.

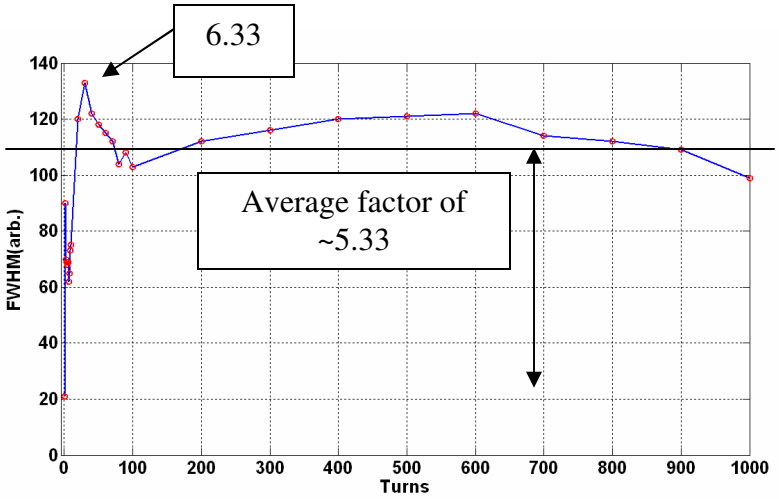

Fig. 6. 4. Measured beam profile on the (a) 1st turn, (b) 100th turn and the (c) 1000th turn.

The FWHM (shown in Fig. 6.4), increases by a factor of 6.33 within the first 30 turns. This result shows that the measured sound speed discrepancy is to first order well within calculations using the g-factor formula (Eqn. 2.4) presented earlier in this section. The beam size blow up, within the first 30 turns, is likely a result of mismatch at injection and the Y-section. The FWHM also appears to reach an equilibrium value of 5.33 from turns 30 to 1000.

6.1.2 Wave Reflections at the Bunch Edges

As presented in the previous section, with the longitudinal focusing system operating, one of the effects of the focusing fields has been the induced waves at the

edges of the bunch. Under the right focusing parameters (as shown in Fig. 5.9b-f), multiple wave reflections are capable of occurring as a result.

A reflection is a space-charge wave that reflects at the bunch edge and propagates in the opposite direction with alternate sign.

Another representation of Fig. 5.9b is shown in Fig. 6.5 below, where the view angle of the figure is tilted such that it is easier to see the wave paths along the bunch.

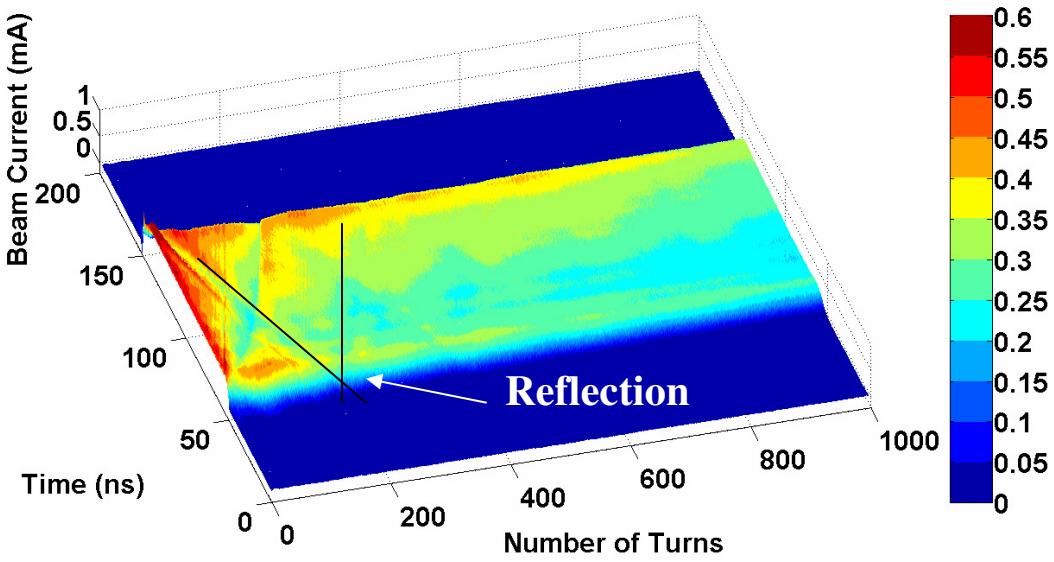

Fig. 6. 5. Beam current, displaying waves launched from imperfections in the applications of the confinement fields. Two black lines define the reflection that we will focus on.

The reflection duration is the time it takes the space-charge wave to reflect at the edge of the beam, which is estimated by following the waves along the bunch beam (shown in Fig. 6.5). The black line in the figure defines the reflection we will focus on. The last few instants of the wave prior to it reflecting are at turns 171 and 180 (as shown in Fig. 6.6a-b).

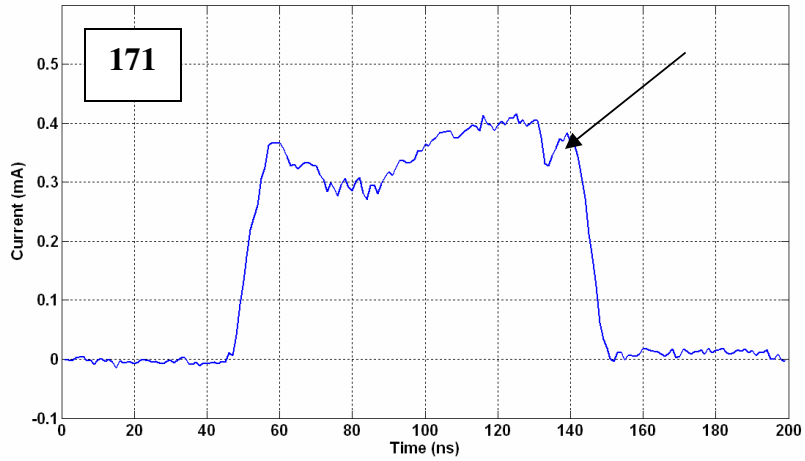

(a)

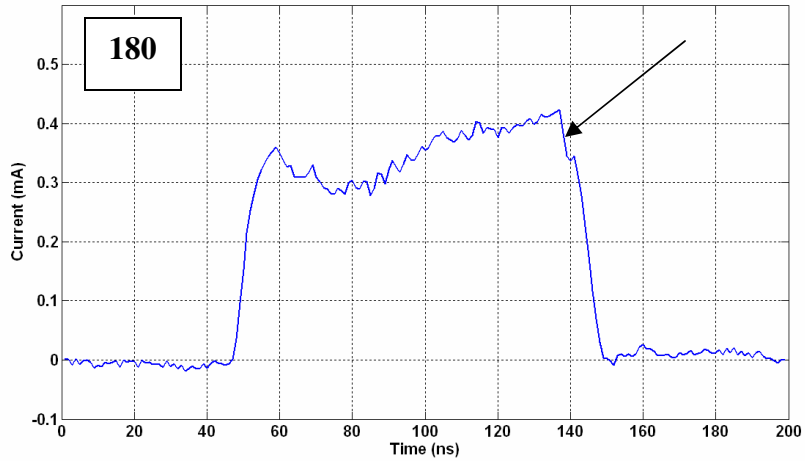

(b)

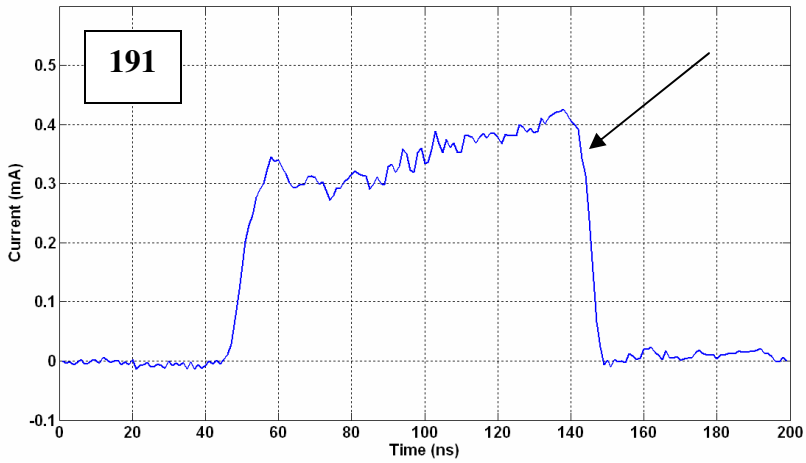

(c)

Fig. 6. 6. Beam current, displaying wave reflection. (a) is turn 171, (b) is turn 180 and (c) is turn 191.

After the wave reflects off the bunch edge, it reappears at approximately the same location on turn 191. This measurement method can only be used to approximate the result. The optimal method would be to repeat the measurement method used in Sec. 6.1.1. Unfortunately the wave amplitude appears to dampen out after the wave reflection, making the wave nearly undetectable within the flat region of the bunch.

The estimated distance required for the wave to reflect off of the bunch edge can be calculated using $S = \frac{v_o^2}{C_s} \times risetime$. Using the theoretical numbers from Sec. 6.1.1 (in Table 6.1 for a current of 0.425±0.1 mA and a rise time of 10 ns), we obtain a distance of 135±35 m. The measured data (in Fig. 6.6) is approximately 127±12 m, which is well within the error bars. Turns are converted into distance using the ring circumference listed in Table 3.3 of Sec. 3.4.1.

This suggests that the wave propagates the entire length of the bunch-end prior to it reflecting at the extreme edges.

6.1.3 Non-Linear Steepening

The following section analyzes non-linear wave motion as a result of the wave amplitude dependent phase velocity (or sound speed).

Space-charge waves (as shown in Fig. 5.9b-c & 6.1) propagating into the central region of the bunch are initiated as a result of the longitudinal mismatches at the bunch edges. As explained in section 2.1.2, an induced negative velocity perturbation has a negative line-charge density fast-wave and a positive line-charge density slow-wave (as shown in Fig. 6.7a). The opposite is true for an induced positive velocity

perturbation. The fast-wave is positive and slow-wave is negative (as shown in Fig. 6.7b).

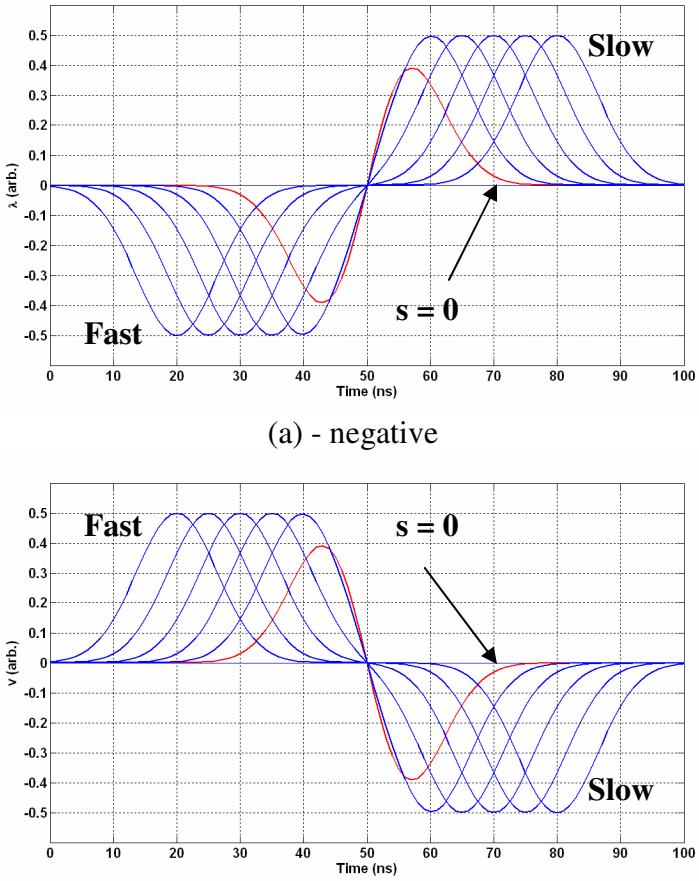

(a) - negative

(b) - positive

Fig. 6. 7. Line-charge density waves from induced (a) negative and (b) positive velocity perturbations (as presented in Section 2.1.2).

An effect of an energy-induced or density-induced space-charge wave is the resulting non-linear steepening at long path-lengths [12, 62]. Using the inviscid Burgers equation, we are able to ascertain why certain regions of the wave steepen more than others [12, 62, 82].

$$\frac{\partial v_1}{\partial t} + (C_s + v_1)\frac{\partial v_1}{\partial z} = 0 \qquad \text{(Eqn. 6. 1)}$$

Solving Eqn. 6.1 using the method of characteristic curves, we obtain the characteristic curve $\zeta(z,t) = z \mp (C_s + \mathrm{v}_1)t$, with a general solution equal to $\mathrm{v}_1(\zeta) = \mathrm{v}_1(z \mp (C_s + \mathrm{v}_1)t)$ [12, 62, 82]. The difference with this result compared to the theory presented in Sec. 2.1.1, (the dispersion relation, Eqn. 2.2) is the extra velocity term in the general solution. The general solution to the linear theory presented in Sec. 2.1.1 would be of the form $\mathrm{v}_1(\zeta) = \mathrm{v}_1(z \mp C_s t)$.

The non-linear solution of a general wave function is obtained by modifying the velocity component in the exponent. If for example, a gaussian line-charge density and velocity function of the form shown in Eqn. 6.2 is used,

$$f(z) = Ae^{-\frac{(z-\mu)^2}{2\sigma^2}} \qquad \text{(Eqn. 6. 2)}$$

where the FWHM of the perturbation is $2\sqrt{2\ln 2}\sigma$, then the linear perturbed line-charge density and velocity functions are shown in Eqn. 6.3 and Eqn. 6.4.

$$\lambda_1(z,t) = \mp\frac{\lambda_1(z=0,t=0^+)}{2}e^{-\frac{(z\mp C_s t)^2}{2\sigma^2}} \qquad \text{(Eqn. 6. 3)}$$

$$\mathrm{v}_1(z,t) = \frac{\mathrm{v}_1(z=0,t=0^+)}{2}e^{-\frac{(z\mp C_s t)^2}{2\sigma^2}} \qquad \text{(Eqn. 6. 4)}$$

The non-linear perturbed line-charge density and velocity functions (Eqn. 6.5 and 6.6) are calculated using the linear velocity solution (Eqn. 6.4) in the exponent as the initial condition. The following time step utilizes the previous non-linear velocity function.

$$\lambda_1(z,t) = \mp\frac{\lambda_1(z=0,t=0^+)}{2}e^{-\frac{(z\mp(C_s+\mathrm{v}_1(z,t))t)^2}{2\sigma^2}} \qquad \text{(Eqn. 6. 5)}$$

$$\mathrm{v}_1(z,t) = \frac{\mathrm{v}_1(z=0,t=0^+)}{2}e^{-\frac{(z\mp(C_s+\mathrm{v}_1(z,t))t)^2}{2\sigma^2}} \qquad \text{(Eqn. 6. 6)}$$

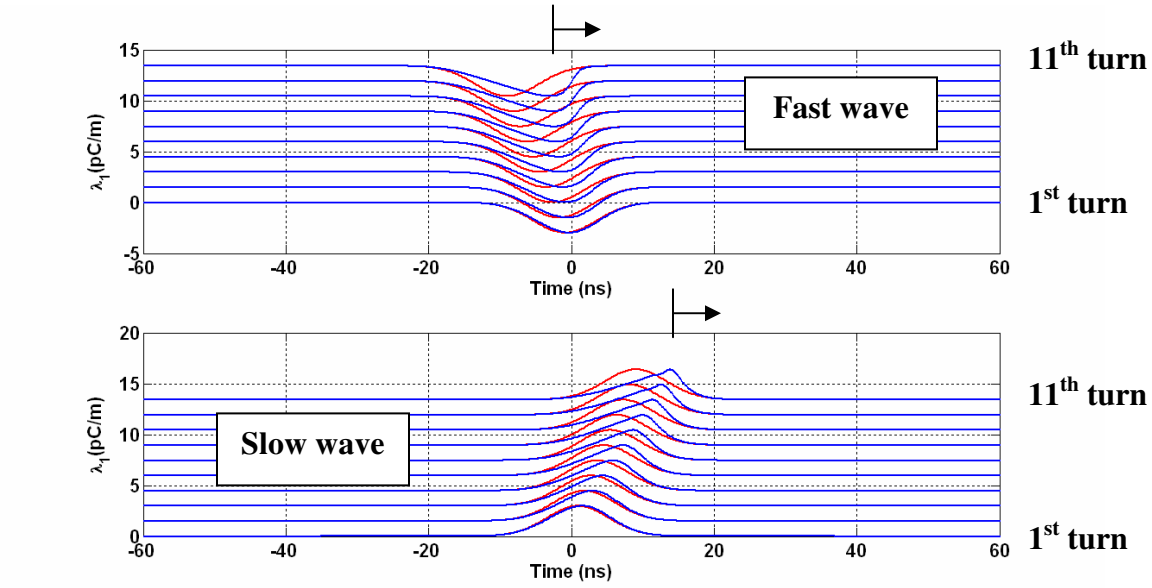

Fig. 6. 8. Calculated linear (red) and non-linear (blue) line-charge density space-charge waves for an induced negative perturbation. Each trace is shifted by 1.5 pC/m starting from the 2nd turn up to the 11th turn.

Figure 6.8 above, illustrates both the linear perturbed line-charge density and the non-linear perturbed line-charge density for 10 turns starting from the 1st up to the 11th turns. The negative perturbation amplitude is $\delta = \frac{v_1}{v_0} = 0.00304$ on the 0.6 mA beam, with a width of 10.3 ns. The figure displays both the fast and slow wave steepening to the right side of the figure, which is a result of the negative perturbation particles propagating at a slower velocity than the injected beam velocity. The same calculation can be repeated for a positive perturbation steepening towards the left side. The degree of steepening is also dependent on the perturbation amplitude [12, 62, 82]. If the perturbation amplitude is too large or the width is too small, then a soliton train is formed.

Similar steepening effects were seen on a 6 mA beam for negative induced perturbations [62]. Figure 6.9, displays the first six turns with a negative perturbation of 100 eV, induced in the center of the bunch.

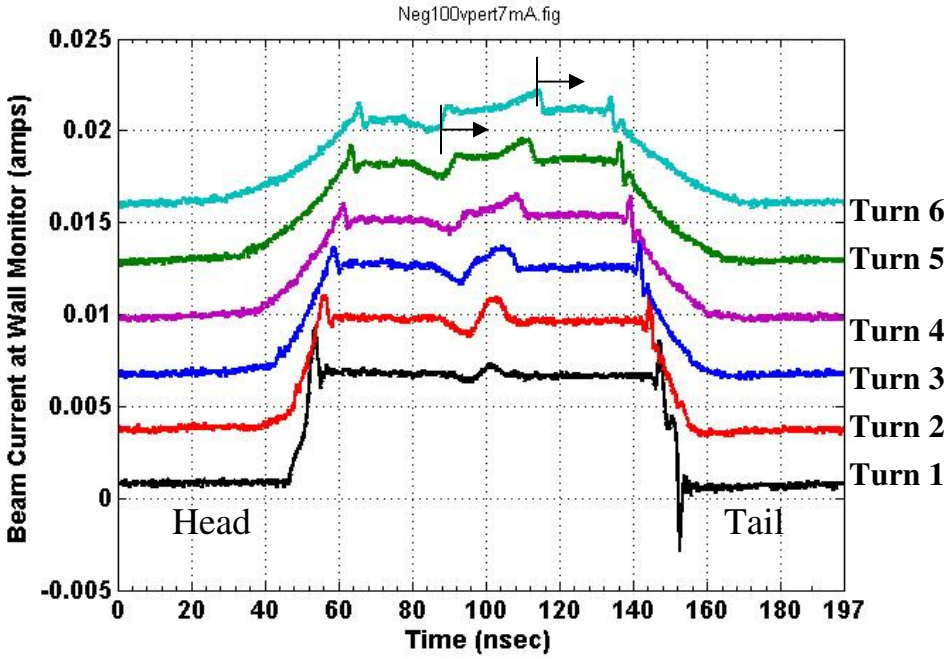

Fig. 6. 9. Measured beam current profiles of the 6 mA beam with an induced negative 100 eV perturbation in the center of the first turn. For clarity, starting from turn 2, each trace is shifted by 3 mA from the previous [64].

With a negative perturbation of $\delta = \frac{v_1}{v_0} = 0.00506$, both the fast and slow wave steepened towards the tail of the bunch. The opposite was true for positive perturbations; both the fast and slow wave would steepen towards the head of the bunch [62].

This steeping effect may also be used to tell if the induced waves at the edges of the beam are directly from the longitudinal focusing fields or the reflections of the induced waves.

The waves induced at the bunch edges (as shown in Fig. 6.1 and Fig. 6.10 below) are both a combination of initial waves traveling into the central region of the beam from "focusing mismatches" as well as reflections.

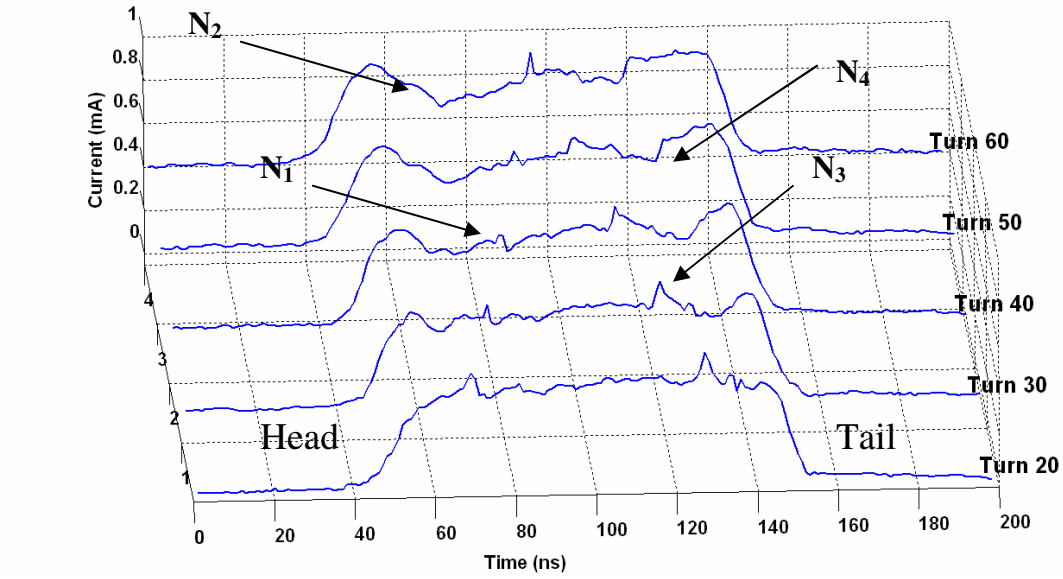

Fig. 6. 10. Measured beam current profiles at RC10, displaying the waves launched from imperfections in the applications of the confinement fields. The waves are labeled by N_1-N_4. For clarity, starting from turn 30, each trace is shifted by 0.1 mA from the previous.

The focusing field necessary to contain the bunch head is a negative perturbation amplitude of $\delta = \frac{v_1}{v_0} = 0.00304$, and so it will induce a positive polarity slow wave (N_1) into the central region of the beam that steepens towards the tail of the beam (as shown in Fig. 6.10). Since the wave is induced at the beam edge, the fast wave reflects at the edge and propagates into the beam as a negative polarity slow wave (N_2) as if induced by a positive perturbation. This is seen by the non-linear steepening towards the head of the bunch.

A similar effect was also observed in the bunch tail. The focusing field necessary to contain the tail is a positive perturbation of the same magnitude, and so it will induce a negative polarity fast wave (N_3) into the central region of the beam that steepens towards the head of the beam. Since the wave is induced at the beam edge, the slow wave reflects at the edge and propagates into the beam as a negative polarity fast wave (N_4) as if induced by a negative perturbation. This was observed by the non-linear steepening, towards the tail of the bunch.

Though this effect results in dispersive wave propagation, the steepening direction illustrates the magnitude of the electron velocities within the space-charge waves (as either a positive or negative energy modulated velocity wave). The steepening functions as an individual wave indicator, separating reflected waves from ones that are not.

6.2 Summary of Space-Charge Wave Measurements

In this chapter, we have compared analytical calculations and measured sounds speeds with longitudinal focusing, obtaining large discrepancies. Though, when the analytical numbers were compared with measured sounds speeds without the use of longitudinal focusing, we achieved better agreement between theory and measurements.

The disagreement between analytical calculations and sounds speed measurements with longitudinal focusing is due to a growth in the beam size as a result of recent turn by turn beam size comparison measurements. Within the first 30 turns, the beam

distribution full width at half maximum (FWHM), increases by a factor of ~6.33 from the first turn. This result shows that the measured sound speed discrepancy is to first order well within calculations using the g-factor formula (Eqn. 2.4). The reasons behind the beam size blow-up are not yet fully understood and still need more investigation, but a first assumption is that the matching at injection and the Y-section must be re-optimized.

We then explored the beam propagation distance required for a wave to reflect off the extreme edge of the bunch. Though this experiment should be repeated with an additional wave launched on the flat region of the contained bunch, we were still able to obtain good agreement between analytical calculations and measurements. Theory approximated a distance of 135±35 m whereas measurements approximated a distance of 127±12 m, which was well within the error bars.

This chapter concluded with a discussion of non-linear wave propagation and the term necessary to achieve non-linear steepening within the general solution to the wave equation. We then used the non-linear steepening concept as a tool to discern if a space-charge wave, induced as a result of errors in the longitudinal matching, was a transmitted wave or a reflected wave of the bunched beam edges.

Chapter 7: Conclusion

In this chapter I conclude by summarizing the work in this dissertation and then end with a few topics that could be further investigated.

7.1 Summary and Conclusion

In this dissertation, I presented an experimental study on the requirements needed to control longitudinal space-charge forces in high-intensity beams using induction focusing. I found that, without longitudinal focusing, space-charge in a bunch propagating in a circular machine results in a correlated transverse motion along the bunch as a result of the energy profile coupling through the dispersive bends. This was indirectly measured in three different ways and compared with theory and simulation. If the beam is mis-steered at any location around the ring, this effect will eventually cause the bunch to result in a large correlated energy spread and increase the risk that the beam scrapes the pipe walls.

When I applied the longitudinal focusing fields periodically to the beam edges, the beam bunch was stored for over 1000 turns, significantly improving the bunch lifetime. This is a factor of ten greater than the original design for the accelerator. I also conducted a study of focusing errors and sensitivity. I found that synchronization between head and tail application rates is critical; for example, a jitter in the head and tail pulse timing of a mere 20 ps leads to a 20 ns change in beam length over 1000 turns. By varying the periodic application rates and focusing

amplitudes, I also showed the existence of a linear relationship between them, allowing me to maintain the same average bunch length for different application rates.

Finally, when longitudinal focusing was applied, errors in the focusing fields were observed to induce space-charge waves at the bunch edges. These waves traveled across the bunch central region and in some cases sustained multiple reflections at the ends. Measurements of the wave speeds showed large discrepancies from analytical calculations and other measurements without longitudinal focusing, suggesting an increase in transverse beam radius. This hypothesis has been confirmed recently with turn-by-turn beam size measurements. The reasons behind the beam size blow-up are not yet fully understood and deserve further investigation, but there is a strong suspicion that the transverse rms matching at injection and the Y-section must be re-optimized. I was also able to use the non-linear steepening of space-charge waves to observe the particle velocity polarities in both transmitted and reflected waves.

7.2 Suggested Future Research Topics

The studies presented here open the door for using UMER to address two major unanswered questions in beam physics:

1. What is the limit on transportable beam current in UMER?
2. What do such limits tell us about how to design other higher intensity, higher energy accelerators?

UMER is capable of injecting a broad range of charge, from 60 pC up to 10 nC per bunch, spanning a vast range of beam intensities. This limit is not a hard limit, as more charge may be extracted with a few modifications to the system. Implementing containment at these higher intensities will require larger focusing fields, applied in some cases at fractions of the revolution frequency. This can be accomplished through the utilization of more than one induction cell per turn. With longitudinal containment, we will be able to investigate the factors that limit the transportable charge in this machine as well as other high-intensity circular and linear machines that may be built in the future.

An additional topic that should be investigated is the longitudinal energy profiles of intense bunches propagating in a circular machine. Using direct measurements with an energy analyzer will allow us to better understand the turn-by-turn evolution of the longitudinal energy profile and some of the discrepancies measured using indirect methods.

The induction cell can also be used to accelerate the beam. I have shown preliminary acceleration on UMER, but more work is needed to complete the high-voltage modulator electronics that pulse the induction cell [86]. An additional induction cell has been installed on UMER for this very reason at RC16. With this added hardware, we will be able to investigate resonance crossings as well as the rates of crossing.

The longitudinal focusing should also be simulated using a Particle-In-Cell (PIC) code, in order to find the optimal focusing solutions. This allows us to minimize the amount of space-charge waves induced by the longitudinal focusing fields while

maximizing the transported charge. This should be repeated for cases with transverse current losses in order to better resolve the beam current dependence on the focusing parameters.

Appendices

A.1 UMER Calculations

The lattice periodicity S or the FODO cell period is equal to 0.32 m, where the zero-current phase advance σ_0 is equal to 66.5^o at a quadrupole current of 1.82 A. This allows us to calculate the betatron oscillation wavelength with no space-charge Λ_o, using $\Lambda_o = \frac{2\pi S}{\sigma_0} = 1.73m$ [12].

If space-charge is included in the calculation, the betatron wavelength with space-charge Λ increases and is defined by Eqn. A.1,

$$\Lambda = \frac{2\pi}{k} = \frac{2\pi S}{\sigma} \qquad \text{(Eqn. A. 1)}$$

where k is the wave number and σ is the phase advance with space-charge. This depresses the betatron oscillations by decreasing the phase advance or tune in the machine. To calculate the phase advance with space-charge, we use the smooth approximation defined in Eqn. A.2,

$$\sigma = \sigma_o \left(\sqrt{1+u^2} - u \right) \qquad \text{(Eqn. A. 2)}$$

where u is a parameter defined as $u = \frac{KS}{2\sigma_0 \varepsilon}$ [12]. The variable K is the generalized perveance and ε is the un-normalized effective emittance. The generalized perveance is calculated using Eqn. A.3,

$$K = \frac{2I}{I_0 (\beta\gamma)^3} \qquad \text{(Eqn. A. 3)}$$

where I_o is the characteristic current equal to 17 kA for electrons, I is the beam current, β is the ratio of the beam velocity to the speed of light and γ is the Lorentz factor. For the 21 mA beam, the wavelength with space-charge is 5.54 m, where the phase advance with space-charge is 20.8^o assuming the quadrupoles are operating at a current of 1.82 A.

To calculate the average radius's $\overline{R}$ shown in Tables 3.5 and 3.6, for a periodic focusing channel with space-charge, we use Eqn. A.4 assuming the smooth approximation [12].

$$\overline{R} = \overline{R}_o \sqrt{u + \sqrt{1+u^2}} \qquad \text{(Eqn. A. 4)}$$

In Eqn. A.4, $\overline{R}_o$ is the average radius without space-charge and u is the same parameter as defined earlier prior to the generalized perveance.

A.2 Induction Cell System Experimental Test Stand

The induction cell system is composed of a high voltage modulator located directly next to the induction cell installed at RC4 (as shown in Fig. A.1a-b). The Glassman High voltage power supplies for the modulator are located directly underneath.

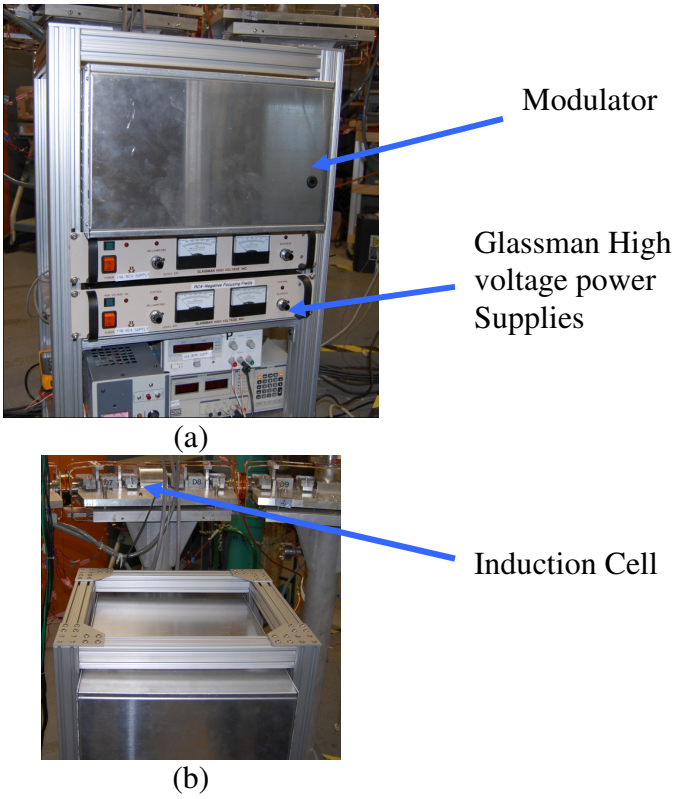

Fig. A. 1. Induction cell experimental test stand. The (a) side view and the (b) top view is shown.

Both power supplies are computer controlled via the UMER control system through the use of the Lab VIEW GUI control computer (in Fig. A.2a). A DSO7104A Agilent oscilloscope, normally on top of the experimental apparatus, is the present digitizer for the induction cell voltage waveforms and a beam timing monitor using the RC3 BPM.

The 81150A Agilent function generator (in Fig. A.2b) at the console is used to set the timing of the individual focusing pulses sent to the modulator at the RC4

induction cell. Channel 1 is the negative focusing timing generator and channel 2 is the positive focusing timing generator. Both are triggered from the master timing via the external sync connection on the Agilent function generator. Both channels are set to burst mode operation, with a 200 pulse burst of TTL level pulses at a focusing period that is a multiple of the beam revolution period where each channel is independently controlled.

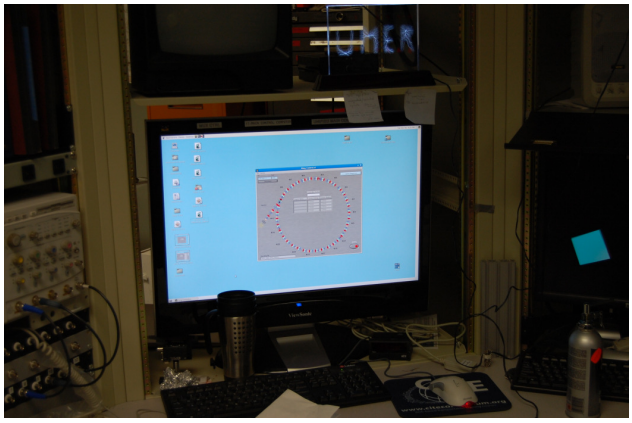

(a)

(b)

Fig. A. 2. UMER Console components that control the induction cell experimental test stand. The (a) Lab VIEW GUI control computer and the (b) 81150A Agilent function generator is shown above.

Using the Agilent function generator, the focusing pulses at the modulator may be set to purposely induce space-charge waves using a 2-pulse burst or programmed to run in the normal mode of operation with the containment fields.

Bibliography

[1] L. Evans, New Journal of Physics, **9**, 335, (2007).

[2] European Organization for Nuclear Research (CERN). http://sl-div.web.cern.ch/sl-div/history/lep_doc.html

[3] R. R. Wilson, The Tevatron, Physics Today, **30**, 10, (1977).

[4] Oak Ridge National Lab (ORNL). http://neutrons.ornl.gov/about/what.shtml

[5] J. Tang, S. Hartman and L. Longcoy, Proceedings of the 12th International Conference on Accelerator and Large Experimental Physics Control Systems, Kobe, (2009).

[6] H.-D. Nuhn, Proceedings of the Free Electron Laser Conference, Liverpool, (2009).

[7] A. Ekkebus, Neutron News, **21**, 54, (2010).

[8] V. Ayvazyan, N. Baboi, J. Bahr, V. Balandin, B. Beutner, A. Brandt, I. Bohnet, A. Bolzmann, R. Brinkmann, O.I. Brovko, J.P. Carneiro, S. Casalbuoni, *et al.*, The European Physics Journal D, **37**, 297-303, (2006).

[9] J.B. Rosenzweig, *Fundamentals of Beam Physics*, (Oxford, Oxford University Press, 2003).

[10] Linac Coherent Light Source (LCLS). https://slacportal.slac.stanford.edu/sites/lcls_public/Pages/Default.aspx.

[11] Virtual National Lab for Heavy Ion Fusion. http://hif.lbl.gov/.

[12] M. Reiser, *Theory and Design of Charged Particle Beams* 2nd Ed. (Wiley-VCH Inc., Weinheim Germany, 2008).

[13] C. Papadopoulos, Ph.D. Dissertation, University of Maryland, (2009).

[14] J.C.T. Thangaraj, Ph.D. Dissertation, University of Maryland, (2009).

[15] H.H. Braun, R. Corsini, L. Groening, F. Zhou, A. Kabel, T.O. Raubenheimer, R. Li, and T. Limberg, Physical Review Special Topics – Accelerators and Beams, **3**, 124402, (2000).

[16] R.A. Kishek, G. Bai, S. Bernal, D. Feldman, T.F. Godlove, I. Haber, P.G. O'Shea, B. Quinn, C. Papadopoulos, M. Reiser, D. Stratakis, K. Tian, C.J. Tobin, and M. Walter, International Journal of Modern Physics A, **22**, 3838, (2007).

[17] S. Ramo, Physical Review, **56**, 276, (1939).

[18] W. C. Hahn, Gen. Elec. Rev., **42**, 258, (1939).

[19] C. Birdsall and J. Whinnery, Journal of Applied Physics, Vol. **24**, 3, 314, (1953).

[20] J. G. Wang, D. X. Wang and M. Reiser, Physical Review Letters, Vol. **71**, 12, 1836, (1993).

[21] D.X. Wang, J.G. Wang, and M. Reiser, Physical Review Letters, **73**, 66, (1994).

[22] Y. Zou, Y. Cui, V. Yun, A. Valfells, R.A. Kishek, S. Bernal, I. Haber, M. Reiser, P. G. O'Shea, and J.G. Wang, Physical Review Special Topics – Accelerators and Beams, Vol. **5**, 072801, (2002).

[23] Y. Cui, Y. Zou, M. Reiser, R.A. Kishek, I. Haber, S. Bernal, and P. G. O'Shea, Physical Review Special Topics – Accelerators and Beams, Vol. **7**, 072801, (2004).

[24] K. Tian, Y. Zou, Y. Cui, I. Haber, R. A. Kishek, M. Reiser and P. G. O'Shea, Physical Review Special Topics – Accelerators and Beams, Vol. **9**, 014201, (2006).

[25] Y. Huo, Masters Thesis, University of Maryland, (2004).

[26] J.R. Harris, J.G. Neumann and P.G. O'Shea, Journal of Applied Physics, **99**, 093306, (2006).

[27] J. C. T. Thangaraj, G. Bai, B.L. Beaudoin, S. Bernal, D.W. Feldman, R. Fiorito, I. Haber, R.A. Kishek, P.G. O'Shea, M. Reiser, D. Stratakis, K. Tian, and M. Walter, Proceedings of the 2007 Particle Accelerator Conference, Albuquerque, 2007 (IEEE, New York, 2007).

[28] A. Friedman, D.P. Grote, E.P. Lee, and E. Sonnendrucker, Nuclear Instruments and Methods In Physics Research – A, **464**, (2001).

[29] B.L. Beaudoin, S. Bernal, I. Haber, R.A. Kishek, P.G. O'Shea, M. Reiser, J.C.T. Thangaraj, K. Tian, M. Walter and C. Wu, Proceedings of the 2007 Particle Accelerator Conference, Albuquerque, 2007 (IEEE, New York, 2007).

[30] D.A. Callahan, A.B. Langdon, A. Friedman, I. Haber, Proceedings of the 1993 Particle Accelerator Conference, Washington DC, 1993 (IEEE, New York, 1993).

[31] A. Friedman, J.J. Barnard, R.H. Cohen, D.P. Grote, S.M. Lund, W.M. Sharp, A. Faltens, E. Henestroza, J-Y. Jung, J.W. Kwan, E.P. Lee, M.A. Leitner, B.G. Logan, J.-L. Vay, W.L. Waldron, R.C. Davidson, M. Dorf, E.P. Gilson, and I. Kaganovich, Proceedings of the International Computational Accelerator Physics Conference 2009, San Francisco, 2009 (IEEE, New York, 2009).

[32] D. Kerst, Physical Review Letters, **58**, 841, (1940).

[33] N. C. Christofilos, R.E. Hester, W.A.S. Lamb, D.D. Reagan, W.A. Sherwood, and R.E. Wright, Review of Scientific Instruments, **35**, 886, (1964).

[34] J. W. Beal, N.C. Christofilos, and R.E. Hester, IEEE Transactions on Nuclear Science, NS **16**, 294, (1969).

[35] C. Thoma, and T.P. Hughes, Proceedings of the 2007 Particle Accelerator Conference, Albuquerque, 2007 (IEEE, New York, 2007).

[36] Yu-Jiuan Chen, George J. Caporaso, Arthur C. Paul, and William M. Fawley, Proceedings of the 1999 Particle Accelerator Conference, New York, 1999 (IEEE, New York, 1999).

[37] R. Scarpetti, J. Boyd, G. Earley, K. Griffin, R. Kerr, R. Kihara, M. Ong, J-M, Zentler, and N. Back, Digest of Technical papers, 11th IEEE International Pulsed Power Conference, Baltimore, 1997, (IEEE, New York, 1997).

[38] D. Keefe, IEEE Transactions on Nuclear Science, NS **32**, 5, (1985).

[39] J.J. Barnard, G.J. Caporaso, S. Yu, and S. Eylon, Proceedings of the 1993 Particle Accelerator Conference, Washington DC, 1993 (IEEE, New York, 1993).

[40] P.A. Seidl, White Paper for Fusion-Fission Research Workshop, Gaithersburg, (2009).

[41] P. Efthimion, E. Gilson, L. Grisham, R. Davidson, L. Logan, P. Seidl, and W. Waldron, Nuclear Instruments and Methods in Physics Research A, **606**, 124, (2009).

[42] L. Ahle, T.C. Sangster, J. Barnard, C. Burkhart, G. Craig, A. Debeling, A. Friedman, W. Fritz, D.P. Grote, E. Halaxa, R.L. Hanks, M. Hernandez, H.C. Kirbie, B.G. Logan, S.M. Lund, G. Mant, W. Molvik, W.M. Sharp, C. Williams, Nuclear Instruments and Methods In Physics Research – A, **464**, (2001).

[43] K. Takayama, K. Torikai, Y. Shimosaki, T. Kono, T. Iwashita, Y. Arakida, E. Nakamura, M. Shirakata, T. Sueno, M. Wake, and K. Otsuka, Proceedings of the 2006 European Particle Accelerator Conference, (IEEE, New York, 2006).

[44] Y. Shimosaki, E. Nakamura, and K. Takayama, Physical Review Special Topics – Accelerators and Beams, **7**, 014201, (2004).

[45] I. Haber, S. Bernal, B. Beaudoin, M. Cornacchia, D. Feldman, R.B. Feldman, R. Fiorito, K. Fiuza, T.F. Godlove, R.A. Kishek, P.G. O'Shea, B. Quinn, C. Papadopoulos, M. Reiser, D. Stratakis, D. Sutter, J.C.T. Thangaraj, K. Tian, M. Walter, and C. Wu, Nuclear Instruments and Methods in Physics Research A, **606**, 64, (2009).

[46] L. Pedrotti, Class Notes, (Physics of Waves). http://academic.udayton.edu/LenoPedrotti/text232/PHY232.html

[47] A. Hofmann, 1976, Theoretical Aspects of the Behavior of Beams in Accelerators and Storage Rings, Proceedings of the International School of Particle Accelerators, Erice, Italy, edited by M. H. Blewett, A. Z. Zichichi, and K. Johnsen (CERN, Geneva, 1977).

[48] John Barnard and Steve Lund class notes on the, Interaction of Intense Charged Particle Beams with Electric and Magnetic Fields. http://hifweb.lbl.gov/NE290H/

[49] D.D.M. Ho, S.T. Brandon, and E.P. Lee, Particle Accelerators, **35**, 15, (1991).

[50] B. Beaudoin, S. Bernal, K. Fiuza, I. Haber, R.A. Kishek, P.G. O'Shea, M. Reiser, D. Sutter and J.C.T Thangaraj, Proceedings of the 2009 Particle Accelerator Conference, Vancouver, 2009 (IEEE, New York, 2009).

[51] R. C. Davidson, E. A. Startsev, and H. Qin, Proceedings of the 2007 Particle Accelerator Conference, Albuquerque, 2007 (IEEE, New York, 2007).

[52] J.J. Barnard, Private communication, (2010).

[53] D.P. Grote, A. Friedman, I. Haber, and S. Yu, Fusion Engineering and Design, **32-33**, 193, (1996).

[54] WinAgile. http://www.maxlab.lu.se/acc-phys/teach/mnx301/1998/13-winagile.htm

[55] P.J. Bryant and K. Johnsen, *The Principles of Circular Accelerators and Storage Rings*. (Cambridge University Press, 1993).

[56] H. Wiedemann, *Particle Accelerator Physics I* 2nd Ed., (Springer-Verlag Berlin Heidelberg New York, 1993).

[57] R. C. Webber, AIP **212**, Brookhaven, 85, (1990).

[58] Y. Zou, Ph.D. Dissertation, University of Maryland, (2000).

[59] Princeton Instruments. http://www.princetoninstruments.com/

[60] D. Stratakis, Ph.D. Dissertation, University of Maryland, (2008).

[61] Proxitronic Detector Systems. http://www.proxitronic.de/

[62] B. Beaudoin, Master Thesis, University of Maryland, (2008).

[63] BEHLKE. http://www.behlke.de/

[64] Cadence. http://www.cadence.com/us/pages/default.aspx

[65] D.K. Cheng, Field and Wave Electromagnetics (2nd Edition), Addison-Wesley Publishing Company, 1989.

[66] BELDEN. http://www.belden.com/

[67] S. Humphries Jr., T.R. Lockner, and J.R. Freeman, IEEE Transactions on Nuclear Science, NS **28**, 3410, (1981).

[68] S. Humphries Jr., *Principles of Charged Particle Acceleration* (Wiley, New York NY, 1986).

[69] V.K. Neil, "The Image Displacement Effect in Linear Induction Accelerators," NTIS-UCID17976, (1978).

[70] R. Ray, A.K. Datta, Journal of Applied Physics, **21**, 1336, (1988).

[71] Ceramic Magnetics, Inc. http://www.cmi-ferrite.com/

[72] W. Waldron, private communication, (2007).

[73] K. Tian, R.A. Kishek, I. Haber, and P.G. Oshea, Physical Review Special Topics – Accelerators and Beams, **13**, 034201, (2010).

[74] T. Koeth, "Beam interpenetration and DC accumulation in the University of Maryland electron ring," (2011).

[75] T. Koeth, B. Beaudoin, S. Bernal, M. Cornacchia, K. Fiuza, I. Haber, R.A. Kishek, M. Reiser, and P.G. O'Shea, Proceedings of the 14th Workshop on Advanced Accelerator Concepts (AAC), Annapolis, 2010 (AIP, New York, 2010).

[76] D. Sutter, S. Bernal, C. Wu, M. Cornacchia, B. Beaudoin, K. Fiuza, I. Haber, R.A. Kishek, M. Reiser, and P.G. O'Shea, Proceedings of the 2009 Particle Accelerator Conference, Vancouver, 2009 (IEEE, New York, 2009).

[77] M. Cornacchia and D. Sutter, "Verification of the validity of the horizontal BPM measurements," UMER Technical Note.

[78] R.A. Kishek, UMER Technical Note, Note UMER-10-0505-RAK, (2010).

[79] A. Oppenheim, A. Willsky, and S.H. Nawab, *Signals and Systems* 2nd Ed (Prentice Hall, Upper Saddle River, NJ, 1997).

[80] M. Venturini, and M. Reiser, Physical Review Letters, **81**, 96, (1998).

[81] M. Venturini, and M. Reiser, Physical Review E, **57**, 4725, (1998).

[82] Lecture Notes by Ling-Hsiao. http://www.ss.ncu.edu.tw/~lyu/lecture_files_en/

[83] B. Beaudoin, I. Haber, R.A. Kishek, S. Bernal, T. Koeth, D. Sutter, P.G. O'Shea, and M. Reiser, Physics of Plasmas, 013104, (2011).

[84] J.J. Deng, J.G. Wang, and M. Reiser, Proceedings of the 1997 Particle Accelerator Conference, Vancouver, 1997 (IEEE, New York, 1997).

[85] D. Neuffer, IEEE Transactions on Nuclear Science, NS **26**, 3, (1979).

[86] B. Beaudoin, S. Bernal, K. Fiuza, I. Haber, R.A. Kishek, T. Koeth, P.G. O'Shea, M. Reiser, D. Sutter, and J.C.T. Thangaraj, Presentation-"Longitudinal Focusing Studies for Heavy Ion Inertial Fusion," Sixth International Conference on Inertial Fusion Sciences and Applications, San Francisco, (2009).